Assessing different types of disorder in carbonate minerals with vibrational spectroscopy

by

©Ben Xu

A thesis submitted to the School of Graduate Studies in partial fulfillment of the requirements for the degree of

Doctorate of Philosophy

Department of Physics and Physical Oceanography

Memorial University of Newfoundland

Oct. 2015

St. John's Newfoundland

Abstract

In this thesis, calcite was used as a test case to study the effects of structural disorder on vibrational modes. Vibrational modes were examined using Fourier transform infrared (FTIR) and Raman spectroscopy. Structural disorder was assessed by using X-ray diffraction (XRD) and X-ray absorption fine structure (XAFS) measurements. Data for temperature dependent FTIR, FTIR-photoacoustic (FTIR-PAS), and XAFS measurements were collected at the Canadian Light Source Inc. (Saskatoon, SK).

Four normal vibrational modes of calcite were thoroughly investigated: the symmetric in-plane stretch (ν_1, Raman active), out-of plane bend (ν_2, IR active), asymmetric in-plane stretch (ν_3, IR active), and in-plane bend (ν_4, Raman and IR active). Shapes of the ν_1 and ν_4 peaks are affected by long-range disorder and temperature, while the ν_2 and ν_3 peaks remain unchanged. By comparing the FTIR absorption spectra of different calcium carbonate polymorphs, we suggest that planar carbonate arrangements are the key to cause ν_4 broadening at higher temperatures and with structural defects.

To explore the effects of structural defects in more detail, crystalline domain size, lattice strain, and microstrain fluctuation values were calculated from XRD data. Long-range disorder strongly affects the vibrations in calcite. Bonding distances and coordination environments in calcite based minerals (plasters) were assessed from their XAFS spectra. Results indicate that the local environments are dependent on

the secondary phases (mainly $Ca(OH)_2$) in them. My thesis work demonstrates that paring FTIR with other techniques is more effective for researchers.

Weak peaks related to the combination and isotopic modes in a calcite FTIR absorption spectrum were also well studied. My thesis work demonstrates that weak peaks at 848 cm^{-1} and 1398 cm^{-1} in a FTIR absorption spectrum of calcite are due to the ν_2 and ν_3 vibrations of $^{13}CO_3^{2-}$ rather than combination modes. These two peaks become stronger in spectra of calcite with a higher ^{13}C concentration. Also, the ratio between areas of the 848 cm^{-1} peak and the $^{12}CO_3^{2-}$ ν_2 peak in a FTIR transmittance spectrum match the natural abundance ratio of ^{13}C:^{12}C (near 1%). An interesting phenomenon is that positions of these two peaks do not maintain with ^{13}C concentration changes. Theoretical calculations performed by our colleagues (Anna Hirsch and Dr. Leeor Kronik, Weizmann Institute of Science, Israel) confirm my thesis results.

My thesis work shows that FTIR-photoacoustic (FTIR-PAS) spectroscopy is an appropriate technique to study weak isotopic and combination-mode peaks since they are relatively enhanced under an acoustic detector. Origins of combination-mode peaks were discussed, and quantitative analyses of the ^{13}C ν_2 peak were carried out based on FTIR-PAS spectra. A surprising finding is that the ^{13}C ν_2 mode presents crystallinity dependency, while the ^{12}C ν_2 mode is not.

Acknowledgments

I would like to express the deepest appreciation to my supervisor, Dr. Kristin M. Poduska, for her excellent guidance, caring, patience, and providing me with an excellent atmosphere for doing research. I would like to thank Dr. Tim May, Dr. Ferenc Borondics, Dr. Xia Liu, Dr. Lachlan Maclean and Dr. Yongfeng Hu for guiding my experiments at the Canadian Light Source Inc. They let me experience FTIR and EXAFS measurements, and they patiently taught me how to modify equipment to get reliable data. I would also like to thank Dr. Elisabetta Boaretto and her group for providing archaeological materials, and I thank Dr. Leeor Kronik and his group for their calculations that support my experimental data. Many thanks to Dr. Isai Feldmann and Dr. Wanda Aylward for their help on XRD measurements.

I would like to thank colleagues in Poduska research group for helping me organize and maintain equipment in the lab. Many thanks to Dr. Martin Plumer, Dr. Todd Andrews, Dr. John Whitehead, and Dr. Michael Morrow for their help during studying and researching.

I would like to thank my wife and my family for their support and help in my life. I would never have accomplished this achievement without them.

Lastly, I thank the financial support from Natural Sciences and Engineering Research Council and the Department of Physics and Physical Oceanography and School of Graduate Studies. I also thank the Canadian Light Source Inc. for the Student

Travel Support.

Table of Contents

List of Tables

List of Figures

List of Abbreviations

CCD	charged coupled device
CLSI	the Canadian Light Source Inc.
DFT	density functional theory
EXAFS	extended X-ray absorption fine structure
FTIR	Fourier transform infrared
FWHM	full width at half maximum
IR	infrared
JCPDS	Joint Commission on Powder Diffraction Standards
LO	longitudinal optical
PAS	photoacoustic
TEM	transmission electron microscopy
TO	transverse optical
SXRMB	Soft X-ray Micro-characterization Beamline
XAFS	X-ray absorption fine structure
XRD	X-ray diffraction

List of appendices

Chapter 1

Brief introduction to structural disorder and vibrational modes in solids

1.1 Disorder in solids

The structure of a material is important for its properties and applications. An excellent example is carbon polymorphs. Diamond, graphite and amorphous carbon are distinct due to different arrangements of carbon atoms. Although both diamond and graphite have a periodic arrangement of carbon atoms, their electronic, thermal and mechanical properties are significantly different. Diamond is the hardest natural material in the world and is electrically insulating. It is also transparent to visible light. In contrast, graphite is soft, electrically conductive and has a black color [14]. Amorphous carbon does not have a periodic structure, and its electronic properties strongly depend on the type of coordination (sp^2 or sp^3) of its carbon atoms [15]. Structural study is one of the important aspects of materials research, and understanding the

mechanisms of how structural disorder affects the properties of materials is always one of the primary targets for material researchers.

Depending on the length scales of their structural order, solids can be generally classified into two categories: solids that have a periodic 3D structure are long-range ordered (crystalline), while others are only short-range ordered. There are different ways to disrupt long-range order. For example, the expansion or shrinking of a lattice causes lattice strain in it [16, 17]. Microstrain fluctuations are anisotropic lattice distortions that cause nonuniform strain [13,18]. Substitutional impurities also disrupt long-range order in solids [19, 20].

1.2 Vibrational modes in solids

Although vibrations in real crystals are complicated, the fundamentals can be approximately explained with a simple diatomic system. This system is like a mass and spring model with connected atoms as masses and the chemical bond as the spring. The basic principle has been discussed in many textbooks [7, 8, 21]. Based on McCreery's book [21], the potential energy of the system is approximated by $(1/2)Kq^2$ based on Hooke's law if it performs harmonic oscillations. K is the force constant of the spring and q is the displacement of the oscillator. We can apply the time-independent Schrödinger equation (Equation 1.1) and solve it to get the energy of the system, as defined in Equation 1.2:

$$-\left(\frac{\hbar}{2m}\right)^2 \frac{\partial^2 \Psi}{\partial q^2} + \left(E - \frac{1}{2}Kq^2\right)\Psi = 0 \tag{1.1}$$

$$E_n = \left(n + \frac{1}{2}\right)h\nu \tag{1.2}$$

Here, n is the vibration quantum number, h is the Planck constant, ν is the vibrational frequency of the diatomic system $A-B$ and is given by $(1/2)\sqrt{K/\mu}$ where μ (equal to $(m_A m_B)/(m_A + m_B)$) is the reduced mass of the harmonic oscillators. This predicts the allowed vibration energy states of the diatomic system. $(1/2)h\nu$ is the zero point energy, and the difference between any two energy states is $h\nu$, as shown in Figure 1.1 (a). However, in reality, atoms show anharmonic oscillations and a higher order term is necessary, as shown in Equation 1.3:

$$E_n = \left(n + \frac{1}{2}\right) h\nu - \left(n + \frac{1}{2}\right)^2 hx, \tag{1.3}$$

where x is the anharmonicity constant. A sketch of the energy states of an anharmonic oscillator is shown in Figure 1.1 (b). The energy states of a macroscopic solid with $N \gg 2$ atoms is much more complicated; however, the fundamentals are the same.

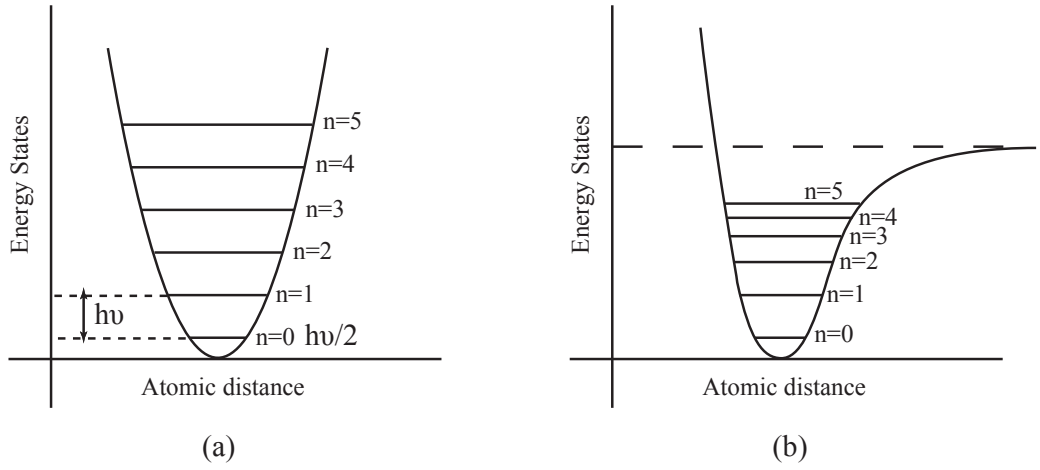

Figure 1.1: A schematic representation of the vibrational energy states for a diatomic system with (a) harmonic and (b) anharmonic oscillations.

Vibrations in a solid usually include lattice modes and internal modes, as well as combination and overtone of them [7]. Lattice modes usually involve relative translations of atoms and are easily affected by disorder within a periodic long-range

structure. Internal modes are the local vibrations of one moiety in the cell (like CO_3^{2-} in carbonate minerals), and these modes strongly depend on (short-range) bonding distances between atoms in the moiety and the atomic masses. Therefore, vibrations in solids contain information about both short-range and long-range features of a solid's structure. Even so, there is still much to be understood about how vibrational spectroscopy can be used to study disorder at different length scales.

1.3 Thesis goals

My research focuses on building the connections between disorder at different length scales and changes to local vibrational modes. I focused on carbonate-containing minerals. My thesis work has two aspects: identifying different types of disorder in carbonate minerals, and detecting the corresponding vibration differences they induce. Based on gaps in previous research, I focused on two main questions:

1. What kinds of structural disorder exists in carbonate-based materials?

2. Can different kinds of disorder be detected in vibrational spectra?

Investigating the link between disorder at different length-scales and vibrations requires understanding of how atomic arrangements determine oscillations in solids. This research is both fundamental and creative since it addresses a knowledge gap related to how changes in long-range disorder affect local vibrational modes. The strategic approach correlates data from different vibration spectroscopy techniques with other X-ray based structure determination methods.

In this dissertation, calcite ($CaCO_3$) is the main study case. It abounds in geological, biological, and archaeological contexts, and the defects in it are strongly dependent on its formation conditions. The vibrational spectra for poorly crystallized calcite are distinct compared to crystallized calcite [22], and this feature is used

to screen for archeological calcite samples [23]. Vibrational spectroscopy was also used to identify amorphous phases in organisms and lab-produced minerals [24, 25].

1.3.1 Structural disorder in calcite-containing minerals

Structural disorder is inevitable during material preparation, and it often brings drawbacks. However, by controlling disorder in materials, people can get novel materials that have remarkable features for promising applications. For example, n-type and p-type semiconductors are produced by introducing low-density impurities [26]. Lattice distortions and strain in thin films are widely acknowledged methods of controlling material properties [27, 28]. Furthermore, studies of structural disorder in minerals can also provide information about their formation conditions and processes, which are significance for geologists and biologists [29–32]. Various techniques have been developed for studying disorder in solids. Transmission electron microscopy (TEM) and X-ray diffraction (XRD) can provide information about periodic structures and strains of solids [33, 34]. X-ray absorption fine structure (XAFS) can give details about local chemical environments [10, 24, 35].

In this dissertation, disorder in calcite samples were thoroughly investigated. By quantitatively analyzing XRD patterns, we obtained information about disruptions to long-range ordered structures in our calcite samples. Local chemical environments were studied with XAFS. XAFS spectra were fitted to get information about coordination numbers, bonding distances, and other parameters related to short-range disorder.

1.3.2 Detection of structural disorder using vibrational spectroscopy

Fourier transform infrared (FTIR) and Raman spectroscopy are commonly used to detect vibrations in solids. Many factors can influence the results, including particle sizes, particle shapes, dilution of powdered samples (especially for infrared (IR)), and fluorescence (especially for Raman scattering). Therefore, although vibrational spectroscopy techniques can give information about disorder in solids, quantitative analyses of their spectra are sometimes difficult. Few studies link structural disorder with detectable signatures in vibrational spectra [30, 36, 37]. In 1974, Keramidas *et al.* studied vibrational modes in ZrO_2 by employing Raman scattering, and they also investigated the crystallinity of ZrO_2 with XRD. They found that specific Raman scattering peaks grow with increasing crystallinity, and they suggested that the Raman scattering peaks can be diagnostic of crystallinity differences [36]. In 1991, other studies showed that specific vibrations in quartz are sensitive to its crystallinity [37]. In 1997, Beniash *et al.* found that the intensities of IR absorption peaks due to calcite internal modes can also provide information about structural disorder [30]. Theoretical calculations were also utilized, and the results indicated that the intensities of IR peaks can change with lattice distortions [38]. More recently, this method was introduced to differentiate among archaeological and geological minerals based on their crystallinity differences [22, 23]. Structural defects also broaden IR peaks, which is due to the decay of phonons through anharmonic coupling [39].

Impurities in a crystal structure also introduce short-range disorder that affects local vibrations. IR measurements on magnesium calcite ($Ca_{1-x}Mg_xCO_3$) indicate that introducing magnesium in calcite (1-80%) will change the positions of IR absorption peaks due to the smaller mass of magnesium atoms relative to calcium atoms [20, 40].

In addition, magnesium brings lattice strain, which also changes vibrations in calcite and makes studying the effects of short-range order complicated [40]. Isotope substitution is also short-range disorder. IR spectra can give clear information about isotopes in both experimental and theoretical results [41–44].

For IR absorption measurements, one common method of preparing samples is to grind them with potassium bromide (KBr) and to press the ground powders into pellets. The particle sizes and the shapes of powders strongly affect the shapes of IR absorption peaks. Large particle sizes, matching the wavelength of the incident light, will cause scattering [45, 46]. For example, the Christiansen effect [45] caused by scattering will cause asymmetrical peak shapes, making the analyses of peaks complicated and unreliable. Therefore, powders must be finely ground to eliminate scattering. The intensities of IR peaks also strongly depend on the concentration of samples in pellets. Comparing the relative intensities of IR peaks from the same spectrum is a helpful strategy and can be used to identifying atomic disorder [22, 23, 47]. Another issue is that some IR peaks (combination and isotopic peaks) are very weak, and the analyses of these peaks are sometimes difficult.

Although Raman scattering is less affected by sample preparation, the fluorescence effect is a serious issue [48]. Fluorescence is usually present in Raman spectra of natural samples since they commonly contain luminescent impurities such as Mn or Fe, and the noise due to the fluorescence is usually not negligible for natural samples [48].

1.4 Overview of the thesis

The structure of a solid contains information about its formation and transformation which is important to researchers. Many techniques have utilized by others to study structural differences, and vibrational spectroscopy is one of them. However, the

abilities of vibrational spectroscopy to differentiate among structural differences and identifying their origins are not completely understood. This dissertation investigates the influences of structure on the vibrations in calcite to see if the origins of structural differences can be identified by using vibrational spectroscopy. My thesis work indicates that vibrational spectroscopy can provide information about structural differences, although it is challenging to distinguish different types of structural disorder and to identify their origins.

This dissertation is divided into 8 chapters, and FTIR, Raman, XRD, and XAFS techniques were utilized. In Chapter 3, IR spectra of carbonate polymorphs with different structures were measured at different temperatures in order to find out which vibrational modes are most sensitive to temperature, and if that is correlated with changes in structural disorder. In Chapter 4, different types of long-range defects were examined by XRD measurements in order to correlate their effects on the IR spectra of calcite. In Chapter 5, XAFS, XRD, and FTIR measurements were carried out on different calcite-based plaster samples in order to demonstrate effects of short-range disorder on the vibrations and the carbonation process. In Chapter 6, calcite samples with varying ^{13}C contents were synthesized and examined by FTIR and Raman spectroscopy, and the effects of isotopic "defects" on vibrations were investigated. In Chapter 7, FTIR-Photoacoustic (PAS) spectroscopy was used to explore the effects of structural disorder on isotopic peaks from different calcite samples.

Chapter 2

Experimental details

2.1 Calcium carbonate polymorphs

Calcite ($CaCO_3$) is the main study case in this dissertation. Researchers did many studies on calcium carbonate polymorphs using vibrational spectroscopy techniques [11, 41, 49, 50]. Utilizing FTIR spectroscopy, my collaborators developed a new approach for distinguishing archaeological calcite from geological calcite [22, 23]. Computational studies showed that theoretical calculations of vibration modes match experimental results for many different calcium carbonate polymorphs [1, 43, 44, 51].

2.1.1 Previous studies on calcium carbonate polymorphs

Calcium carbonate is abundant in natural materials, such as geogenic rock, mollusc shells, and coral reefs [23, 52, 53]. Due to the differences in formation conditions, calcium carbonate can crystallize in many different polymorphs, including calcite, aragonite and vaterite.

The crystal structures of these three calcium carbonate polymorphs are shown in Figure 2.1. Calcite is the most stable phase under ambient conditions, and has a

rombohedral unit cell with the space group of $R\bar{3}C$. Its structure is often described as hexagonal. There are two planes of carbonate ions in calcite, and one is rotated at 60° with respect to the other. Two sets of anions are arranged on different planes. The lattice constants a and b are 4.99 Å, and c is 17.06 Å. They vary slightly with different reports [2, 54].

Aragonite is less stable than calcite [55], and it is in the space group of $Pmcn$ with α=β=γ=90°. The arrangement of carbonate ions in aragonite differs from that of calcite. Four sets of carbonate ions form into staggered layers. Based on De Villiers's study, the lattice constants are a=4.9614 Å, b=7.9671 Å, and c=5.7404 Å; other results are consistent with these findings [4, 56].

The stability of vaterite under ambient condition is even worse. Carbonates in it are disordered which makes structure analysis quite complicated, thus its true crystal structure is still under debate [5, 57, 58].

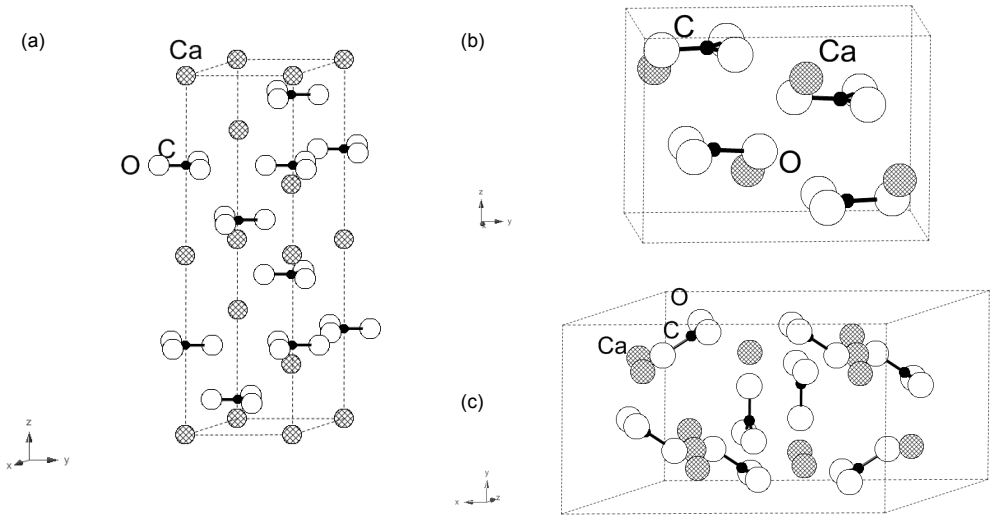

Figure 2.1: Representations of the crystal structures of (a) calcite [2], (b) aragonite [4], and (c) vaterite [5]. The data used to generate these diagrams are from American Mineralogist Crystal Structure Database [6]. Parts of this figure are repeated in Chapter 3 for convenience.

The formation of calcium carbonate polymorphs and the transformation among

them have been studied for decades [4, 56, 59]. It is reported that vaterite and aragonite transform to calcite at temperatures near 690 K, and that calcite is the most energetically favorable phase [55, 60]. However, many living organisms can selectively form calcite, aragonite or vaterite [5, 52]. In 1991, Falini *et al.* studied the formation of aragonite and calcite in mollusk shells, and found that specific macromolecules are responsible for the precipitation of either aragonite or calcite on the shells [52]. The transient amorphous calcium carbonate phases in organisms forming into crystallized phases were also reported for many times [12, 24, 30, 31].

2.1.2 Vibrational modes in calcite

In one calcite unit cell, there are two $CaCO_3$ units containing 10 atoms, resulting in 27 allowed vibrational modes. The calculated frequencies of these vibrational modes are listed in Table 2.1 based on Ref. [1]. Vibrations at lower wavenumbers (lower than 500 cm^{-1}) are the lattice modes, which correspond to relative translations of the carbonate and calcium ions. Vibrations higher than 700 cm^{-1} are internal vibrations of carbonate ions, generally called internal normal modes. The internal modes for carbonate ions are shown in Figure 2.2. One carbonate ion can have 4 normal modes: symmetric stretching (ν_1), out-of-plane bending (ν_2), asymmetric stretching (ν_3), and in-plane bending (ν_4). In calcite, the ν_1 and ν_2 modes are Raman and IR active, respectively, while ν_3 and ν_4 can be observed in both IR and Raman spectra. Apart from the internal modes and lattice modes, combined modes (which are the overtones of two more normal modes) can also be detected by IR and Raman techniques.

Table 2.1: The frequencies of vibrations in calcite based on Ref. [1]. For TO and LO modes of IR active vibrations, "TO" stands for "transverse optical", and "LO" stands for "longitudinal optical".

	symmetry	wavenumber (cm^{-1})
Raman active	E_g	155.9
	E_g	276.6
	E_g	710.9
	A_{1g}	1088.4
	E_g	1432.4
IR active	E_u (TO)	124.9
	(LO)	139.6
	A_{2u} (TO)	126.1
	(LO)	159.5
	E_u (TO)	219.6
	(LO)	230.7
	E_u (TO)	285.9
	(LO)	379.4
	A_{2u} (TO)	298.9
	(LO)	402.6
	E_u (TO)	711.5
	(LO)	712.9
	A_{2u} (TO)	874.4
	(LO)	894.2
	E_u (TO)	1400.1
	(LO)	1554.4
Silent modes	A_{2g}	192.9
	A_{1u}	288.6
	A_{2g}	311.4
	A_{2g}	882.3
	A_{1u}	1088.3

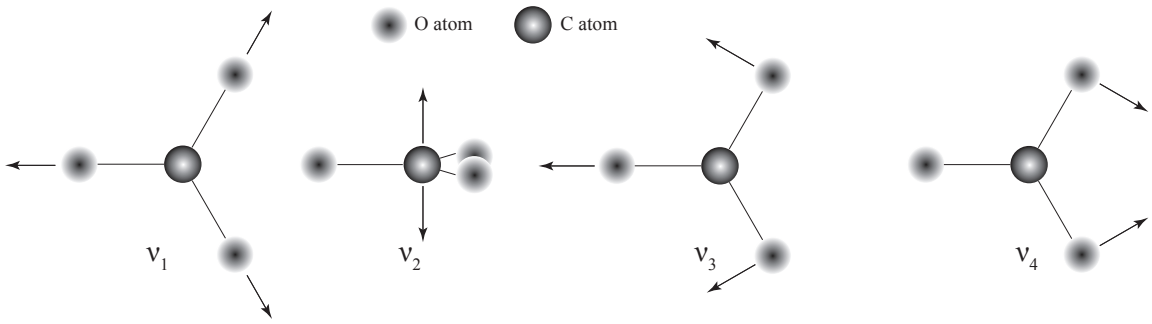

Figure 2.2: Normal internal modes of a carbonate ion (CO_3^{2-}).

2.2 Sample details

My thesis focuses on calcite and other carbonate minerals. Based on their origins, the samples I used can be divided into three categories. Sample details are listed in Table 2.2 and Table 2.3. Geogenic, archeological, and lab-produced samples have different types of defects and structures in them, and were mainly used for studying the influences of long-range disorder on vibrational features of calcite. Plaster and lime samples more disordered than lab-produced and geogenic samples, and their local-environments were compared to demonstrate that vibrations were mainly affected by long-range disorder.

2.2.1 Geogenic minerals

Calcite spar, aragonite spar, flowstone, and dolomite rock are the geogenic materials used in this thesis. Calcite spar is a pure single crystal of geogenic calcite and was from Mexico [23, 55]. Aragonite spar is a pure single crystal of geogenic aragonite and was from Spain [55]. Flowstone is usually formed on floors or walls of a cave due to the deposition of calcite from drip water. Our flowstone samples were collected in Manot cave (Israel) [61]. Flowstone samples were provided by Dr. Miryam Bar-

Matthews and Dr. Avner Ayalon (Geological Survey of Israel). We also thank Dr. Omry Barzilai (Israel Antiquities Authority) with Prof. Israel Hershkovitz (Tel Aviv University) and Dr. Ofer Marder (Ben Gurion University) who led the excavations at Manot Cave. Calcite spar was provided by Dr. Elisabetta Boaretto (Weizmann Institute of Science, Rehovot, Israel) . Dolomite rocks are the natural aggregate of dolomite ($Mg_{0.5}Ca_{0.5}CO_3$), and they were collected in Newfoundland by Dr. Kristin M. Poduska.

2.2.2 Archeological calcite (ancient plaster)

Archeological calcite was collected from a historical site of Yiftahel (Israel) by Lior Regev, supervised by Dr. Steven Weiner and Dr. Elisabetta Boaretto (Weizmann Institute of Science, Rehovot, Israel) [23]. Previous studies of this archeological calcite have been published and suggested that archeological calcite contains well crystallized calcite [22,23]. We thank Dr. Ianir Milevski and Dr. Hamudi Khaily (Israel Antiquities Authority) who led the excavations at Yiftahel.

2.2.3 Lab-produced $CaCO_3$ polymorphs

Lab-made samples include analytical-grade calcite, synthesized calcite, and synthesized vaterite. Analytical-grade calcite was bought from Merck company [23, 55]. Calcite and vaterite samples were synthesized in two steps. First, 25 mL of 5 mM Na_2CO_3 was placed in a flask and immersed in an ultrasonic bath at room temperature, after which 1 mL of 60 mM $CaCl_2$ was added every 15 seconds during the course of 6 minutes, for a total of 25 mL. To produce vaterite, suspensions were left at room temperature; calcite formed when suspensions were stored at 4 °C. After one hour, the suspensions were centrifuged for 15 minutes at 4200 rpm, the supernatant was removed, and products were air-dried. This method does not always produce vaterite.

Table 2.2: Sample details of $CaCO_3$ polymophs.

sample	origin
calcite spar	Chihuahua, Mexico
aragonite spar	Minglanilla, Spain
flowstone (calcite)	Manot Cave, Israel [61]
dolomite rock ($Mg_5Ca_{0.5}CO_3$)	Port au Choix, Newfoundland
glycymeris shell (aragonite)	Ashkelon, Israel [55]
ancient plaster	Yiftahel, Israel
analytical-grade calcite	Merck
synthesized calcite	lab-produced [62]
synthesized vaterite	lab-produced [62]

I made samples using this method 3 times, and only 2 products contained vaterite.

2.2.4 Lab-produced plaster and lime

Lab-produced plaster was provided by Michael B. Toffolo, supervised by Dr. Elisabetta Boaretto (Weizmann Institute of Science, Rehovot, Israel). The method for preparation of plaster and lime can be described by the following chemical reactions [23, 55]. Lime powders from decomposing $CaCO_3$ polymorphs were slaked with deionized water, producing a thin plaster paste. Both the lime powders and plaster pastes were left to cure in ambient conditions for years. The temperatures and date for preparing lime and plaster samples are given in Table 2.3.

$$CaCO_3 \overset{heating}{\longrightarrow} CaO \text{ (lime)} + CO_2$$

$$2\ CaO + H_2O + CO_2 \longrightarrow CaCO_3 + Ca(OH)_2$$

$$Ca(OH)_2 + CO_2 \longrightarrow CaCO_3 + H_2O \text{ (plaster)}$$

Table 2.3: Sample details of lab-produced plaster and lime.

starting material	heating temperature	preparation date
plaster		
calcite spar	800 °C	February, 2012
calcite spar	900 °C	February, 2012
analytical-grade calcite	800 °C	February, 2012
analytical-grade calcite	900 °C	February, 2012
aragonite spar	800 °C	February, 2012
aragonite spar	900 °C	February, 2012
glycymeris shell	800 °C	February, 2012
glycymeris shell	900 °C	February, 2012
lime		
calcite spar	900 °C	May, 2012
analytical-grade calcite	900 °C	May, 2012
aragonite spar	900 °C	May, 2012
glycemeris shell	900 °C	May, 2012

2.3 Material characterization techniques

2.3.1 Vibrational spectroscopy

Fourier transform infrared (FTIR) and Raman spectroscopy were utilized to study the vibrational modes of calcium carbonate polymorphs in this thesis. Normally, Raman and IR can give complementary information about vibration modes of a material [7,8]. Vibrational spectra are influenced by structural detail at short- and long-range length scales [12, 23, 36, 63–67].

2.3.1.1 Fourier transform infrared (FTIR) spectroscopy

Vibrations in a solid can cause oscillatory electric fields that have the same frequency as the molecule vibration. The changing electric field can interact with an electromagnetic wave. Through this, the vibration can absorb the photon energy when incident light also has the same frequency. Since the frequency of the molecule vibration is usually in the infrared region, infrared spectroscopy is often utilized to give information about vibration modes in materials [7, 8, 68].

Fourier transform infrared (FTIR) spectroscopy is the most widely used version of the IR technique [7]. Its core part is the Michelson interferometer, as shown in Figure 2.3. Incident IR beams with a range of wavenumbers (500 cm^{-1} to 4000 cm^{-1} for this thesis work) are separated into two beams with the same intensities by a splitter. They are then reflected back by mirrors and interfere with each other. One of the two mirrors is fixed, and by moving the other mirror in a few millimeters, an interferogram (the beam intensity *vs.* mirror displacement) is recorded. The Fourier transformed interferogram produces a spectrum. Two spectra are collected during one FTIR measurement, one for the sample and the other for the background. By removing the background signal from the sample spectrum, an absorption/transmittance spectrum is then acquired.

FTIR is widely used to detect a material's components. Take calcium carbonate polymorphs and dolomite ($(CaMg)(CO_3)_2$) as examples. Representative FTIR spectra of three $CaCO_3$ polymorphs are shown in Figure 2.4. It is obvious that each material has a unique vibrational spectrum.

In this thesis, FTIR measurements were done with a Bruker Vertex 70v/S spectrometer using either synchrotron IR light (Mid-IR beamline 01B1-1 at Canadian Light Source Inc., Saskatoon, SK and a Hyperion 3000 microscope) or a globar IR source (in the Poduska lab at Memorial University of Newfoundland). The measuring range was typically 4000-500 cm^{-1}. Samples were ground together with spectrophotometric grade potassium bromide and the mixed powders were pressed into 3 mm diameter pellets under 2 tons. The analysis of IR absorption peaks utilized OPUS 7.0 (Bruker Inc.) or Igor 6.6 software (WaveMetrics Inc.) [69, 70]. The background was removed and peak heights and positions were recorded. For peak widths, a reliable method was to fit each individual peak to the Lorentzian function using Igor 6.6 software.

2.3.1.2 Raman spectroscopy

Solids can only absorb photon energy through oscillating electric dipole moments. Therefore, when a vibration in a solid does not cause a changing dipole, it does not have an absorption peak in its IR spectrum. In this case, Raman spectroscopy can be utilized to detect this vibrational mode [8, 21]. Rather than absorption, Raman spectroscopy utilizes the scattering effect between photons and vibrations. As described elsewhere [8], the oscillating electric field (E) of the incident light as a function of time (t) is given by Equation 2.1:

$$E = E_0 \; cos\left(2\pi\nu_0 t\right), \tag{2.1}$$

where E_0 and ν_0 are the amplitude of the electric field and the frequency of the light. Then the electric dipole moment (P) can be expressed as

$$P = \alpha E = \alpha E_0 \; cos\left(2\pi\nu_0 t\right). \tag{2.2}$$

α is known as the polarizability, which is the key to Raman scattering. In a vibration, the atomic displacement (q) will be

$$q = q_0 \; cos\left(2\pi\nu_{vib} t\right) \tag{2.3}$$

ν_{vib} is the frequency of the vibration. Since the polarizability is proportional to atomic displacement at short range, the polarizability can be rewritten as

$$\alpha = \alpha_0 + \left(\frac{\partial\alpha}{\partial q}\right)_0 q, \tag{2.4}$$

and therefore, the dipole moment will be

$$P = \alpha_0 E_0 \; cos\,(2\pi\nu_0 t) + \left(\frac{\partial\alpha}{\partial q}\right)_0 q E_0 \; cos\,(2\pi\nu_0 t)\,. \tag{2.5}$$

Combining Equation 2.3 and Equation 2.5, we have

$$\begin{aligned} P &= \alpha_0 E_0 \; cos\,(2\pi\nu_0 t) + \left(\frac{\partial\alpha}{\partial q}\right)_0 q_0 \; E_0 \; cos\,(2\pi\nu_0 t) \;\; cos(2\pi\nu_{vib} t) \\ &= \alpha_0 E_0 \; cos\,(2\pi\nu_0 t) \\ &\quad + \frac{1}{2}\left(\frac{\partial\alpha}{\partial q}\right)_0 q_0 \; E_0 \;\; \{cos\,[2\pi(\nu_0 + \nu_{vib})t] + cos\,[2\pi(\nu_0 - \nu_{vib})t]\}\,. \end{aligned} \tag{2.6}$$

The first term in Equation 2.6 is related to Rayleigh scattering, in which the scattered light has the same frequency as the incident light. The second term comes from Raman scattering, as shown schematically in Figure 2.5. Raman scattering is inelastic, thus the frequency of the scattered light is different from the incident light and the energy difference is the same as the vibration energy. From Equation 2.6, we can find that Raman scattering can only happen when $(\partial\alpha/\partial q)_0$ is not zero. Therefore, the polarizability change is the essence of the Raman scattering.

In this thesis, a Renishaw inVia Raman Microscope 90Q314 with the Renishaw laser source was employed for the Raman measurements. The wavelength for the Raman laser is 633 nm and its maximum power is 500 mW. The measuring range for Raman measurements was typically 3000-100 cm^{-1}. Samples for Raman measurements were powders. The scattered photons are captured by a CCD (Charge Coupled Device) detector to give a Raman spectrum. Raman peaks can be fitted by a Lorentzian function, and Igor 6.6 software (WaveMetrics Inc.) was employed for data analyses.

2.3.2 X-ray diffraction

X-ray diffraction (XRD) is commonly utilized for studying crystal structure [71, 72]. The sample is exposed to monochromatic X-rays which results in the scattering of incident light by the crystal planes. The scattered light can produce constructive interference only when Bragg's law (Equation 2.7) is satisfied:

$$n\lambda = 2dsin\theta \tag{2.7}$$

Here, n is an integer, λ is the X-ray wavelength, d is the distance between crystal planes and θ is the angle of incident light. Bragg's law is explained graphically in Figure 2.6. The path difference between the two reflected rays is $2dsin\theta$. If they interfere constructively, $2dsin\theta$ must be an integral number of wavelengths. There are different crystal planes in a crystal, and each crystal plane has the Bragg condition met at a distinct incident angle. Based on the angle of each XRD peak, plane distances and lattice constants can be calculated. However, if the sample is poorly crystallized, XRD will be of little help. A typical powder XRD pattern of calcite is shown in Figure 2.7. The angle of each peak is labeled with their hkl indices.

In this thesis, XRD measurements employed a Rigaku Ultima IV with Cu Kα source equipped with a monochrometor. Powdered samples were exposed to X-rays using a 2 θ range of 20° to 90°, a step size of 0.02°, and a count time of one second. XRD data were analyzed using JADE 7.0 software. The background was removed, and JCPDS (Joint Commission on Powder Diffraction Standards), such as 88-1807 for calcite, were used for comparison [9]. The XRD peaks were then fitted individually to get accurate widths (full width at half maximum (FWHM)) and positions. Lattice constants were calculated from the 2-θ value of the diffraction peaks. The Williamson-Hall method was employed to calculate microstrain fluctuation values and crystalline

domain sizes [18, 33, 73].

2.3.3 The Canadian Light Source Inc.

A portion of my data was collected at the Canadian Light Source Inc. (Saskatoon, SK), including all the X-ray absorption fine structure (XAFS) data, the FTIR spectra for temperature dependent measurements, and the FTIR-photoacoustic (FTIR-PAS) spectra. The dates we spent at the Canadian Light Source Inc. were from 2012-05-15 to 2012-05-20, from 2012-09-28 to 2012-10-06, from 2013-05-08 to 2013-05-13, and from 2013-10-08 to 2013-10-15.

Synchrotron radiation is emitted when charged particles are radially accelerated [74, 75]. We utilized synchrotron radiation for two reasons: a) the synchrotron beam has high intensity that enables rapid measurements on our samples and makes it possible to focus on a small region; b) their microscope stage and temperature control stage allowed us to do measurements that we cannot do in our own lab.

We used the soft X-ray Micro-characterization Beamline 06B1-1 and Mid-IR Beamline 01B1-1 at CLSI for XAFS and FTIR measurements, respectively. Temperature control systems for heating and cryogenic experiments were used in the Mid-IR lab. Heating experiments used a nitrogen-purged temperature-controlled stage (Instec HCS601 Microscope Hot and Cold stage with MK1000 series High Precision Temperature Controller). Low-temperature data were collected with a liquid-nitrogen-cooled stage (Cryo Industries of America RC102-CFM Microscopy Cryostat with a controller from Cryogenic Control Systems) while under vacuum at 1×10^{-6} torr. Dr. Ferenc Borondics, Dr. Tim May and Dr Xia Liu helped us set up the equipment. Data were collected by Dr. Kristin M. Poduska and myself. I analyzed all data.

2.3.4 X-ray absorption fine structure (XAFS)

The local environment of our samples was determined by employing X-ray absorption fine structure (XAFS) measurements. An XAFS measurement includes extended X-ray absorption fine structure (EXAFS) and X-ray absorption near edge structure (XANES) spectra. An EXAFS spectrum can give the information about local environment of a solid, and an XANES spectrum is usually used to determine the composition of a sample [10, 12, 25]. The fundamental of XAFS is shown in Figure 2.8 (a). Core electrons will absorb the energy of X-ray photons and be promoted out of the atom, leaving core holes. Meanwhile, electrons at higher energies will drop into the core holes, emitting photons. Both the ejected electrons and emitted photons can be detected. For each kind of atom, its characteristic X-ray absorption energies are well defined and an absorption edge will be observed in its XAFS spectrum, as shown in Figure 2.8 (b). For an isolated atom, the absorption probability at energies higher than the absorption energy E_0 is smooth as shown in Figure 2.8 (b). In a real solid, since that ejected electrons scatter with neighboring atoms, an EXAFS spectrum always oscillates as shown in Figure 2.8 (c). The oscillations induced by the neighboring atoms contain information about the local structure.

For XAFS measurements, the absorption coefficient μ_0 is proportional to I_f/I_0, where I_f is the intensity of fluorescence or electron emission and I_0 is the intensity of incident X-ray. Since the oscillation well above absorption edge contains information about local structure, the EXAFS data is contained in this expression [76]:

$$\chi(E) = \frac{\mu(E) - \mu_0(E)}{\delta\mu_0(E)} \tag{2.8}$$

where $\mu_0(E)$ is the "bare atom" background and $\delta\mu_0(E)$ is the “edge step” as shown in Figure 2.8 (c). $\chi(E)$ can be written in terms of the photo-electron wavenumber k

based on $k = \sqrt{2m(E - E_0)/\hbar^2}$. The oscillation decays fast with k and are usually multiplied by k^2 or k^3 to enhance the signal during the data analyses (k^2 was employed in this thesis). The EXAFS spectrum of K-edge of Ca atoms in calcite is shown in Figure 2.9 (a) as an example. The EXAFS spectrum can be Fourier transformed to get the bonding distances between Ca atoms and other atoms in calcite in real space, as shown in Figure 2.9 (b).

Further quantitative analysis on the EXAFS spectrum by employing the EXAFS function can give precise information about local environment in a solid. Equation 2.9 is the EXAFS function and the oscillation extracted from the EXAFS signal can be fitted to it [76]:

$$\chi(k) = \sum_j \frac{N_j f_j(k) e^{-2k^2\sigma_j^2}}{kR_j^2} \sin\left[2kR_j + \delta_j(k)\right] \tag{2.9}$$

where $f(k)$ and $\delta(k)$ are the scattering amplitude and the phase-shift, respectively, which are properties of the neighboring atoms and are already known. N is the coordination number and R is the distance to the neighboring atom. $e^{-2k^2\sigma_j^2}$ is known as the Debye-Waller factor and accounts for the variation in the bonding distances [77]. Therefore, N, R and σ^2 can be calculated with the known constants of $f(k)$ and $\delta(k)$.

XAFS measurements were performed at the Soft X-ray Micro-characterization Beamline 06B1-1 (SXRMB) at the Canadian Light Source Inc.(CLSI) in Saskatoon, SK. Data were collected by Dr. Kristin M. Poduska and me. We were both trained in data analysis by CLSI beam line scientists (Dr. Lachlan Maclean and Dr. Yongfeng Hu). After getting initial help from Dr. Lachlan Maclean, I did all the analysis using the IFEFFIT software package [78]. A typical XAFS spectrum of analytical-grade calcite (Merck) is shown in Figure 2.10 (a). The EXAFS signal $\chi(E)$ was defined as $((E) - \mu_0(E))/\Delta\mu_0$, where $\mu(E)$ is the measured XAFS value, $\mu_0(E)$ represents an

Table 2.4: The 5 closest neighbours around a Ca site in calcite, based on Markgraf's results [2].

bond	distance
Ca-O	2.36 Å
Ca-C	3.21 Å
Ca-O	3.46 Å
Ca-Ca	4.05 Å
Ca-O	4.28 Å

isolated calcium atom and $\Delta\mu_0$ indicates the increase of $\mu(E)$ at an energy well above the absorption edge as shown in Figure 2.10 (a). The EXAFS spectrum weighted by k^2 is presented in Figure 2.10 (b), and its Fourier transformed spectrum in a real space is presented in Figure 2.10 (c). Peak positions in Figure 2.10 (c) are usually underestimated by about 0.5 Å compared to real bonding distances because of the phase correction during a Fourier transform [76]. The k region for Fourier transform is from 2 $Å^{-1}$ to 9 $Å^{-1}$ as shown in Figure 2.10 (b). The 5 closest neighbors of a calcium atoms are listed in Table 2.4. Therefore, we know that the strong peaks at 1.8 Å and 3.4 Å indicate Ca-O and Ca-Ca bonding in calcite, and the two weak peaks in between represent Ca-O and Ca-C bonding. Quantitative analysis of the EXAFS spectrum was performed using Artemis software [78]. The crystallographic data of calcite used was from Markgraf's results [2]. The first coordination shell of ideal calcite cell was calculated and fitted to the EXAFS spectra by using Artemis software, as presented in Figure 2.10 (c), with fit parameters of bonding distance in the first coordination shell, and the variation of scattering path.

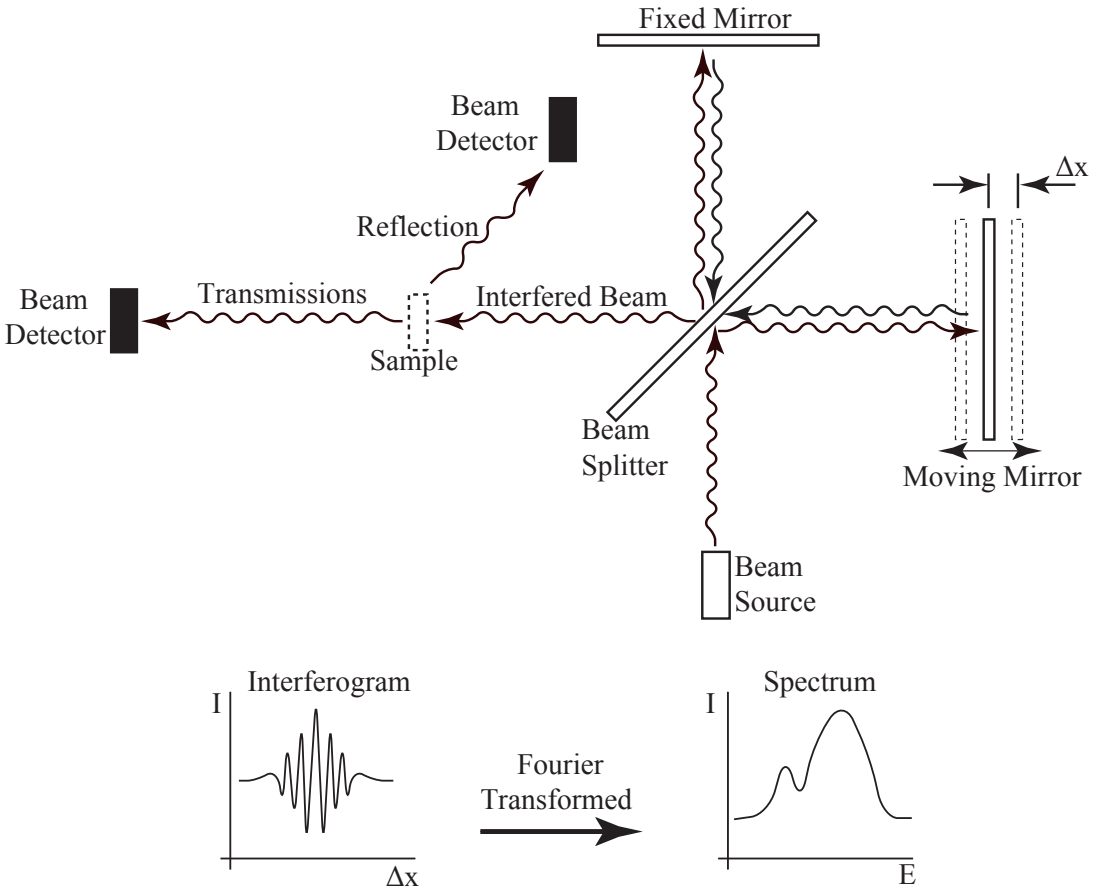

Figure 2.3: A schematic picture of the fundamentals of FTIR technique, especially its use of the Michelson interferometer. Two beams with the same intensity are produced by a beam splitter and reflected by two mirrors (one of them is movable and the other one is fixed). Two reflected beams interfere with each other, producing an interferogram. A Fourier transformed interferogram gives an IR spectrum. The sketch is based on Ref. [7].

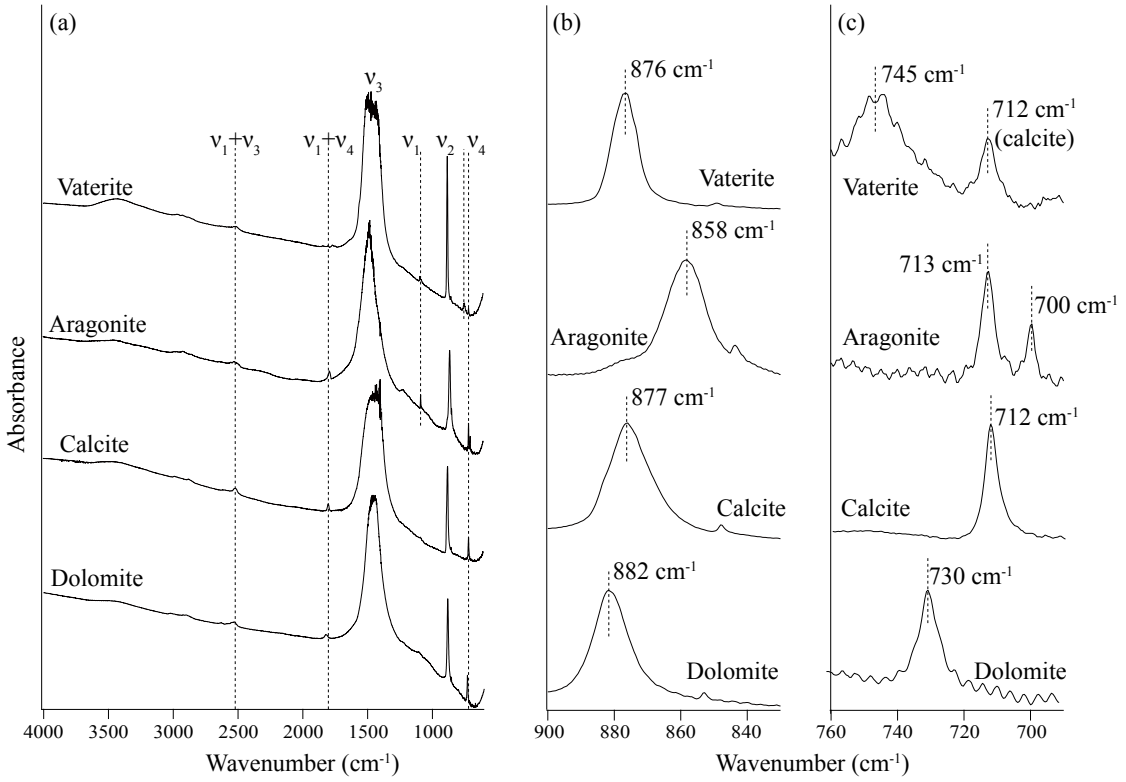

Figure 2.4: FTIR absorption spectra of calcite, aragonite, and vaterite. Spectra are shifted along the vertical axis for clarity. ν_3 peaks shown in (a) have noisy shapes because they are saturated (completely) absorbing. This is often necessary in this thesis to get better signal for the lower intensity peaks, such as ν_4 regions (c). (b) presents the ν_2 regions for these carbonate minerals.

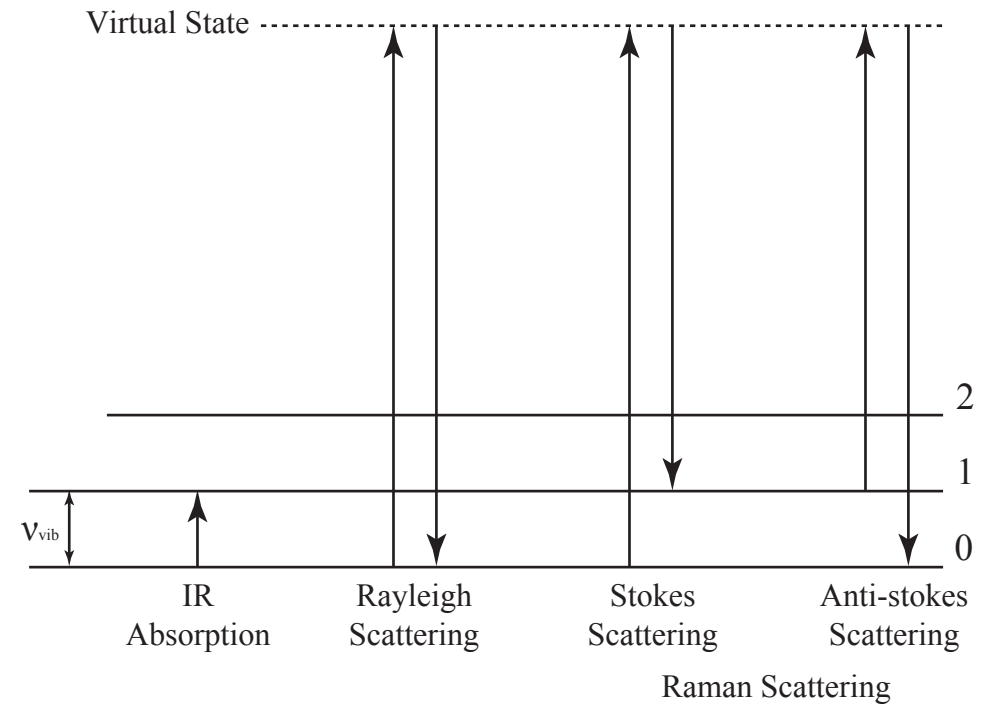

Figure 2.5: Schematic comparison of IR absorption, Rayleigh scattering and Raman scattering, based on Ref. [8].

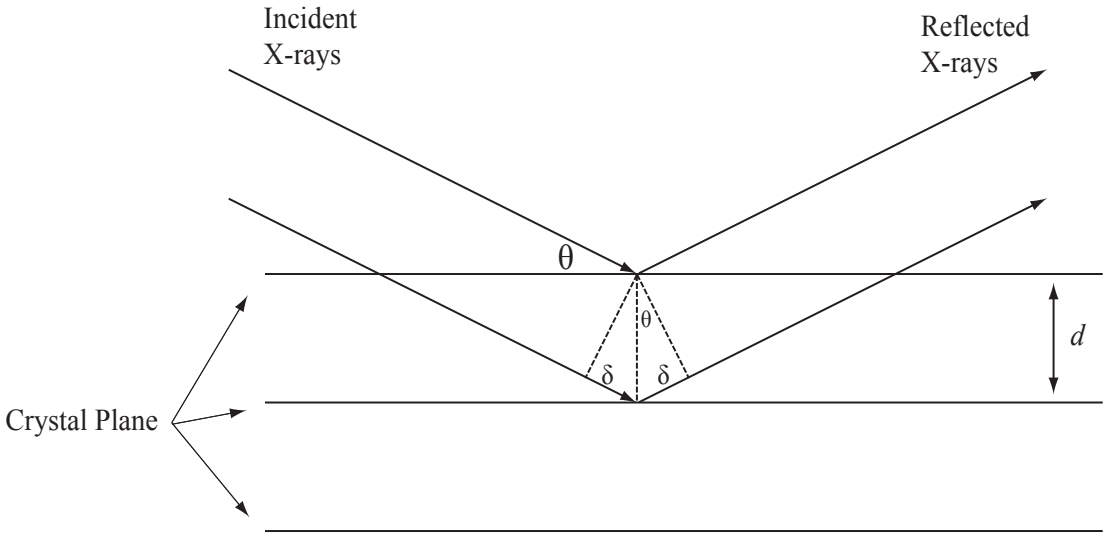

Figure 2.6: A schematic picture of the Bragg diffraction condition for X-ray diffraction.

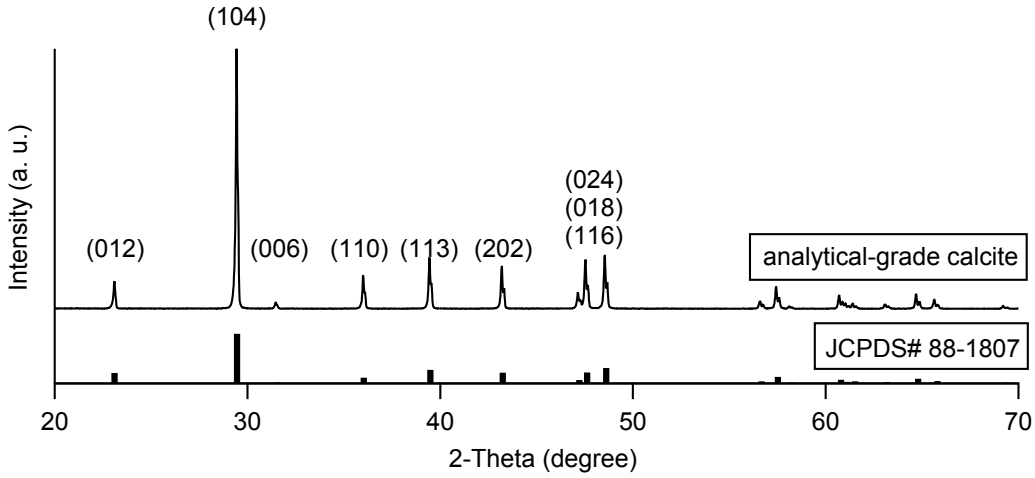

Figure 2.7: The XRD pattern for crystalline calcite. The crystal plane (*hkl* indices) for each XRD peak is labeled. The standard pattern is from JCPDS [9].

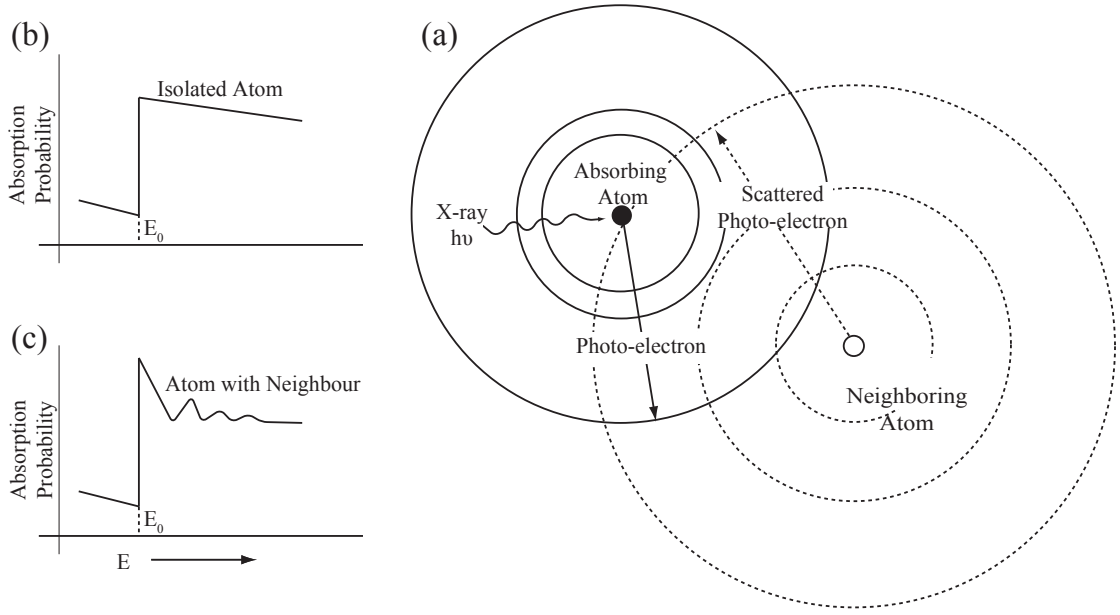

Figure 2.8: A schematic picture of the fundamentals of XAFS, based on Ref. [10].

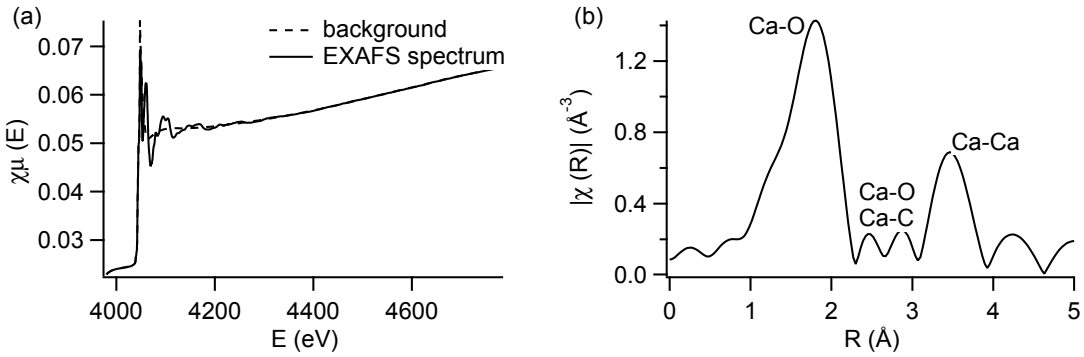

Figure 2.9: The XAFS spectrum from (a) the K-edge of Ca atoms in calcite and (b) the Fourier transformed EXAFS result in real space.

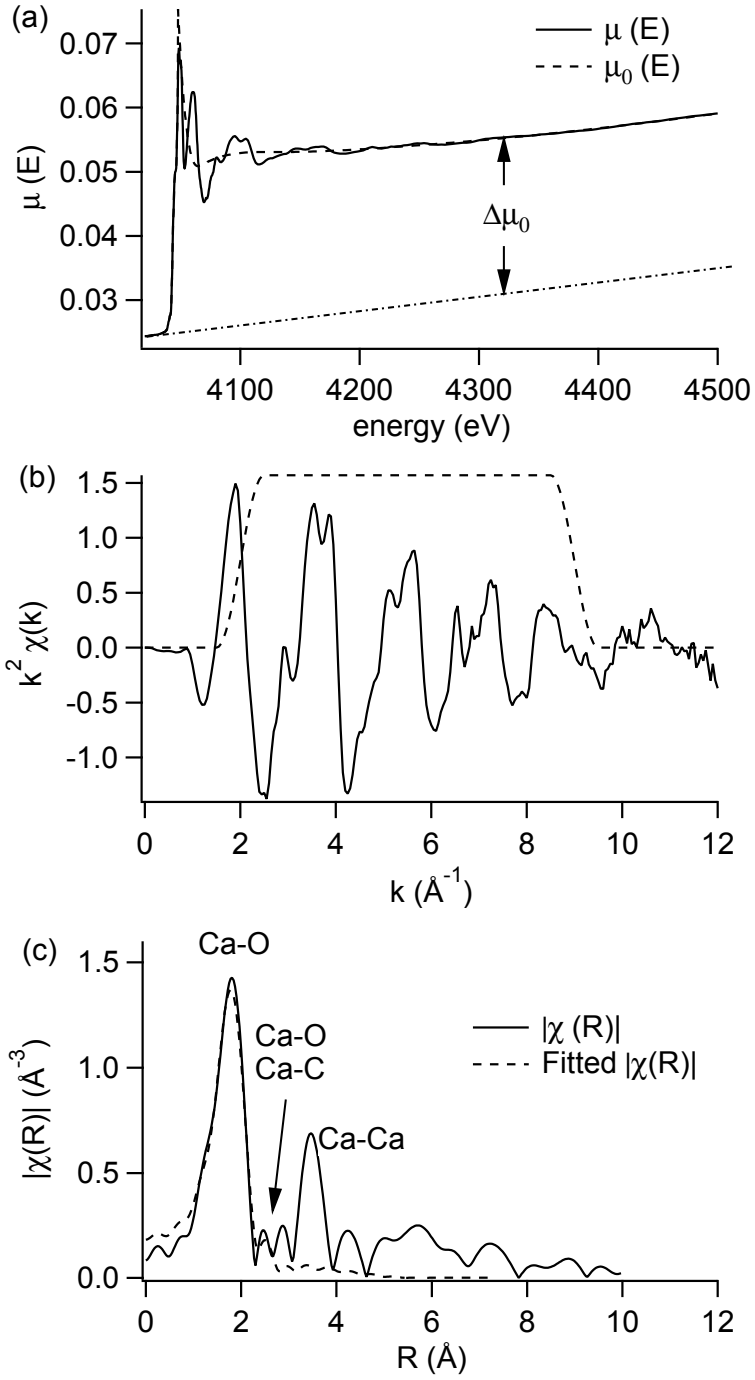

Figure 2.10: (a) XAFS spectrum of analytical-grade calcite (Merck). (b) EXAFS weighted by k^2. (c) Fourier transform of EXAFS at real space and the fitted first coordination shell.

Chapter 3

Linking crystal structure with temperature-sensitive vibrational modes in calcium carbonate minerals

This chapter was published as "Linking crystal structure with temperature-sensitive vibrational modes in calcium carbonate minerals" Ben Xu and Kristin M. Poduska. *Phys. Chem. Chem. Phys.*, Vol. 16, Page 17634, 2014. Used with permission.

3.1 Abstract

We demonstrate a correlation between how an IR-active vibrational mode responds to temperature changes and how it responds to crystallinity differences. Infrared (IR) spectroscopy was used to track changes in carbonate-related vibrational modes in

three different $CaCO_3$ polymorphs (calcite, aragonite, and vaterite) and $CaMg(CO_3)_2$ (dolomite) during heating. Of the three characteristic IR-active carbonate modes, the in-plane bending mode (ν_4) shows the most pronounced changes with heating in polymorphs that have planar carbonate arrangements (calcite, aragonite, and dolomite). In contrast, this mode is virtually unchanged in vaterite, which has a canted arrangement of carbonate units. We correlate these trends with recent studies that identified the ν_4 mode as most susceptible to changes related to crystallinity differences in calcite and amorphous calcium carbonate. Thus, our results suggest that studies of packing arrangements could provide a generalizable approach to identify the most diagnostic vibrational modes for tracking either temperature-dependent or crystallinity-related effects in IR-active solids.

3.2 Introduction

Fourier transform infrared spectroscopy (FTIR) has been used to study the constituents of naturally occurring and laboratory synthesized sample for decades. Since sample preparation methods and measurement geometries can have dramatic effects on the widths and intensities of FTIR peaks, there has been a general disregard for quantitative comparisons of structural order from such spectra. However, recent studies have demonstrated that differences in long-range periodicity (crystallinity) can be extracted from FTIR spectra [22,38,39,67,79]. Calcite has been an excellent test case because it has three well separated IR absorption bands [4, 65, 80, 81], and because there are a range of different degrees of crystalline order that it can accommodate, ranging from amorphous to single crystalline. In other materials, such as apatite, the effects of crystallinity on peak widths can be more challenging to track when there are overlapping IR bands [82–84]. FTIR has proven to be useful for tracking phase tran-

sitions in geological samples [82], developing screening techniques for archaeological materials [23], and for characterizing biominerals [79, 84].

In this work, we investigate the temperature dependencies of peak positions and peak widths in FTIR spectra from different carbonate minerals (geogenic sources of spar calcite, spar aragonite, and dolomite), as well as laboratory-prepared samples of calcite and vaterite. We find that there are different temperature dependencies for two prominent vibrational modes, and that these differences correlate with the packing arrangements for the carbonate units in the different crystal structures. Our analyses suggest that crystallinity differences and temperature dependent differences affect vibrational modes in these carbonate materials in a similar manner. This offers a new way to help identify vibrational modes that could be indicators for crystallinity differences by using temperature-dependent spectral data.

3.3 Experimental details

Geogenic carbonate samples included calcite spar (Chihuahua, Mexico), aragonite spar (Minglanilla, Spain), and dolomite (Port au Choix, Newfoundland, Canada). Representative powder X-ray diffraction data, shown in Figure 3.1, confirm the phase compositions of these geogenic samples. Calcite (space group $R\bar{3}C$, compared with JCPDS 83-1762) has $a = 4.990(1)$ Å and $c = 17.063(3)$ Å, dolomite (space group $R\bar{3}C$, compared with JCPDS 75-1655) has $a = 4.816(3)$ Å and $c = 16.02(1)$ Å, and aragonite (space group $Pmcn$, compared with JCPDS 71-2396) has $a = 4.967(4)$ Å, $b = 7.96(1)$ Å,and $c = 5.746(5)$ Å. All XRD data were collected using a Rigaku Ultima IV with Cu Kα radiation, lattice constant refinements from Jade (Materials Data Inc.) were compared with JCPDS standards [9].

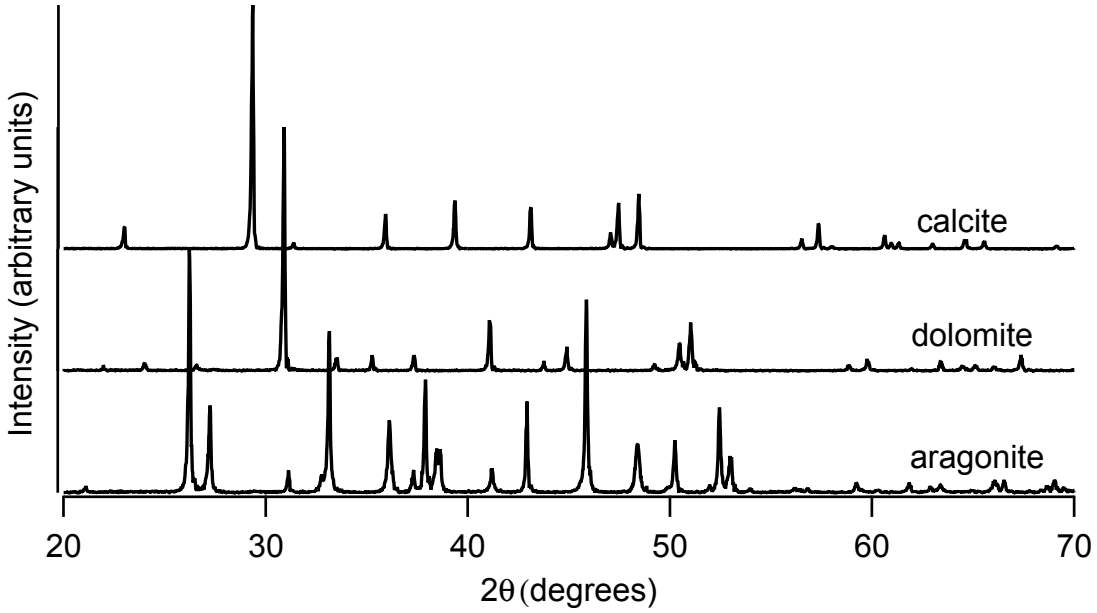

Figure 3.1: Representative powder X-ray diffraction spectra at room temperature for spar calcite, geogenic dolomite, and spar aragonite. Lattice constant refinements of these data yield values in good agreement with JCPDS standard patterns [9].

Synthesized calcite and vaterite were made in two steps. First, 25 mL of 5 mM Na_2CO_3 was placed in a flask and immersed in an ultrasonic bath at room temperature, after which 1 mL of 60 mM $CaCl_2$ was added every 15 seconds during the course of 6 minutes, for a total of 25 mL. To produce vaterite, suspensions were left at room temperature; calcite formed when suspensions were stored at 4 °C. After one hour, the suspensions were centrifuged for 15 minutes at 4200 rpm, the supernatant was removed, and products were air-dried.

FTIR measurements used a Bruker Vertex 70v vacuum spectrometer connected to a Hyperion 3000 IR microscope with a liquid-nitrogen-cooled single-element HgCdTe (MCT) detector. The system is attached to beamline 01B1-1 at the Canadian Light Source (Saskatoon, SK, Canada), and this bright IR source enabled very short data

acquisition times. Spectra for the carbonate samples were measured in transmission (in the range of 4000-500 cm^{-1} with 1 cm^{-1} resolution). For this, specimens were ground with spectrophotometric grade KBr, pressed into 7 mm diameter pellets under 2 tons, and the resulting pellet was affixed to the mounting stage with thermal epoxy. To obtain better signal to noise for the two peaks of interest (ν_2 and ν_4), uncharacteristically high amounts of carbonate sample were used in the KBr pellets (approximately 1:20 by weight). For this reason, the most intense peak (ν_3) is saturated in all spectra shown in this work.

Heating experiments used a nitrogen-purged temperature-controlled stage (Instec HCS601 Microscope Hot and Cold stage with MK1000 series High Precision Temperature Controller). Spectra were collected while heating from 293 K to 773 K at 25 K intervals, letting the temperature equilibrate for 30 minutes prior to each measurement. For each sample, spectra were collected from the same 250 μm diameter spot throughout the entire heating run.

Low-temperature data were collected with a liquid-nitrogen-cooled stage (Cryo Industries of America RC102-CFM Microscopy Cryostat with a controller from Cryogenic Control Systems) while under vacuum at $1{\times}10^6$ torr. Samples were cooled to 77 K, then spectra were collected at 20 K intervals while warming from to 298 K, letting the temperature equilibrate for 30 minutes at each temperature step. At each temperature, spectra were collected at 5 different 250 μm diameter spots.

Spectra were baseline corrected with Bruker OPUS 7.0 software, after which the peak positions, amplitudes, and full width at half maximum (FWHM) values were extracted from Lorentzian peak fits (Wavemetrics IgorPro v6.31). Lorentzian functions are widely utilized for peak fitting in IR and Raman spectra [85, 86], and recent studies have demonstrated that the IR-active ν_2 and ν_4 modes in calcite are well matched by this function [20]. For accurate comparisons, the same wavenumber re-

gions were fitted across all temperature ranges for each different mineral phase: calcite (ν_2 at 800–960 cm^{-1}, ν_4 at 660–760 cm^{-1}), aragonite (ν_2 at 780–920 cm^{-1}, ν_4 at 660–760 cm^{-1}), vaterite (ν_2 at 800–960 cm^{-1}, ν_4 at 680–780 cm^{-1}), and dolomite (ν_2 at 800–960 cm^{-1}, ν_4 at 700–760 cm^{-1}).

3.4 Results

At room temperature, different polymorphs of $CaCO_3$ (calcite, aragonite and vaterite) and the Mg-carbonate dolomite have clearly distinguishable X-ray diffraction patterns (Figure 3.1) and FTIR spectra (Figure 3.2). The vibrational modes associated with these FTIR peaks have been well documented in the literature [4,80], and our results are in good agreement. We find that the out-of-plane bend ν_2 (near 870 cm^{-1}) and the in-plane bend ν_4 (near 720 cm^{-1}) are the only distinct peaks in the mid-IR range that can be fit well with a single Lorentzian function across all four mineral phases. Thus, the ν_2 and ν_4 modes are the ones that we consider in detail here. Some of the remaining vibrational modes in these carbonates present overlapping peaks, including ν_3 (near 1450 cm^{-1}), and combined modes $\nu_1 + \nu_4$ and $\nu_1 + \nu_3$ (near 1800 cm^{-1} and 2500 cm^{-1}, respectively) [81]. Unlike calcite and dolomite, aragonite and vaterite have IR active ν_1 modes at 1082 cm^{-1} and 1090 cm^{-1}, respectively. Aragonite also has an additional peak in the ν_4 range, as noted in Figure 3.2c.

FTIR spectra for calcite (lab-synthesized and geogenic spar), vaterite, aragonite, and dolomite were monitored while heating from 293 K to 768 K at 25 degree increments. Additional experiments at low temperatures were carried out on lab-synthesized and geogenic spar calcite. Figure 3.3 illustrates representative temperature-dependent peak trends for calcite. Others have reported that calcite bonding distances expand and that carbonate ions distort at high temperatures [2,87]. This is consistent

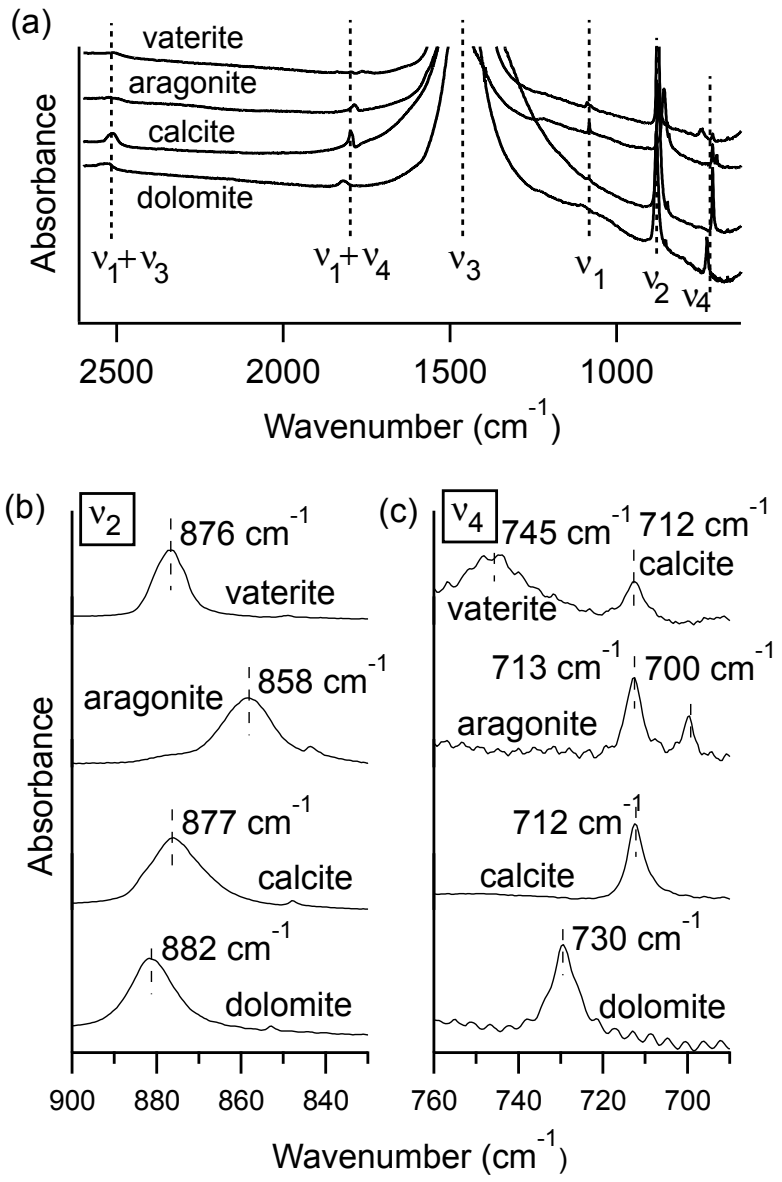

Figure 3.2: Representative FTIR spectra at room temperature for lab-synthesized vaterite, spar calcite, spar aragonite and geogenic dolomite, showing (a) full spectra, (b) the ν_2 modes, and (c) ν_4 modes. Spectra are scaled and shifted along the vertical axis for clarity. High amounts of sample were used to boost the signal to noise for the ν_2 and ν_4 peaks, which leads to saturated absorbance unit values for the strongest (ν_3) peak; for this reason the full ν_3 peak is not shown in (a).

with our findings, since both ν_2 and ν_4 peaks shift to lower wavenumbers and decrease in intensity with increasing temperature in both lab-synthesized and geogenic calcite. However, there are other temperature-dependent changes to these two spectral peaks as well. First, ν_4 broadens with increasing temperature, while in contrast, the ν_2 peak width is nearly constant (Figure 3.4). Second, the ν_4 peak intensity decreases more rapidly than the ν_2 intensity as temperature increases.

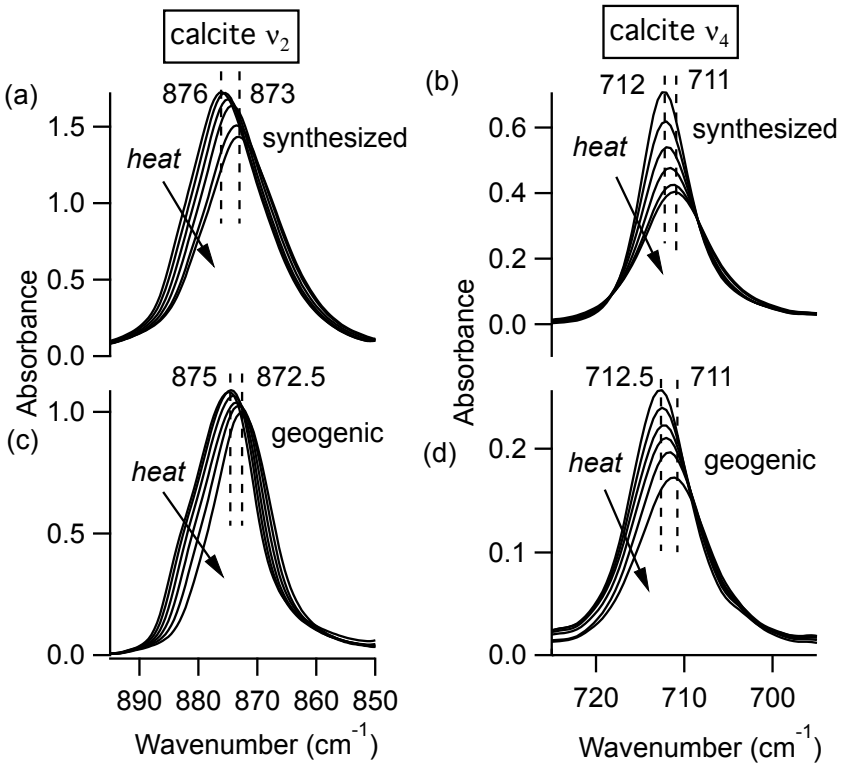

Figure 3.3: FTIR spectra for lab-synthesized calcite (a,b) and geogenic spar calcite (c,d) at different temperatures. The arrows indicate that the ν_2 and ν_4 peaks shift to lower wavenumber values and have smaller amplitudes at higher temperatures.

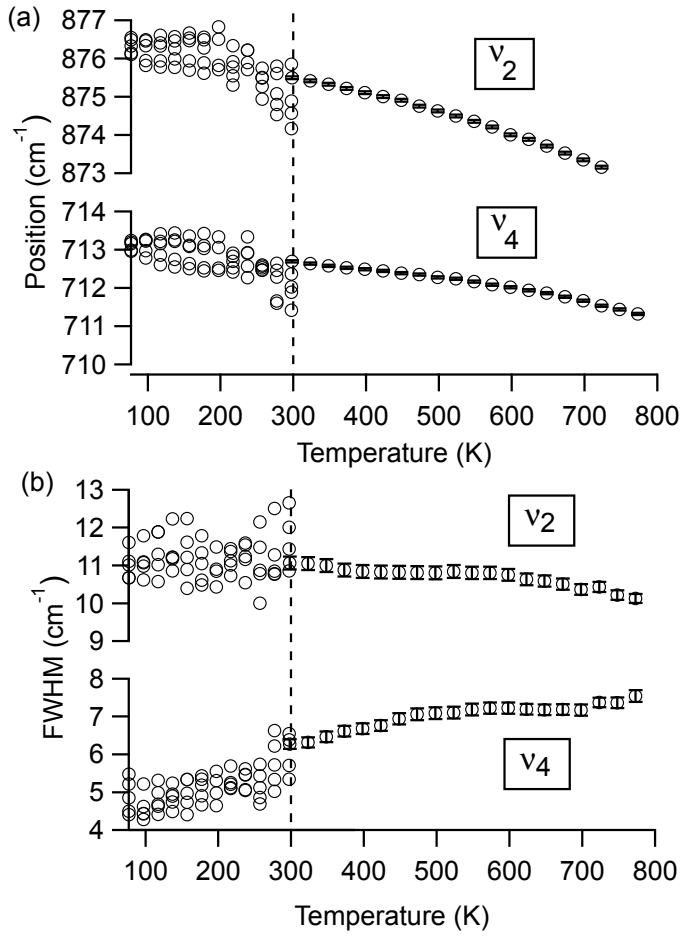

Figure 3.4: Temperature-dependent changes to (a) peak position and (b) FWHM values for ν_2 (out-of-plane bend) and ν_4 (in-plane bend) for spar calcite. Data below room temperature were collected in many different areas of the KBr pellet, contributing to more scatter. Data above room temperature show the trend at a single spot. Error bars account for the uncertainty associated with the Lorentzian peak fits, and are generally contained within the size of the data marker symbol.

A comparison of high-temperature effects to FTIR peaks among all four types of carbonate minerals is provided in Table 3.1. The comparison temperature (598 K) is below any possible phase transitions. As a rule, peak positions show a slight shift to

lower wavenumbers upon heating. The lone exception is the aragonite ν_4 peak near 700 cm^{-1}, which moves to a higher wavenumber. The peak width trends show more pronounced differences. Dolomite, calcite, and aragonite show very little change in the ν_2 FWHM, while the ν_4 peak broadens with increasing temperature. Vaterite behaves differently, with its ν_2 and ν_4 peaks both showing constant widths during heating.

Table 3.1: Summary of high temperature changes (at 598 K, relative to 293 K) to the out-of-plane ν_2 and in-plane ν_4 bending modes. Data are compared for calcite (lab-synthesized and geogenic spar), aragonite, vaterite, and dolomite. Note that aragonite has two distinct ν_4 peaks at 713 cm^{-1} and 700 cm^{-1}.

Mode	Sample	δ Position (cm^{-1})	δ FWHM (cm^{-1})	δ FWHM/ $FWHM_{RT}$
ν_2	calcite synth	-1.7 ± 0.1	-0.3 ± 0.3	-2 ± 2%
	calcite spar	-1.5 ± 0.1	-0.3 ± 0.3	-2 ± 3%
	dolomite	-2.5 ± 0.1	0.5 ± 0.2	4 ± 2%
	aragonite	-2.3 ± 0.1	1.5 ± 0.5	9 ± 3%
	vaterite	-2.2 ± 0.1	-0.1 ± 0.2	2 ± 2%
ν_4	calcite synth	-0.7 ± 0.1	1.8 ± 0.2	42 ± 5%
	calcite spar	-0.7 ± 0.1	1.0 ± 0.3	15 ± 4 %
	dolomite	-1.9 ± 0.2	3.4 ± 0.3	48 ± 5%
	aragonite (713)	-0.4 ± 0.1	1.6 ± 0.4	40 ± 10%
	aragonite (700)	1.0 ± 0.3	2.6 ± 0.9	90 ± 40%
	vaterite	-2.2 ± 0.3	0.3 ± 1.1	2 ± 8 %

At temperatures above 598 K, our experiments demonstrate that both aragonite and vaterite undergo phase transitions to form calcite, as reported by others [60]. The ν_4 peaks are most indicative of these changes, shown in Figure 3.5. The aragonite peak

at 700 cm^{-1} disappears above 698 K (Figure 3.5a), and the vaterite peak near 740 cm^{-1} disappears above 748 K (Figure 3.5b). Up to the maximum heating capacity of our high temperature stage (768 K), dolomite shows no evidence of a phase change (Figure 3.5c). For calcite, Figure 3.4 indicates that there are no statistically significant discontinuities in the ν_4 or ν_2 peak positions or widths. For example, the small changes that occur to the calcite peak widths near 700 K (Figure 3.4b) are within the range of the error bars on each data point. Therefore, calcite does not show any evidence of a phase change within the temperature range of the present study.

3.5 Discussion

Changes in the IR spectra of solid materials during heating can be related to changes in the crystal lattice (such as phase transitions) or to the anharmonic nature of vibrations within the material [88, 89]. In the present study, the maximum measurement temperatures were safely below the decomposition temperature for calcite and dolomite ($\sim$1000 K), but aragonite and vaterite each convert to calcite within this temperature range (at 748 K and 698 K, respectively) in agreement with the literature [60]. For this reason, we choose to focus on the changes to spectral peak widths and positions that occur at temperatures below any phase transitions in these materials.

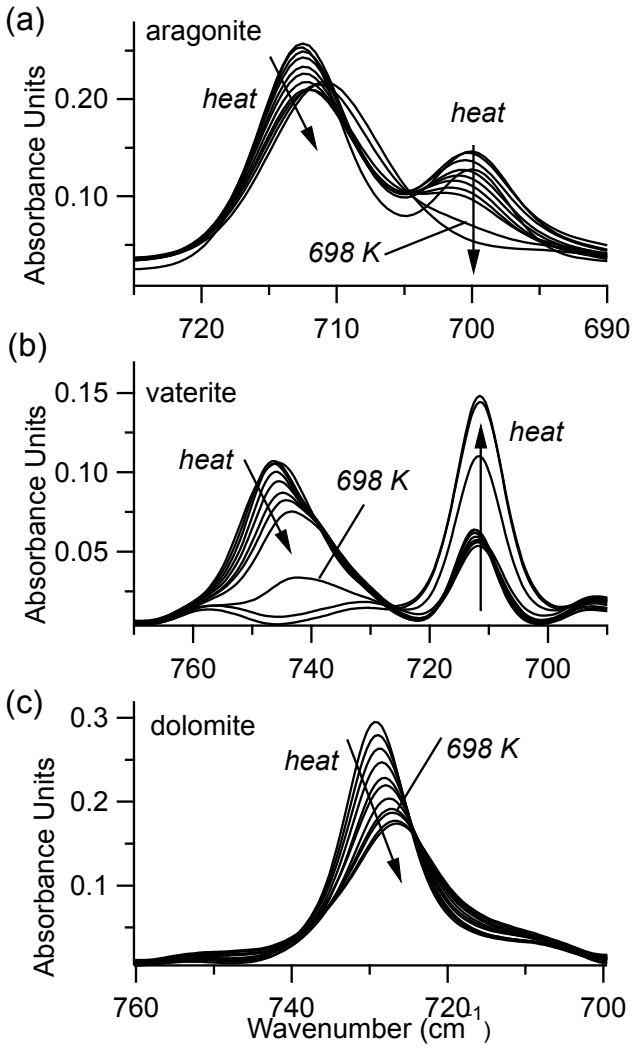

Figure 3.5: FTIR data in the ν_4 region show that high temperatures cause a phase change to calcite in vaterite (a) and aragonite (b), but not in dolomite (c). In each plot, the spectrum corresponding to 698 K is noted for clarity.

In simple terms, adding thermal energy to a solid can provide information about the degree of anharmonicity of the atomic interaction potentials. For example, larger shifts in peak positions with a given temperature change signify a softer, more anharmonic interatomic potential. Recently, these kinds of effects have been explored

in the temperature-dependent IR peak positions and width trends in apatite and kaolinite [39, 90, 91]. They employed a simple model to describe weakly anharmonic oscillations and their quantum saturation limit at low temperatures [92]. In brief, these previous works report a linear temperature dependence for peak widths and positions at higher temperatures, which they attribute to anharmonic effects. However, below some threshold temperature, the temperature dependence diminishes, and peak widths and positions are constant; this is assumed to be the result of quantum saturation. Thus, there is an effective minimum peak width that can be achieved for a given IR vibrational mode once the material is cooled below a specific temperature threshold. This threshold temperature is determined empirically rather than from calculations, due to the complex and varied factors that contribute to spectral peak shapes and positions in real systems.

In the present study, we find that four calcium carbonate minerals (calcite, dolomite, aragonite, and vaterite) do not show a particularly strong temperature dependence in their peak positions or widths when compared to apatite or other minerals [39]. Our working temperatures (298–768 K) appear to be far above the quantum saturation limit for the ν_4 peak, since their widths show approximately linear temperature dependences in all four carbonates. However, the ν_2 peak width shows little change, suggesting that the quantum saturation temperature for this mode is far above ambient temperatures.

To explore these saturation effects in more detail, Figure 3.4 shows low temperature peak width and position data for calcite ν_2 and ν_4 from many different microscopic regions of a sample. We achieved this by collecting numerous spectra at different areas on a KBr-embedded pellet sample, knowing that the spatial arrangement of the calcite particles within the KBr matrix will be slightly different at each location, and thus the peak widths will be slightly different due to differences in scattering effects (data below

300 K in Figure 3.4). However, the spatial arrangement of particles at any given spot remains fixed during the course of the temperature-dependent measurements, since the calcite is not mobile in the KBr matrix. Therefore, collecting spectra from a single spot as the temperature changes shows peak width changes that are due solely to temperature-dependent effects (data above 300 K in Figure 3.4). We note that the spread in peak widths at different measurement spots (low temperature data in Figure 3.4) introduces scatter to the data that is larger than the temperature-dependent trends that we can detect while measuring at a single location (high temperature data in Figure 3.4). However, even with this large scatter, it is evident that the ν_2 peak widths at higher temperatures are not statistically different than at lower temperatures. This is not the case for the ν_4 peak widths, since there is a clear decrease in peak width with temperature.

For both ν_2 and ν_4, the peak position changes are significant. Following the analysis of others [39], we extrapolate slopes (-0.0049 $\pm$ 0.0009 cm^{-1}/K, -0.0012 $\pm$ 0.001 cm^{-1}/K) with corresponding 0 K peak positions (876.9 $\pm$ 0.2 cm^{-1}, 713.2 $\pm$ 0.1 cm^{-1}) for ν_2 and ν_4, respectively. The larger slope for the ν_2 peak position change suggests that mode has a softer interatomic potential relative to the ν_4 mode.

From these temperature dependent data, we notice two interesting trends. First, in all minerals, the ν_2 peak (out-of-plane bend) has a width that is statistically unchanged with heating. Second, the ν_4 peak (in-plane bend) does broaden with increasing temperature for calcite, aragonite, and dolomite, but not for vaterite. To explain the relative differences in the behavior of the in-plane and out-of-plane bending modes among these four different carbonate minerals, we look to differences in their crystal structures (Figure 3.6).

Of the three pure calcium carbonates, calcite is the most stable phase under ambient temperature and pressure conditions (space group $R\bar{3}C$, with reported lattice

constants of $a = 4.99$ Å and $c = 17.10$ Å) [54]. All of its carbonate moieties lie in-plane, rotated at 60° to each other within a single plane. Dolomite is isostructural to calcite, but it has smaller lattice constants since it has ∼50% Mg replacing Ca. Aragonite is less stable thermodynamically under ambient conditions when compared to calcite. Its carbonate ions exist in staggered layers (space group $Pmcn$, with $a = 4.9614$ Å, $b = 7.9671$ Å and $c = 5.7404$ Å based on earlier reports [4, 56]). Vaterite is even less stable than aragonite under ambient conditions, making it extremely rare in natural environments. Partial carbonate occupations and distortions have made definitive analysis of its structure quite complicated and the focus of considerable debate [57, 58]. Nevertheless, its non-planar arrangement of the carbonate units is a unique feature among the four carbonate minerals addressed in this study.

As described above, carbonate moieties have four possible vibrational modes, which are ν_1 (in-plane symmetric stretching), ν_2 (out-of-plane bending), ν_3 (in-plane asymmetric stretching) and ν_4 (in-plane bending) [65]. In dolomite, calcite and aragonite, the carbonate ions are arranged in layered structures and their ν_2 mode (out-of-plane) is less affected by temperature changes than the ν_4 (in-plane) mode. On the other hand, vaterite has carbonate units that are canted relative to each other and not in layers, and there are also partial occupancies that lead to built-in disorder. We propose that it is this structural difference – the non-planar arrangement of carbonate units – that makes the vaterite ν_4 mode less changed as a function of temperature.

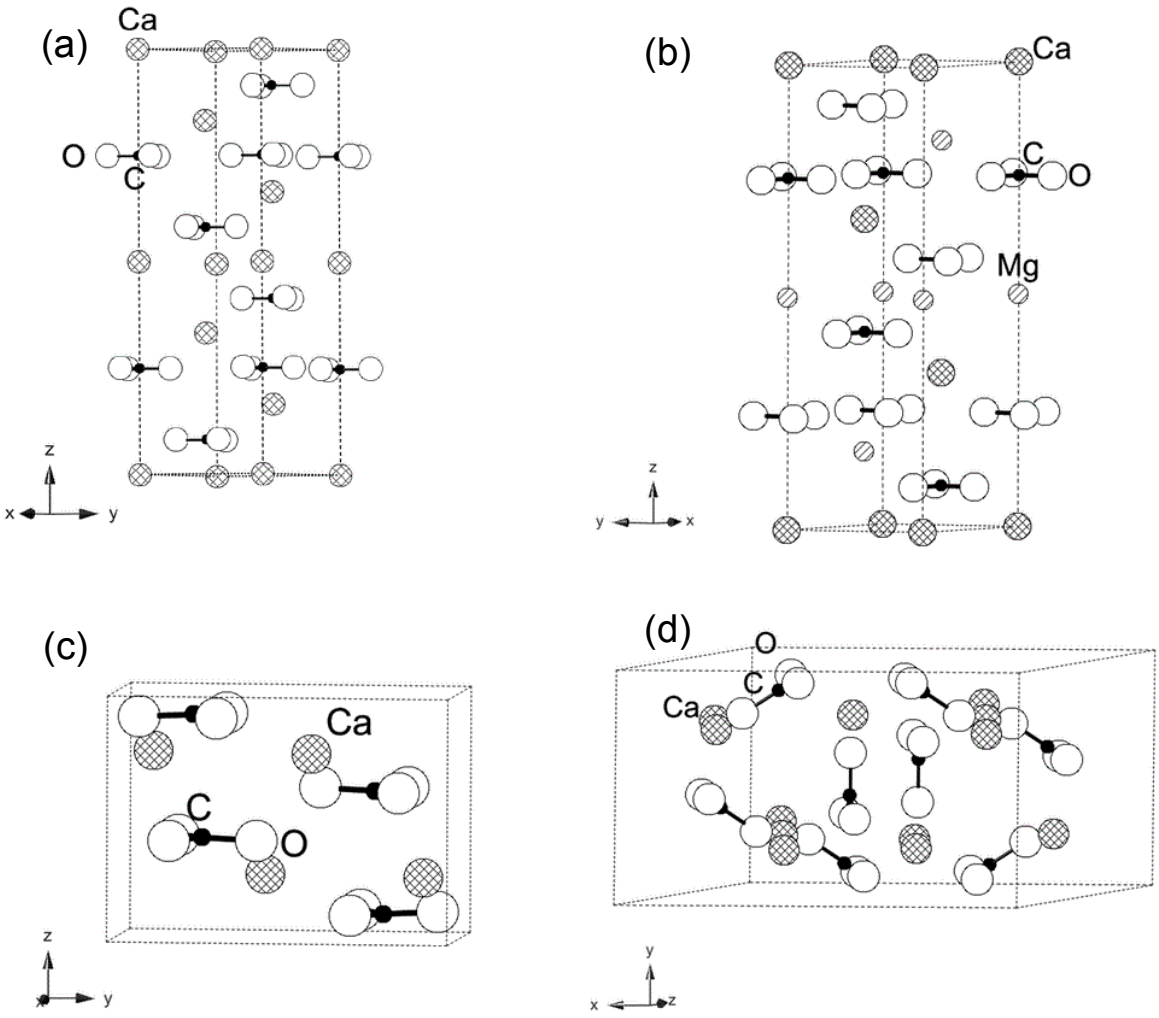

Figure 3.6: Schematic representations of crystallographic unit cells for (a) calcite and (b) isostructural dolomite, as well as (c) aragonite and (d) vaterite.

It is noteworthy that there are other reports of ν_4 peak width changes in calcium carbonate phases, albeit in a different context. Recent studies based on experiments and density functional theory (DFT) demonstrate that the calcite ν_4 peak broadens significantly more than ν_2 when going from highly crystalline structures to a truly amorphous structure [38]. The authors conclude that peak broadening, without a shift in peak position, is consistent with poorer long-range periodicity in calcite. At first

glance, it might appear that comparing crystallinity differences (mixtures of amorphous and crystalline calcite) with temperature-dependent spectral features (changes in the anharmonicity of the vibrational modes) is not straightforward. However, we suggest that it is significant that the same peak (ν_4) is most affected in both scenarios. For calcite, this in-plane bending mode appears to be the most responsive to changes in its structural environment, whether those changes are due to temperature or structural disorder. For example, we note that there is slightly larger temperature-dependent broadening in the ν_4 peak for our rapidly-formed laboratory-synthesized calcite compared with the geogenically formed spar calcite (Table 3.1). To extrapolate this link between temperature and structural disorder with other carbonate minerals beyond calcite is somewhat speculative, since theoretical studies are lacking. The DFT studies that work well in demonstrating the peak broadening between amorphous calcium carbonate and calcite cannot easily be extended to compare with other $CaCO_3$ polymorphs [38], since the energy minima for these different structures are quite similar [1, 93].

3.6 Conclusions

Extending the idea of tracking crystallinity-dependent peak signatures with temperature-dependent experiments to cases beyond carbonate-containing minerals is an intriguing possibility, and it has not been explored. There are many potential materials that could be candidates for future studies. For example, there are reports of using features from vibrational spectra to track differences in crystallinity in silicon to identify the presence and proportion of amorphous components [66]. In this case, factor analysis showed that Raman spectra exactly two independent spectra features, one of which can be attributed to crystalline Si while the other is assigned to amorphous Si.

Others have identified a crystallinity-sensitive IR mode in SiO_2 that corresponds to an octahedral site that is easily disrupted in the Si-O tetrahedral network [67], and temperature-dependent studies in glassy SiO_2 have also be studied [94]. Crystallinity has also been tracked in experimental studies of apatite and aragonite [30, 79, 84].

One possible advantage of using temperature as screening strategy for crystallinity dependent vibrational modes is that one sample is all that is needed. This could be a more time-effective option when detailed theoretical calculations are not feasible.

3.7 Acknowledgments

We thank M. Toffolo and E. Boaretto (Weizmann Institute of Science, Israel) for spar calcite and spar aragonite samples, and F. Borondics, T. May, and X. Lu at the Mid-IR beamline at the Canadian Light Source.

Chapter 4

Structural differences in archaeologically relevant calcite

This chapter will be published as "Structural differences in archaeologically relevant calcite" Ben Xu, Michael B. Toffolo, Lior Regev, Elisabetta Boaretto, and Kristin M. Poduska. *Anal. Methods*. Accepted on Sep. 30, 2015. Used with permission.

4.1 Abstract

We show that two different sources of calcite (geogenic flowstones and anthropogenic lime plaster) have complex, yet distinctive, structural disorder signatures. It is effective to identify these differences by pairing a rapid, fieldwork-compatible technique (Fourier transform infrared (FTIR) spectroscopy) with a robust laboratory-based technique (X-ray diffraction (XRD) peak width analyses). We demonstrate that crystalline domain size, microstrain fluctuations, and lattice strain each affect the FTIR spectra of calcite. To focus on each variable separately, XRD data and FTIR ab-

sorption spectra are compared among calcite samples formed by different processes. Small crystalline domain sizes cause changes to FTIR peak intensity ratios (grinding curves). However, larger microstrain fluctuations or larger lattice strain also produce similar changes. Thus, inferring structural differences from calcite FTIR spectra alone is not advisable. Instead, we advocate using FTIR grinding curves in conjunction with analyses of angle-dependent XRD peak widths using the Williamson-Hall relation. Thus, combining these two analysis techniques is more powerful and informative than using either one alone. These findings are relevant for heritage science, including archaeology.

4.2 Introduction

The origin of a material is of critical importance for archaeological interpretations, yet it is often challenging to determine. Calcite is especially difficult because it has many possible sources, including lime plaster (mortar), ash from fires [55], speleothems (flowstones, stalactites, stalagmites), pedogenic sources (calcrete), and mineralized tissue (shells, otoliths) [95]. This means that one must rely on subtle aspects of a material's structure, such as isotopic signatures, [96] trace elements, or heat-related changes to crystalline structure [23], to determine possible formation pathways. An increasing number of studies investigate how structural order differences might be extracted from the vibrational signatures of solids through their Fourier Transform Infrared (FTIR) spectra [22, 23, 38, 62, 65, 84, 97]. In archaeological samples, there is strong empirical evidence that FTIR analyses are useful for distinguishing between lime plaster, ash, limestone, and sparry calcite [22, 23]. However, the exact structural differences that cause changes in the FTIR spectra have not yet been reported.

FTIR spectroscopy is an effective, non-destructive technique to characterize the

composition of solid samples [11, 12, 80, 98]. It offers the advantages of small sample size and portability, including on-site use during archaeological excavations and in art galleries [95, 96, 99, 100]. However, quantitative analyses from FTIR data must be done carefully because peak intensities are strongly affected by sample preparation and measurement methods [22, 23, 101]. In this study, we show that three separate factors can contribute to FTIR peak intensities for calcite ($CaCO_3$) samples. From these comparisons, we offer recommendations for future analyses to use FTIR in tandem with X-ray diffraction (XRD) data. Our recommendations are particularly relevant for archaeological investigations in calcite-rich environments such as caves.

Several studies have used density functional theory (DFT) in conjunction with group theory analyses to verify the energies and intensities of the IR-active vibrational modes expected for carbonate units in calcite [1, 43]. Other studies have paired DFT calculations with experimental studies to investigate not only the mean vibrational energy for each mode (peak position), but also how IR peak widths can change when the calcite unit cell is distorted [22, 38]. These studies show that calcite's in-plane carbonate bend (ν_4 mode) is strongly affected by deformation, which is consistent with experimental investigations of amorphous calcium carbonate from biogenic sources [24, 38]. More recently, experimental studies of calcite showed that the same ν_4 peak is also the mode that softens (broadens) the most at high temperatures [62].

Although quantitative analyses of FTIR data are gaining popularity, XRD is still the benchmark method for assessing structural differences in solids. In powder XRD patterns, peak positions provide information about lattice strain: [17, 102]

$$\epsilon_{hkl} = \left(\frac{d - d_0}{d_0} \right)_{hkl}, \tag{4.1}$$

wherein ϵ_{hkl} is the average elastic strain for a given hkl direction based on the cal-

culated (d) and initial (d_0) plane spacings. XRD peak widths are affected by both crystalline domain size r as well as microstrain fluctuations σ: [103]

$$r = 2d\frac{\tan\,\theta_B}{W_L},\ \text{and} \tag{4.2}$$

$$\sigma = \frac{\sqrt{{W_G}^2 - {W_I}^2}}{4\sqrt{2\,\ln(2)}\,\tan\,\theta_B}. \tag{4.3}$$

Here, θ is the Bragg diffraction angle, and W_I is the instrumental broadening. XRD peaks can be fitted with a Voigt function to give the relative amount of Lorentzian contribution W_L and Gaussian contribution W_G. This strategy has been used successfully on high-resolution synchrotron XRD data from powders of biogenic and geogenic calcite [13, 104].

It is also possible to extract microstrain fluctuation information from lower resolution XRD data by assessing peak position shifts through the Williamson-Hall relation: [18, 33, 73, 105]

$$\text{FWHM}\,\cos\,\theta = \frac{K\lambda}{r} + 4\,\sigma\,\sin\,\theta \tag{4.4}$$

Here, r is the crystalline domain size, σ is the microstrain fluctuation, λ is the incident X-ray wavelength, and K is a dimensionless shape factor with a typical value of 0.9 for particles that are rough approximations to spherical. This expression shows a convenient correlation between the full width at half maximum (FWHM) of a given Bragg peak and the diffraction angle at which it occurs (2θ). This analysis is a standard option in XRD software such as Jade (Materials Data Inc), yet it is not often used in the literature.

In this paper, we demonstrate a clear link between lattice strain, microstrain fluctuations, and crystalline domain size (as obtained from Williamson-Hall analyses of powder XRD data) and relative FTIR peak intensities. We focus on two classes of

calcite that are each relevant for archaeological excavations: lime plaster, and calcitic speleothem flowstones. Our data uncover structural differences that are typical for each class. These case studies provide guidance for future investigations based on FTIR screening of calcite-containing samples.

4.3 Experimental details

Calcite lime plasters were made from purchased calcite (Merck) or naturally occurring chalk (Dead Sea, Israel) by heating to 800° for 6 hours and then cooling to room temperature. The product was then mixed with water and aged for various amounts of time (1-7 years) to produce plaster [23, 55]. One ancient lime plaster ($\sim$ 10,000 years before present from Yiftahel, Isreal) was also studied [106]. Additional comparisons were made by heating a 7-year plaster to 400°C, which is well below calcite's decomposition temperature. Calcite flowstones were obtained from Manot cave (Manot, Israel) during archaeological excavations led by the Israel Antiquities Authority in 2012 and 2013 [61]. Sample details are listed in Table 4.1.

Table 4.1: Crystalline domain size, microstrain fluctuations, and lattice constants calculated from XRD data. Domain size and microstrain fluctuations are calculated according to Equation 4.4. For narrow XRD peaks, domain sizes cannot be quantified accurately, so they are listed as "large." Lattice strains are listed for {100} and {001} planes based on Equation 4.1, using the lattice constants from JCPDS 88-1807 (calcite) as d_0. Sample P1 has larger uncertainty values because it contains $Ca(OH)_2$, and those peaks overlap with some calcite peaks.

Name	Description	r (nm)	σ (%)	a (Å)	c (Å)	ϵ_a (%)	ϵ_c (%)
P0	purchased powder	large	0.006±0.006	4.987±0.004	17.07±0.01	0.0(2)	0.0(5)
P1	plaster, 1 yr	90±40	0.03±0.04	5.0±0.1	17.0±0.3	0.2(4)	0.3(5)
P7	plaster, 7 yr	350±80	0.135±0.008	5.00±0.01	17.09±0.03	0.2(4)	0.1(6)
P7A	plaster, 7 yr annealed	240±40	0.113±0.008	4.98±0.01	17.05±0.02	-0.1(6)	-0.0(6)
P10K	plaster, 10,000 yr	250±30	0.006±0.006	4.983±0.005	17.05±0.01	-0.1(0)	-0.0(6)
F1	flowstone	large	0.039±0.003	5.00±0.01	17.08±0.01	0.2(4)	0.1(1)
F2	flowstone	large	0.059±0.005	4.98±0.01	17.04±0.02	-0.1(6)	-0.1(2)
F3	flowstone	large	0.141±0.007	4.982±0.006	17.03±0.01	-0.1(2)	-0.1(8)
F4	flowstone	large	0.161±0.006	4.98±0.01	17.02±0.02	-0.1(6)	-0.2(4)
F5	flowstone	large	0.146±0.008	4.98±0.01	17.02±0.02	-0.1(6)	-0.2(4)
F6	flowstone	large	0.164±0.007	4.98±0.01	17.02±0.02	-0.1(6)	-0.2(4)
F7	flowstone	large	0.195±0.006	4.97±0.01	16.98±0.03	-0.4(7)	-0.4(7)

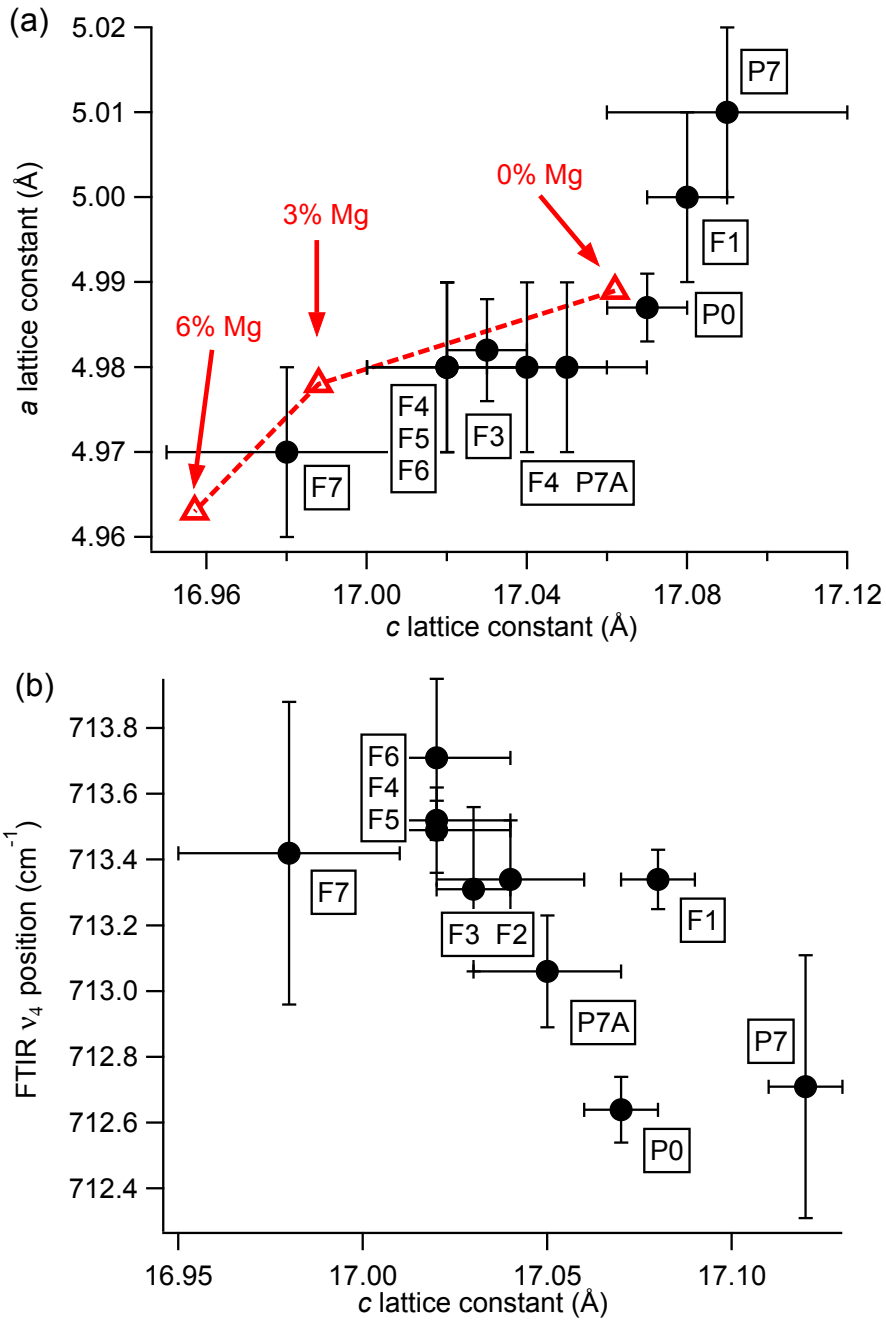

Figure 4.1: (a) Correlations between a and c lattice constants from XRD data (circles), compared with JCPDS standard patterns for zero- and low-Mg content calcite (triangles). Pure calcite ($CaCO_3$) is JCPDS 05-0586, $Mg_{0.03}Ca_{0.97}CO_3$ is JCPDS 97-008-6161, and $Mg_{0.06}Ca_{0.94}CO_3$ is JCPDS 89-1305. (b) Correlation between c lattice constants (from XRD data) and FTIR ν_4 peak position. Sample labels are defined in Table 4.1

The XRD data were collected using either a Rigaku Ultima III or Ultima IV system (each with Cu Kα radiation). All XRD data analyses were completed with the Jade software package (Materials Data Inc.) [9], including lattice constant refinements (Equation 4.1) as well as microstrain fluctuation assessments and crystalline domain size values (Equation 4.4). For reliable Williamson-Hall analyses (Equation 4.4), only XRD peaks with $2\theta \leq 70^\circ$ and that were well separated from other peaks were used. No peak deconvolutions were necessary.

FTIR spectra were obtained using either a Bruker Vertex 70v vacuum spectrometer or a Nicolet 380 N_2-purged spectrometer. All measurements were made in transmission mode over a wavenumber range of at least 4000 cm^{-1} to 500 cm^{-1} with a resolution of 1 cm^{-1}. Samples were ground with spectral grade KBr and then pressed (2 tons) into transparent 7 mm diameter pellets. IR peak positions and intensities were determined with Bruker's OPUS 7.0 software.

In general, the relative intensities of IR absorbance peaks are affected by the amount and distribution of sample particles in the KBr matrix. To compensate for these variations, and to decouple these effects from changes due to structural differences, we measured many FTIR spectra for each pellet after successive regrinding. Then, we normalized the calcite out-of-plane bend (ν_2) and in-plane bend (ν_4) peak intensities to the intensity of the asymmetric stretch (ν_3) within each spectrum. Results for each spectrum can then be compared to produce a "grinding curve" [23]. These grinding curves decouple the sample preparation influences from factors related to differences in the intrinsic structural order in the material. This procedure and its theoretical foundations are described in detail elsewhere [22].

4.4 Results

4.4.1 X-ray diffraction analyses

XRD data show that samples used in this study have calcite as the only crystalline phase. The one exception is the freshest plaster (1-year-aged), which contains some $Ca(OH)_2$ and aragonite. We compare the indexed raw XRD patterns in Supporting Information. Figure 4.1a shows the lattice constant values refined from these XRD data, compared with JCPDS standards [9]. Most flowstones have smaller lattice constants, which are consistent with low levels of Mg incorporation (<6%). Table 4.1 gives a summary of all lattice constants and the corresponding lattice strains (ϵ, from Equation 4.1).

All samples were assessed for angle-dependent XRD peak widths using the Williamson-Hall relation (Equation 4.4). Two representative examples are shown graphically in Figure 4.2. The first important feature in this plot is the slope of the fits, which are directly proportional to microstrain fluctuation values. For data in Figure 4.2, this means that the microstrain fluctuation value in sample F4 (a flowstone) is much larger than for sample P0 (a purchased fine-grain calcite). The second important feature of the Williamson-Hall plots are the y-intercepts of the fit lines, which are inversely proportional to crystalline domain size. Larger domain sizes cause narrower XRD peaks. For data in Figure 4.2, both samples have y-intercepts close to zero, which indicates large crystalline domain sizes. In such cases, the peak widths are dominated by other factors, such as instrumental broadening from the diffractometer. Table 4.1 lists calculated crystalline domain sizes (r) and microstrain fluctuation values (σ) for all samples. We note that the range of these microstrain fluctuation values are comparable to those reported earlier for biogenic calcite [13].

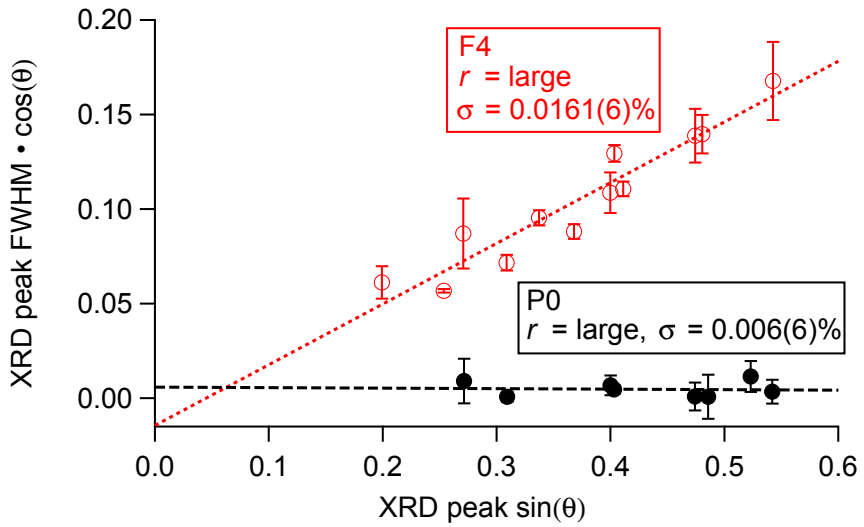

Figure 4.2: Representative plots showing angle-dependent XRD peak widths, according to the Williamson-Hall relation. The slopes of the fit lines are directly proportional to microstrain fluctuation values, and the y-intercepts are inversely proportional to crystalline domain sizes.

4.4.2 Fourier transform infrared spectra

FTIR spectra indicate sample compositions that are consistent with XRD data. Peaks due to carbonate vibrational modes are present in all spectra: ν_3 (asymmetric stretching near 1430 cm^{-1}), ν_2 (out-of-plane bending near 875 cm^{-1}), and ν_4 (in-plane bending near 713 cm^{-1}). Two additional peaks are related to combined modes [1, 11, 12]: $\nu_1 + \nu_4$ at 1799 cm^{-1}, and $\nu_1 + \nu_3$ at 2512 cm^{-1}. Only the freshest plaster (P1) shows some $Ca(OH)_2$ (3643 cm^{-1}) and aragonite (858 cm^{-1}). No evidence of other phases, such as amorphous calcium carbonate, was detected in any sample. A more detailed comparison of the raw FTIR data is included in Supporting Information.

Like the XRD data, FTIR spectra also provide evidence of Mg incorporation. The ν_4 peak positions in some samples show slight blue shifts ($\leq$ 2 cm^{-1}), as displayed in

Figure 4.1b. These shifts correlate well with lattice constant contractions (Table 4.1), both of which are consistent with low levels of Mg incorporation [107, 108].

Relative FTIR peak height comparisons among selected samples are shown in Figure 4.3. Each set of data points corresponds to a range of different preparation conditions (grindings) for a single type of sample (see Section 4.3 above). In general, higher normalized ν_4 values indicate better crystallinity [38]. Figure 4.3a shows that small crystalline domain sizes (90(40) nm) correlate with a grinding curve shift to lower normalized ν_4 values, when lattice strain and microstrain fluctuations are both zero. We note that these grinding curve shifts are quantitatively similiar to earlier reports that compared large-grain spar calcite and lime plaster (though no crystalline domain sizes were reported) [22, 23].

To emphasize that grinding curve shifts cannot be due solely to crystalline domain size differences, Figure 4.3b shows that large microstrain fluctuation values (0.113(8)%) also correlate with a grinding curve shift to lower normalized ν_4 values (when lattice strain is zero and crystalline domain sizes are large). Figure 4.3b shows that annealing a sample to reduce microstrain fluctuations drives the grinding curve to higher ν_4/ν_3 values for a given ν_2/ν_3 range, even when the overall crystalline domain sizes remain comparable. In the case shown in Figure 4.3b, the crystalline domain sizes for a 7-year plaster shrink only slightly upon annealing (from 350±80 nm to 240±40 nm after 6 hours at 400°C), but the microstrain fluctuations drop from 0.135(8)% to 0.113(8)% after annealing.

Thus, two different kinds of structural disorder (small crystalline domain sizes, and large microstrain fluctuations) are correlated with the same kind of grinding curve shifts. Finally, Figure 4.3c shows that two samples with different kinds of structural disorder can have identical grinding curve shifts. A comparison of FTIR grinding curves for all samples is included in Supporting Information.

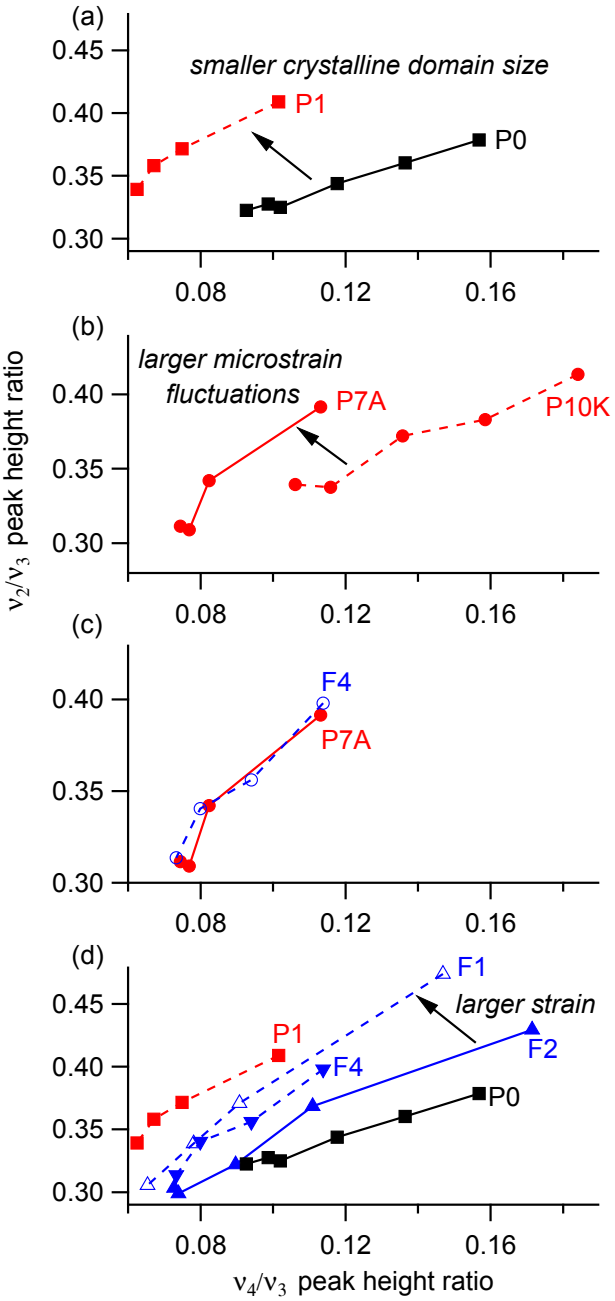

Figure 4.3: Representative FTIR grinding curves highlight differences among calcite samples with two distinct kinds of structural disorder. (a) compares large and small crystalline domain sizes, while (b) compares low and high microstrain fluctuation values. (c) shows that two samples with different kinds of structural disorder can have identical grinding curve shifts. (d) compares large and small lattice strain values. These comparisons emphasize that grinding curve shifts cannot be uniquely correlated to a single kind of structural disorder.

4.5 Discussion

Based on data in Table 4.1 and in Figure 4.3, it is evident that three different kinds of structural disorder (σ, ϵ, and r) can affect the relative peak intensities in calcite FTIR spectra. Furthermore, our results show that decoupling these three different kinds of structural disorder is not possible from FTIR grinding curves alone.

It is a new finding that microstrain fluctuations affect grinding curve shifts in a way that is similar to the effect of small crystalline domain sizes. Prior studies compared FTIR spectra, XRD data, and DFT for different sources of crystalline calcite, but no explicit suggestions for the underlying structural differences were proposed [22]. More recent studies of aragonite suggested that microstrain fluctuations could influence FTIR peak widths, but no verification was attempted [79].

Our work also shows that lattice strain, either compression or expansion, can affect grinding curve shifts. This result has support from other studies in the literature, but had not been demonstrated explicitly. An earlier report used high-resolution neutron diffraction data to assess structural differences in biogenic calcites, including comparisons with FTIR ν_4 peak positions and widths [108]. Their work used energy-dispersive and wavelength-dispersive X-ray analyses to determine Mg content independently from the lattice constants derived from the diffraction measurements. They used these data to correct for Mg content in their FTIR data, and concluded that all peak position differences can be attributed to Mg levels. In our study, this is consistent with the correlation we see between XRD lattice constants and FTIR ν_4 peak positions, as presented in Figure 4.1.

However, this earlier neutron-diffraction study also found that FTIR peak width differences are not directly correlated with Mg levels [108]. Instead, they found a stronger correlation between FTIR widths and the magnitude of lattice constant changes. They observed lattice contractions in some samples (suggested to be related to Mg incor-

poration), but reported lattice expansions in other samples (suggested to be related to the presence of an amorphous precursor).

In our study, we also find a correlation between lattice constant changes and FTIR peak attributes. Here, we use grinding curve shifts (normalized FTIR peak height changes) as a proxy for FTIR peak width differences [22]. Since we have evidence that microstrain fluctuations affect grinding curve shifts, isolating the effect of lattice strain requires more careful comparisons. We provide one such example in Figure 4.3d among flowstones that all have large crystalline domain sizes. This Figure compares the grinding curve for a flowstone with an expanded lattice and low microstrain fluctuations (F1) with two flowstones (F2 and F4) that have zero lattice expansion but higher microstrain fluctuation values. Based on microstrain fluctuation differences alone, one would expect that F1 should have the smallest grinding curve shift. Instead, F1 has a larger shift than F2 or F4, and we attribute this to its larger lattice strain. We provide a comparison of microstrain fluctuation values with lattice strain in Supporting Information.

4.6 Conclusions

There is potential for wider societal impact whenever an analysis tool can be used to understand more about the conditions under which a heritage material was likely produced, or altered. This is certainly true for the work we present here, since decoding the formation and diagenesis history of calcite-based materials – including geogenic, biogenic, and anthropogenic sources – plays a critical role in archaeological interpretations and in heritage restoration efforts. Furthermore, the analyses we describe here could likely be helpful to identify structural differences in other minerals. For example, aragonite [79] and hydroxyapatite [84] have each shown shifts in

their grinding curves, but as of yet, no correlations between these grinding curves and Williamson-Hall analyses of XRD data have been reported.

Our results demonstrate that crystalline domain size, microstrain fluctuations, and lattice strain each affect the FTIR spectra of calcite. We emphasize that the methods described here can identify the effects of structural disorder, but not the causes of structural disorder. This distinction is important. Several common kinds of structural irregularities can change calcite's FTIR spectrum in similar ways. This underscores the need to pair FTIR spectroscopy with another method (such as XRD) if one wants to determine what kind of structural disorder is present in the calcite. It is true that many different factors during the synthesis and processing of calcite could cause strains, microstrain fluctuations or other structural irregularities. It is also true that these structural irregularities could be correlated with features such as porosity, crystallite size, or morphology. In the present study, we did not undertake an extensive synthesis-based project to try to produce a full range of different structural defects that calcite can accommodate. Instead, we used sample types that would be relevant for the archaeologists and geoscientists who might be the most likely ones to adopt our method. In this context, it is important to comment on how effective FTIR can be as an on-site identification tool for archaeology.

The present work demonstrates that some kinds of archaeological sites, including caves, may be very challenging for using FTIR grinding curve analyses. Most published reports of grinding curve comparisons have focused on open-air sites, or utilized samples made in laboratory settings [22,23,79,84,106]. The flowstones analyzed in the present study were obtained from recent excavations in Manot Cave (Israel). During these excavations, grinding curves were used in an attempt to identify calcitic ash, which is known to have a pronounced grinding curve shift [23]. Flowstone fragments were prevalent in virtually all sediments. As we demonstrate in this work, flowstones

can have very different grinding curve shifts, so it is challenging to distinguish ash signatures from the background calcite. Therefore, it was more helpful to use techniques such as optical microscopy and polarized light microscopy to give additional information (on-site) to help distinguish between ash and flowstones [95]. We note that the heterogeneous chemical composition of ash prevents a thorough investigation of the lattice strain and microstrain fluctuation values in this source of calcite.

Even though this work shows that it is helpful to support FTIR measurements with XRD data, the reality is that many archaeological samples are too small in volume, or too precious, to obtain the powder XRD data required for more detailed structural information. For such samples, the best option is to compare with grinding curves for common sources of calcite, including samples with high degrees of structural perfection. This procedure provides a baseline for comparing relative degrees of structure differences, even if the exact type of disorder cannot be identified from the FTIR data alone. In this way, the grinding curves can be an effective means of rapid on-site screening for samples of possible interest, even if the detailed analyses would benefit from more extensive off-site analyses.

4.7 Acknowledgments

We used XRD facilities at Memorial University (Dr. Wanda Aylward, CREAIT) and at the Weizmann Institute (Dr. Isai Feldman). We thank Dr. Miryam Bar-Matthews and Dr. Avner Ayalon (Geological Survey of Israel) for access to flowstone samples F3, F5, F6, and F7. We also thank Dr. Omry Barzilai (Israel Antiquities Authority) with Prof. Israel Hershkovitz (Tel Aviv University) and Dr. Ofer Marder (Ben Gurion University) who led the excavations at Manot Cave. We thank Dr. Ianir Milevski and Dr. Hamudi Khalaily (Israel Antiquities Authority) who led the excavations at

Yiftahel.

4.8 Supporting Information

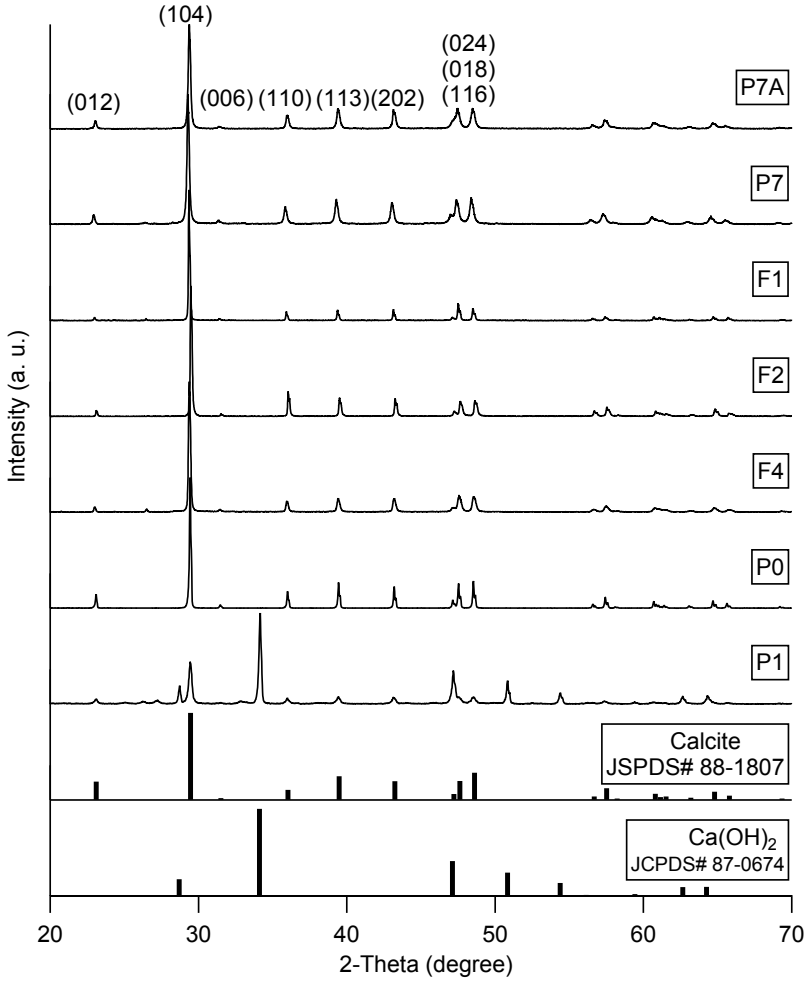

Plaster

Figure 4.4: Representative XRD diffraction data for different calcite samples, and JCPDS standards for calcite (88-1807) and $Ca(OH)_2$ (87-0674) [9]. P1 is the only sample that shows $Ca(OH)_2$. Weak peaks in S1 near 27° and 32° indicate the existence of aragonite, which is consistent with FTIR data.

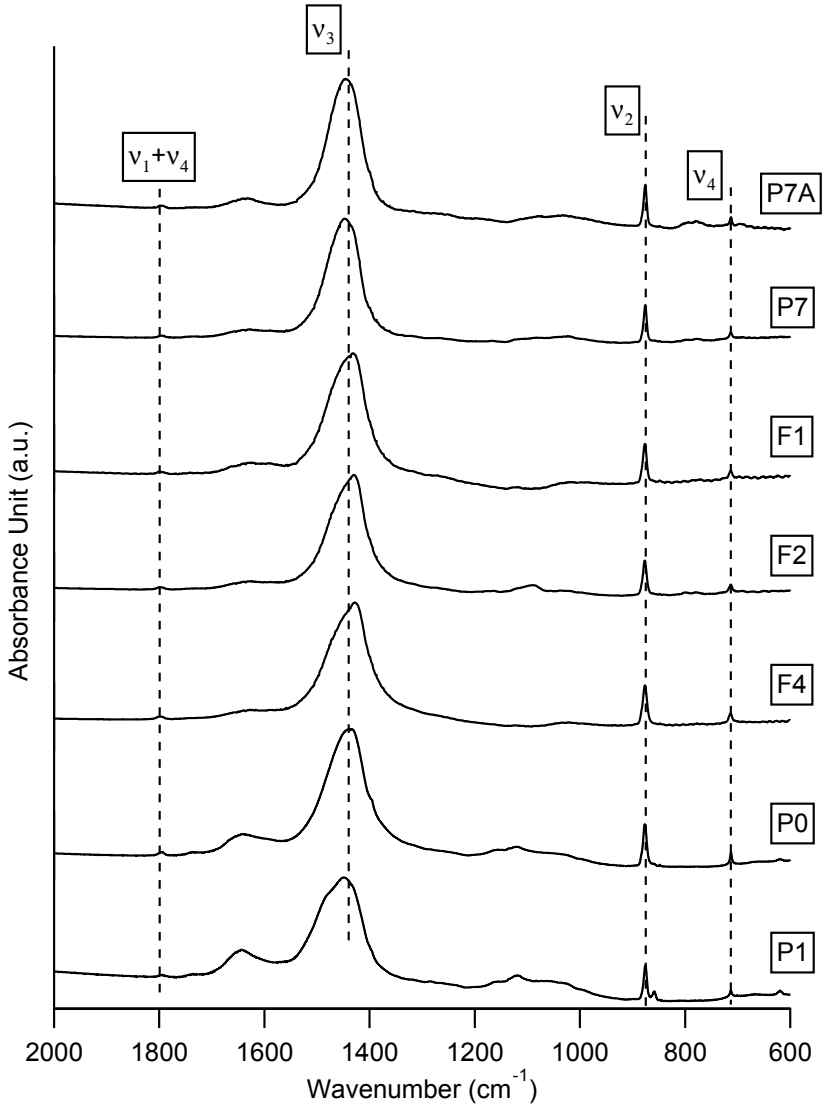

Figure 4.5: Representative FTIR spectra compared using absorbance values that are scaled to the largest (ν_3) peak. Normal mode assignments for each peak are made based on literature reports [1, 11, 12]. The broad peak near 1650 cm^{-1} is from water adsorbed by the KBr matrix during sample preparation.

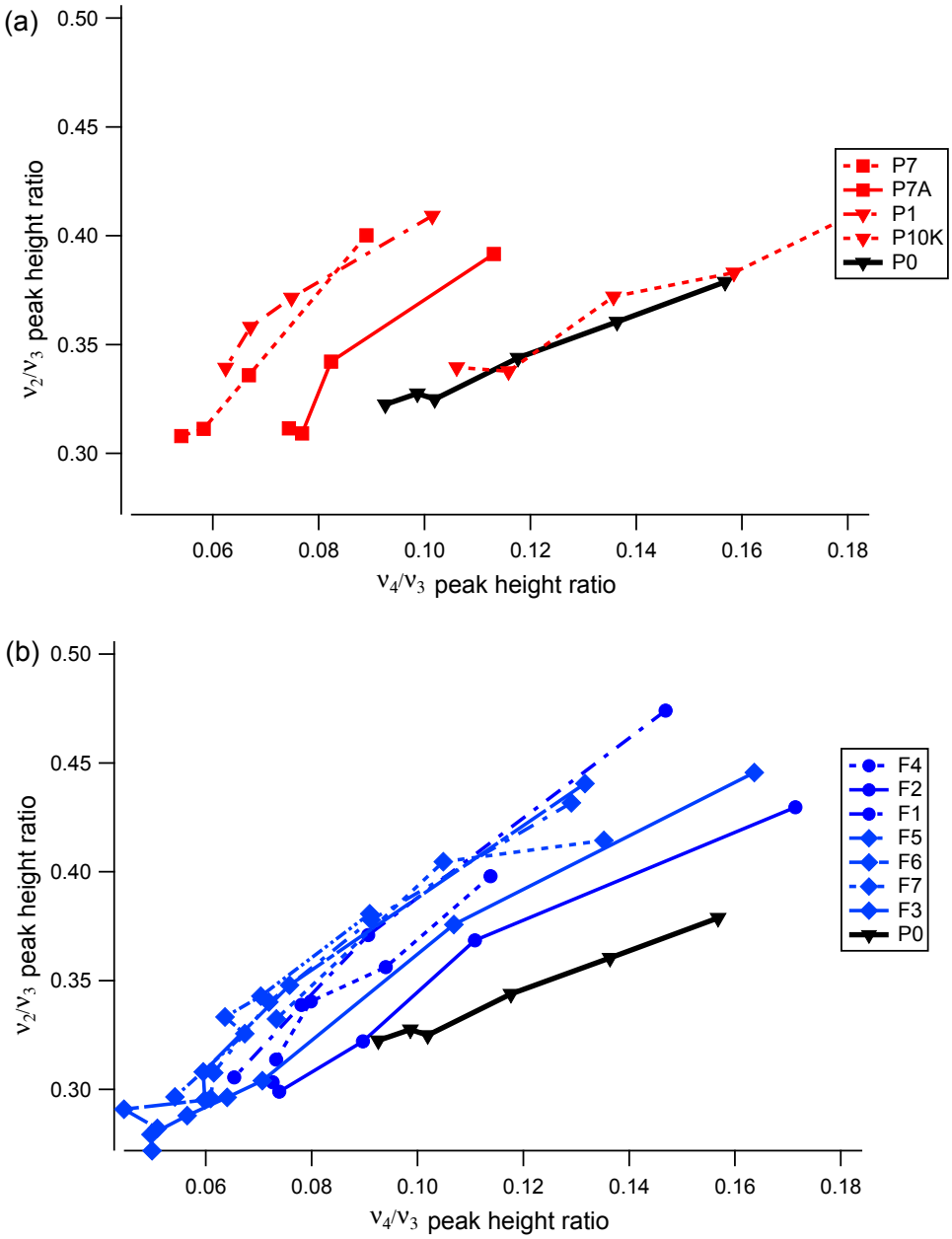

Figure 4.6: Grinding curves for all samples. Sample labels are defined in Table 4.1 in the main text. Color coding differentiates plaster samples (red in (a): P1, P7, P7A, P10K) and flowstone samples (blue in (b): F1-F7) from purchased (synthetic) calcite (black: P0).

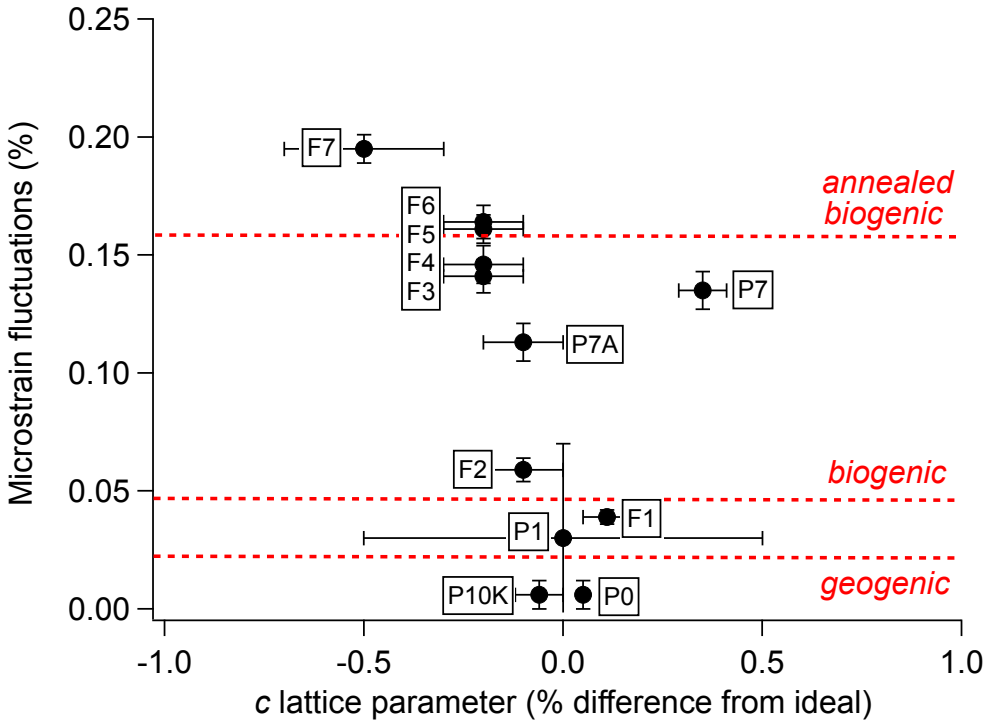

Figure 4.7: Comparison of microstrain fluctuation values with c lattice constants. Sample labels are defined in Table 4.1 in the main text. Microstrain fluctuation values can show considerable variation among different samples even when there are no statistically significant differences in their unit cell sizes. The dotted lines indicate approximate microstrain fluctuation values that have been reported for calcite in an earlier report by Pokroy *et al.* [13]

Chapter 5

XAFS measurements on calcite minerals

This chapter is a manuscript in preparation. The authors are Ben Xu, Michael B. Toffolo, Elisabetta Boaretto, and Kristin M. Poduska.

5.1 Abstract

By performing XAFS (X-ray absorption fine structure) measurements, the differences in plaster samples due to their preparation conditions were studied. Their X-ray diffraction (XRD) patterns, Fourier transform infrared (FTIR) spectra, and X-ray absorption near-edge structure (XANES) spectra are similar; however, the R-factor of extended X-ray absorption fine structure (EXAFS) fitting show clear differences, and the differences are strongly dependent on the $Ca(OH)_2$ phase.

5.2 Introduction

Calcium carbonation in natural minerals has been studied by many methods, including XAFS, XRD, and FTIR [24, 35, 55, 109]. Due to differences in formation conditions, calcium carbonate has three polymorphs, which are calcite, aragonite, and vaterite [52, 110]. Studying the structure and phase differences in natural calcium carbonate can give valuable information not only for material studies, but also for geological, biological, and archaeological research.

XAFS is a powerful technique for investigating material structure. It can give detailed information about the short-range structure of a sample regardless its crystallinity. It is widely used for studying amorphous phases, such as amorphous calcium carbonate (ACC) in biogenic minerals. Studies on biogenic ACC indicate that the structures of different origins of ACC vary considerably, and crystallization pathways strongly depend on the local structure of the ACC [24, 35, 109].

In this work, we studied samples with mixed phases by XAFS. By measuring the XAFS spectra of pyrogenic plaster samples (which are a mixture of calcite and $Ca(OH)_2$), as well as crystalline calcite and pyrogenic lime samples, the differences in plaster samples were investigated. By correlating the differences with preparation condition, we suggest the conversion to calcite in a plaster sample is strongly dependent on its preparation temperature. Moreover, the capability of XAFS measurements for studying mixtures is also demonstrated.

5.3 Experimental details

Methods for preparation can be described by following chemical reactions:

$$CaCO_3 \overset{800\ or\ 900^\circ C}{\longrightarrow} CaO\ (\text{lime}) + CO_2$$

$$2\ CaO + H_2O \longrightarrow Ca(OH)_2$$

Table 5.1: Samples used in this chapter are listed. The heating temperature and raw starting materials for preparing lime and plaster samples are included.

standards	raw material	
C1	analytical-grade calcite (Merck)	
C2	spar calcite	
PA	ancient plaster (Yiftahel)	
A1	spar aragonite	
A2	glycymeris shell (aragonite)	
plaster		temperature
P1	analytical-grade calcite (Merck)	800°C
P2	analytical-grade calcite (Merck)	900°C
P3	spar calcite	800°C
P4	spar calcite	900°C
P5	spar aragonite	800°C
P6	spar aragonite	900°C
P7	glycymeris shell	800°C
P8	glycymeris shell	900°C
lime		temperature
L1	analytical-grade calcite (Merck)	900°C
L2	spar calcite	900°C
L3	spar aragonite	900°C
L4	glycymeris shell	900°C

$$Ca(OH)_2{+}CO_2 \longrightarrow CaCO_3{+}H_2O \text{ (plaster)}$$

As described in Ref. [55], calcium carbonate is decomposed by heating (above 800°C) for 12 hours. Quick lime powders were collected from the production (CaO) after the heating process. A portion of the production was placed in a beaker and mixed with deionized water in order to form a thin plaster layer. Both the quick lime powder and plaster layers were left to cure under ambient laboratory conditions. Therefore, the lime samples in this chapter are not pure CaO. $Ca(OH)_2$ formed in them during storage. For all lime samples, the heating temperature was 900°C. For plaster samples, two possible temperatures (800°C and 900°C) were used. The details for each sample are listed in Table 5.1.

Analytical-grade calcite was bought from Merck. Calcite spar is a pure single crystal of geogenic calcite and was from Mexico. Ancient plaster was collected from

the historical site of Yiftahel (Israel), and previous studies suggested that ancient plaster is composed of well-crystallized calcite [22, 23]. Aragonite spar is a pure single crystal of geogenic aragonite and was from Spain, and glycymeris shell (aragonite) was from a beach near Ashkelon, Israel.

XAFS measurements were accomplished using the Soft X-ray Micro-characterization Beamline 06B1-1 (SXRMB) at the Canadian Light Source (CLSI). A small quantity of powdered sample was mounted on black carbon tape which was attached to a copper plate. Samples were then exposed to synchrotron X-rays. This ejected ionized electrons from the Ca K-edge, which were detected and are shown here as XAFS spectra. XAFS data were analyzed using the IFEFFIT software package [78]. Fourier transformation of EXAFS spectra in R space are from 2 $Å^{-1}$ to 9 $Å^{-1}$. Artemis software was employed to calculate the coordination number, the neighbor distances, and the deviation in distance (σ^2) based on an ideal calcite structure [2]. The fitting range of the R region is from 1 Å to 4 Å for the first four coordination shells. R-factors, known as fitting residual, were used to describe the differences between fitted and experimental spectra.

5.4 Results

5.4.1 Preliminary sample characterization

Composition of our samples were examined by X-ray diffraction and FTIR measurements prior to the XAFS measurements. XRD patterns for plaster and lime samples are presented in Figure 5.1. Powder XRD patterns were compared to JCPDS standards of 86-2334 (calcite), 76-0606 (aragonite), 87-0673 ($Ca(OH)_2$), and 82-1691 (CaO) [9]. The aragonite and two calcite samples (A1, C1, and C2) show clear single phase of XRD patterns. XRD patterns of the ancient plaster sample (PA) indicate

that it is composed of well crystallized calcite, although a minor peak at 27° implies that it also contains a small amount of other minerals. Lime samples are composed of CaO and $Ca(OH)_2$, and no extra peaks were present. Plaster samples have similar patterns-they all contain calcite and a large portion of $Ca(OH)_2$. XRD patterns for all plaster samples also show weak peaks which are related to aragonite due to the formation of small amounts of aragonite during the reactions [55].

FTIR measurements gave further details on composition of samples. Spectra are shown in Figure 5.2. The three characteristic peaks (ν_2, ν_3, and ν_4) of calcite are present in all samples, indicating that they all contain calcite. However, they only show weak calcite peaks, indicating calcite is the minor component, which is the reason why XRD patterns for lime samples do not show calcite features. The strong peak at 3643 cm^{-1} in spectra of both lime and plaster is due to the OH- stretching of $Ca(OH)_2$. The OH- stretching intensity (normalized to ν_3) significantly decreases in plaster compared to lime, which implies that $Ca(OH)_2$ converts to $CaCO_3$. The weak peak at 855 cm^{-1} in the plaster spectrum is due to aragonite, which corresponds to XRD results. Spectrum of the ancient plaster is the same as the spectra of two calcite samples (C1 and C2), indicating the ancient plaster are mainly composed of calcite, which corresponds to its XRD patterns. The small amount of minerals in it caused the broad peak between the ν_3 and ν_2 peaks.

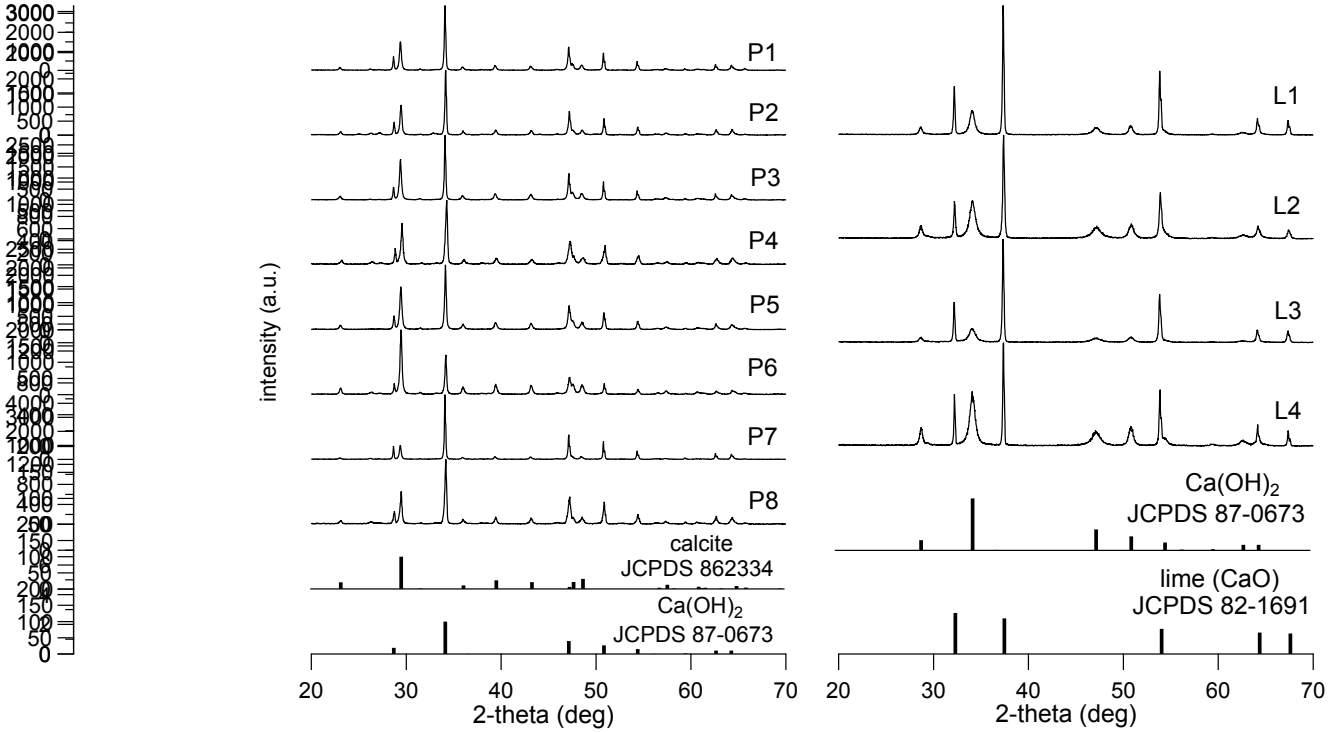

Figure 5.1: Powder XRD patterns of plaster samples (left) and lime samples (right) are presented. Patterns are offset and scaled along the vertical (intensity) axis for easier comparison. Data are compared to JCPDS standards for calcite, calcium hydroxide, and lime [9].

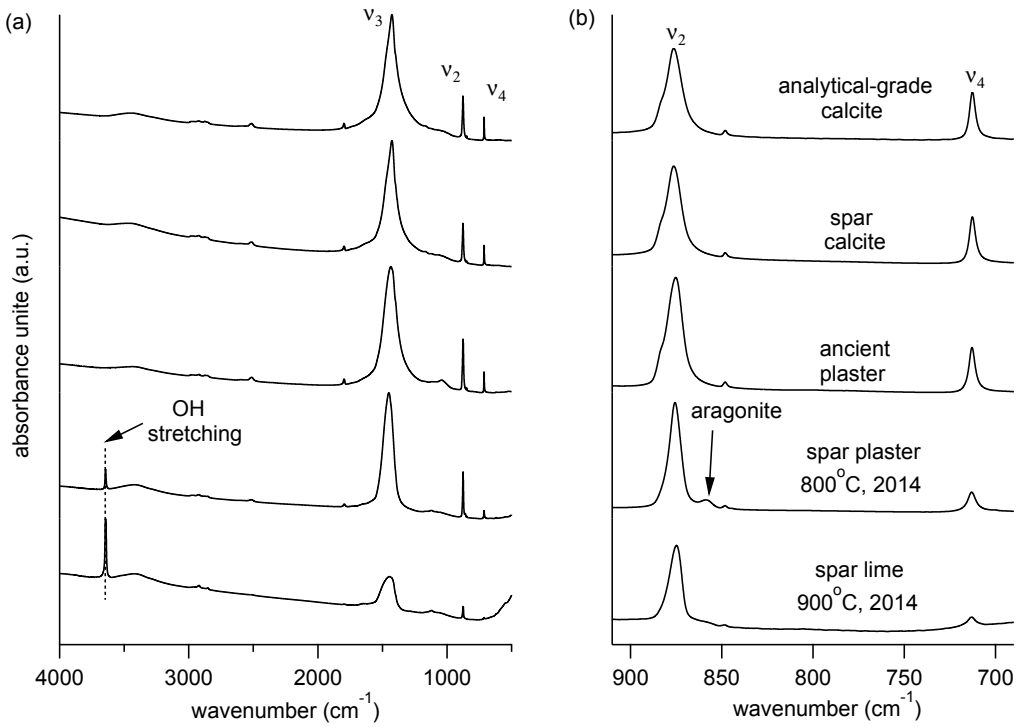

Figure 5.2: FTIR spectra in the full range from 4000 cm^{-1} to 500 cm^{-1} are shown in (a) and the a zoom is shown in (b). The ν_3, ν_2, and ν_4 peaks are dominant. The OH- stretching mode for modern plaster and lime indicates the presence of $Ca(OH)_2$, which is consistent with XRD results.

5.4.2 Pre-edge and XANES regions

The pre-edge and XANES region of XAFS spectra of lime (L2), plaster (P3), calcite (C2), and aragonite (A2) samples are shown in Figure 5.3. The energy of the K-edge for calcium is at 4038 eV. The pre-edge peak (A) at 4040 eV and the shoulder (B) at 4045 eV are attributed to the *1s-3d* and *1s-4s* transitions in a calcium atom [24, 35]. Two main XANES peaks, C at 4048 eV and D at 4061 eV, are characteristic of calcite. C2 and PA show identical and characteristic XANES spectra for calcite. Spectrum

L2 (lime) does not show any calcite features in the XANES regions. This agrees with its XRD pattern. The sharp peak at 4051 eV (near peak C) is due to $Ca(OH)_2$ and CaO [111]. Spectrum P3 shows mixing features of calcite and lime, indicating that plaster is an intermediate state between lime and calcite.

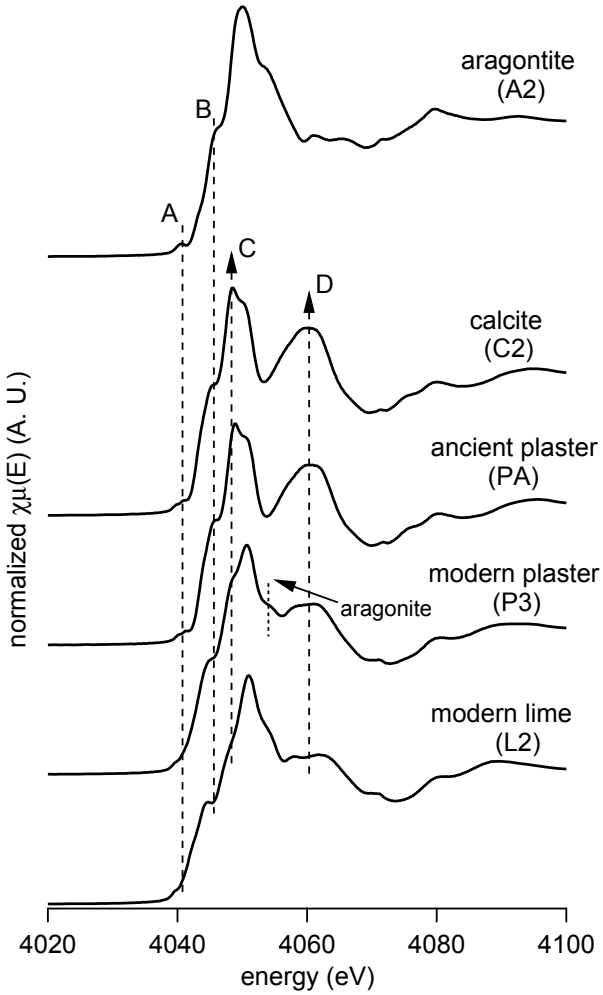

Figure 5.3: XAFS spectra (Ca K-edge) for calcite (C2), ancient plaster (PA), plaster (P3), lime (L2), and aragonite (A2). The pre-edge absorption (peak A) and the shoulder (peak B) denote the *1s-3d* and *1s-4s* transitions in a calcium atom. The two XANES peaks (C and D) are characteristic to calcite. The growth of the C and D peaks from lime to calcite is indicated with arrows. Modern plaster sample also contains little amounts of aragonite.

Table 5.2: The four closest neighbours around a Ca site in calcite, based on Markgraf's results [2].

bond	distances
Ca-O	2.36 Å
Ca-C	3.21 Å
Ca-O	3.46 Å
Ca-Ca	4.05 Å

5.4.3 EXAFS regions

Fourier transforms of EXAFS spectra in R space are presented in Figure 5.4. Spectra of calcite standards show typical calcite coordination shells. The bonding distances in the first four coordination shells for calcium in calcite are shown in Table 5.2, based on Ref. [2]. The first (1.8 Å) and second (3.5 Å) strongest peaks are attributed to Ca-O and Ca-Ca bonds. The two weak peaks (2.4 Å and 2.8 Å) in between are due to Ca-C and Ca-O bonds. It is noteworthy that positions of peaks are not the real bonding distances due to the phase correction during Fourier transforms [76]. However, their relative positions can be trusted.

Quantitative analysis of EXAFS spectra requires specialized software (Artemis) [78]. Theoretical model data for the fitting procedure were built based on the crystallographic data of ideal calcite [2], and the computer code of FEFF8 was employed [78]. The first four coordination shells (Ca-O_1, Ca-C, Ca-O_2, and Ca-Ca) are included (See Table 5.2). Coordination numbers were fixed for all shells. The variable parameters during fitting were bond distance (r), the variance in the half scattering path length (σ^2(Å^2)), and amplitude. The results are shown in Table 5.3 and Table 5.4. Bonding distances are the same for all samples within uncertainties. However, R-factors (residual factor), which indicate the stability of fitting, are different. Plaster samples prepared at a lower temperature have considerably larger R-factors.

Fourier transforms of EXAFS spectra in R space are presented in Figure 5.4.

Spectra of calcite standards show typical calcite coordination shells. The bonding distances in the first four coordination shells for calcium in calcite are shown in Table 5.2, based on Ref. [2]. The first (1.8 Å) and second (3.5 Å) strongest peaks are attributed to Ca-O and Ca-Ca bonds. The two weak peaks (2.4 Å and 2.8 Å) in between are due to Ca-C and Ca-O bonds. We note that the positions of peaks are not the real bonding distances due to the phase correction during Fourier transforms [76]. However, their relative positions can be trusted.

The differences in the spectra of plaster samples are mainly attributed to heating temperatures rather than raw materials, which agrees with the results discussed in Ref. [55]. Plaster samples prepared at a lower temperature show more $Ca(OH)_2$ features.

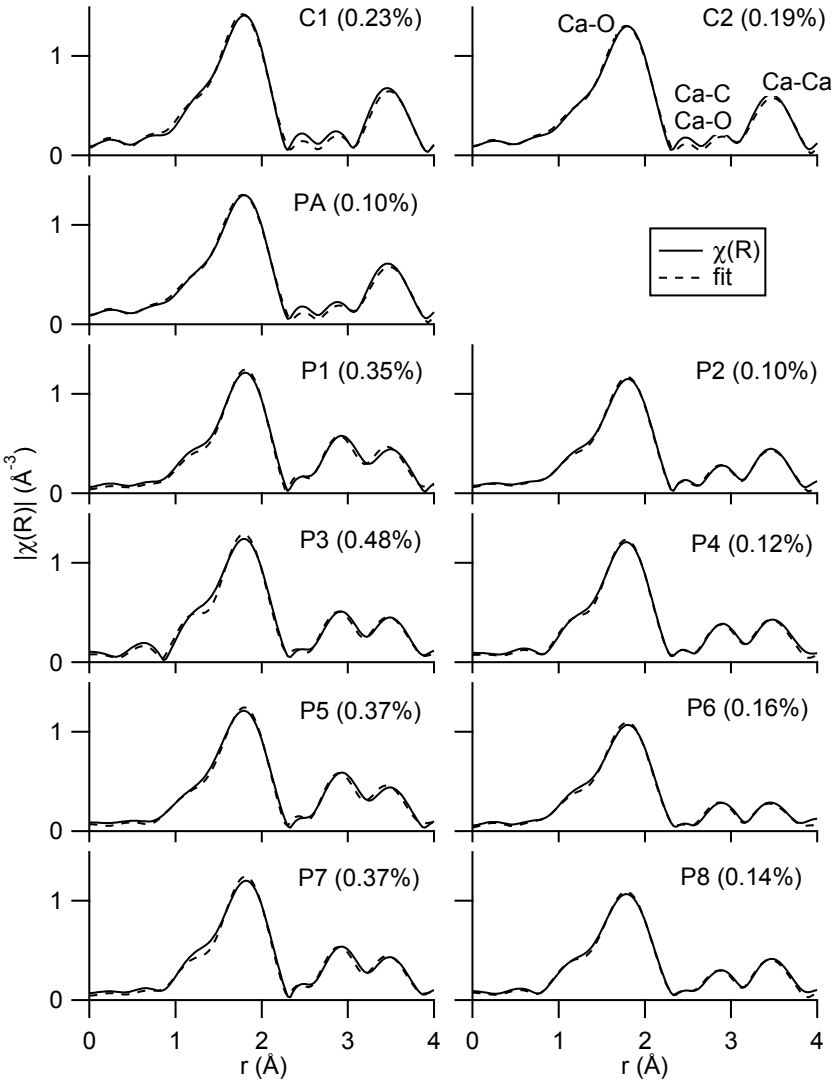

Figure 5.4: Fourier transformed EXAFS spectra in R space for calcite and plaster samples. Dashed lines indicate fitted results based on ideal calcite. Four shells are included during fitting. R-factors for plasters prepared at 800°C are considerably larger than those prepared at 900°C, which is related to their larger amount of secondary phases.

Table 5.3: Fitted results of EXAFS spectra for pure calcite samples, including bonding distances in the first four coordination shells, Debye-Waller factor (σ^2), and R-factor, (the stability of a fit).

sample	bond	r(Å)	σ^2(Å^2)	R-factor
C1	Ca-O	2.37±0.02	0.009±0.003	0.23%
	Ca-C	3.41±0.08	0.02±0.02	
	Ca-O	3.59±0.05	0.010±0.008	
	Ca-Ca	4.04±0.02	0.010±0.003	
C2	Ca-O	2.38±0.01	0.010±0.002	0.19%
	Ca-C	3.45±0.08	0.03±0.02	
	Ca-O	3.63±0.05	0.013±0.009	
	Ca-Ca	4.05±0.02	0.011±0.003	
PA	Ca-O	2.378±0.008	0.010±0.002	0.10%
	Ca-C	3.46±0.07	0.03±0.02	
	Ca-O	3.63±0.04	0.016±0.008	
	Ca-Ca	4.05±0.02	0.011±0.002	

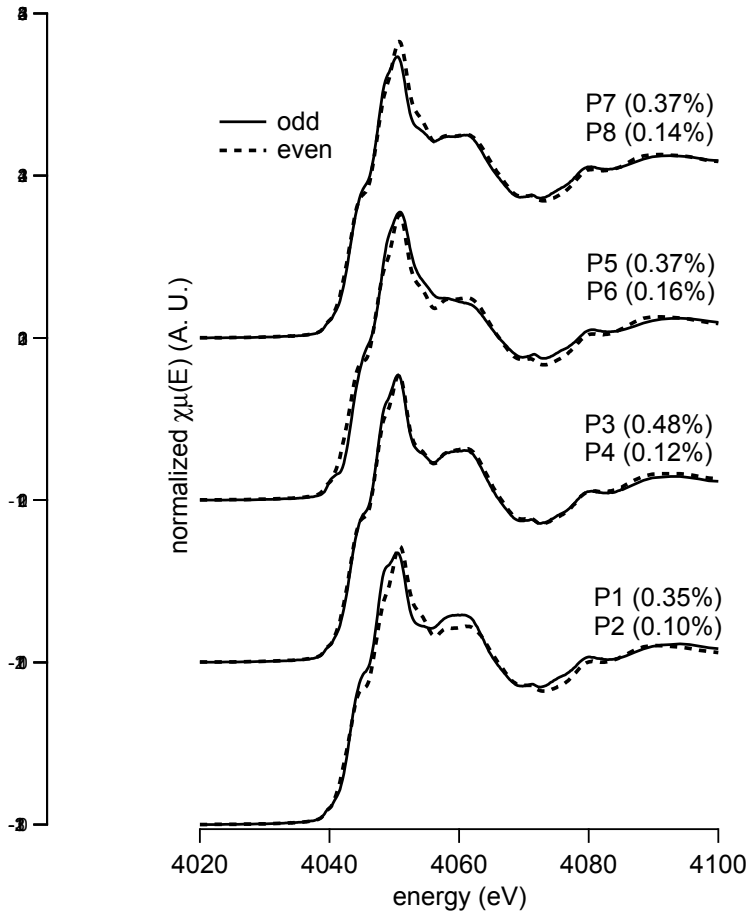

Figure 5.5: Normalized XAFS spectra for plaster samples. By eye, there are no clear differences among plasters prepared at different temperatures. However, a large R-factor correlates well with samples that have a larger amount of secondary phases.

Table 5.4: Fitted results of EXAFS spectra for all plaster samples. Although bonding distances are the same within uncertainties for all samples, their R-factors vary.

smaple	bond	r(Å)	σ^2(Å^2)	R-factor
P1	Ca-O	2.38±0.01	0.006±0.003	0.35%
	Ca-C	3.36±0.08	0.03±0.02	
	Ca-O	3.48±0.02	0.016±0.003	
	Ca-Ca	4.06±0.03	0.011±0.005	
P2	Ca-O	2.379±0.007	0.008±0.001	0.10%
	Ca-C	3.33±0.05	0.03±0.01	
	Ca-O	3.50±0.01	0.007±0.002	
	Ca-Ca	4.04±0.01	0.014±0.002	
P3	Ca-O	2.38±0.02	0.008±0.003	0.48%
	Ca-C	3.32±0.08	0.03±0.02	
	Ca-O	3.49±0.02	0.002±0.003	
	Ca-Ca	4.06±0.03	0.017±0.006	
P4	Ca-O	2.37±0.008	0.009±0.002	0.12%
	Ca-C	3.32±0.04	0.03±0.01	
	Ca-O	3.49±0.01	0.005±0.002	
	Ca-Ca	4.05±0.02	0.016±0.002	
P5	Ca-O	2.39±0.01	0.007±0.002	0.37%
	Ca-C	3.34±0.08	0.03±0.02	
	Ca-O	3.48±0.02	0.000±0.03	
	Ca-Ca	4.06±0.03	0.016±0.005	
P6	Ca-O	2.38±0.009	0.009±0.002	0.16%
	Ca-C	3.26±0.05	0.03±0.01	
	Ca-O	3.48±0.02	0.006±0.003	
	Ca-Ca	4.02±0.03	0.023±0.005	
P7	Ca-O	2.39±0.01	0.007±0.003	0.37%
	Ca-C	3.34±0.08	0.03±0.02	
	Ca-O	3.49±0.02	0.001±0.003	
	Ca-Ca	4.06±0.03	0.016±0.005	
P8	Ca-O	2.39±0.008	0.010±0.002	0.14%
	Ca-C	3.34±0.05	0.03±0.01	
	Ca-O	3.49±0.01	0.006±0.002	
	Ca-Ca	4.06±0.02	0.016±0.003	

5.5 Discussion

Much research has investigated crystallization processes in geogenic, biogenic, and lab-produced ACC phases using XAFS measurements [24, 35, 109]. By analyzing the coordination number or the stability of an EXAFS fit [24, 35, 109], structural differences and the subsequent crystallization of ACC were studied. Here, we demonstrate that XAFS measurements are also a useful method to study the carbonation process in $Ca(OH)_2$ during plaster formation.

In 2002, Levi-Kalisman *et al.* studied three stable biogenic amorphous calcium carbonates (ACC) using XAFS [109]. They found that an EXAFS fit for one sample was not stable (by comparing the reduced χ^2), and they attributed this instability to its more heterogeneous internal structure. In our case, R-factors (fitting residual) is used to evaluate the differences between fitted and experimental spectra. Due to that calcite crystallographic data was used for the fitting, it is expected that plaster samples which are more "calcite-like" have smaller R-factors. As shown in Figure 5.6, the fitted Fourier transformed EXAFS regions of plaster (P3) and lime (L2) samples are presented. L2 mainly contains $Ca(OH)_2$ and CaO, while calcite is only the minor composition in it. Its R-factor is 0.81%, which is almost two times than that of the P3 sample. XRD and FTIR results for plaster samples show clear calcite peaks, and there is no clear evidence supporting that plaster samples contain ACC phases. Therefore, we suggest that the presence of the secondary phases ($Ca(OH)_2$ and other calcium carbonate polymorphs) cause larger R-factor rather than the heterogeneous structure of ACC phases. As shown in Figure 5.4, all plaster samples present a strong peak at 2.9 Å due to Ca-Ca bonds in $Ca(OH)_2$. For crystallized calcite samples (C1, C2, and PA), this strong peak is replaced by a much weaker peak–the calcite Ca-O bonding, and the peak at around 3.5 Å indicating the calcite Ca-Ca bond at around 3.5 Å grows. By fitting the Fourier transformed EXAFS regions of plaster samples, it

is clear that the R-factor is related to this two peaks. Smaller $Ca(OH)_2$ Ca-Ca peak and stronger calcite Ca-Ca stabilize the fitting (smaller R-factor).

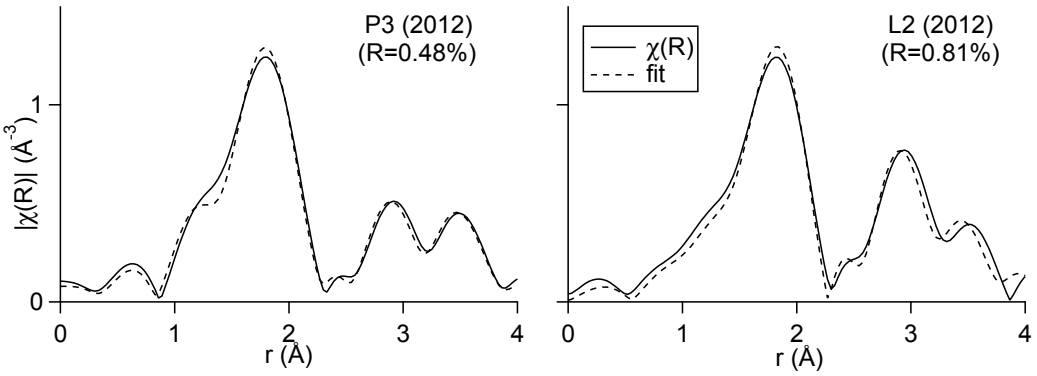

Figure 5.6: Fourier transforms of EXAFS regions of P3 and L2. Lime only contains small amount of calcite based on its FTIR spectrum.

As shown in Table 5.4, R-factors for plaster samples varies with temperatures rather than raw materials, which confirms the recent research carried out by Toffolo *et al.* [55]. They studied carbonation processes in lime and plaster samples using FTIR method and suggested the starting materials do not significantly influence the composition of plaster or lime samples. Our method can quantitatively differentiate plaster samples based on the R-factor. As shown in Figure 5.4, the R-factor for a plaster sample can be a measure of how close the sample is to ideal calcite.

It is surprising that two calcite standards (C1 and C2) have relative large R-factors of 0.23% and 0.19%, which are even larger than some plaster samples. We think this is likely because some multiple scattering paths, like Ca-C-O, were not considered during our fitting, causing amplitudes to be underestimated [109]. It is clear that a fitted data is always slightly different than an experimental data. However, there is still a strong correlation between R-factors and preparation temperatures for plaster

samples.

5.6 Conclusions

In this chapter, we studied how close plaster samples are to ideal calcite by using XAFS measurements. The results of XRD and FTIR measurements indicate all plaster samples contain calcite and a large portion of $Ca(OH)_2$. XRD patterns and XANES spectra of plaster samples prepared under different temperatures are similar. However, the quantitative analyses of EXAFS spectra indicate that not all samples are close to ideal calcite. Our results are consistent with earlier reports that carbonation processes in plaster samples are strongly dependent on calcination temperatures, rather than starting materials [55]. Moreover, we also demonstrate that the XAFS measurement is a powerful method even for characterizing mixtures.

Chapter 6

^{13}C related features in mid-infrared spectra of calcite

This chapter is a manuscript in preparation. The authors are Ben Xu, Anna Hirsch, Leeor Kronik, and Kristin M. Poduska.

6.1 Abstract

By systematically varying the ^{13}C:^{12}C content of calcite ($CaCO_3$), we show that its vibrational properties are more complex than one would expect from a simple mixture of the two isotopically pure end members. To do this, we pair experimental data from Fourier transform infrared (FTIR) measurements with theoretical calculations in the mid-IR range (500-1700 cm^{-1}), and find good quantitative agreement with peak shifts and with relative peak intensities. These results highlight the need to consider a range of isotopic compositions to account for the complex interactions that can occur when isotopic "defects" are present in high concentrations well beyond the dilute (non-interacting) limit.

6.2 Introduction

Isotopic substitution is a common strategy for gaining insight into the structure of solid materials. In some cases, isotopic enrichment can increase the efficiency of a measurement technique. For example, the acquisition time of high quality solid state nuclear magnetic resonance data is reduced in ^{13}C enriched calcite [112,113]. In other cases, isotopic substitutions can aid peak assignment, e.g., in vibrational spectra [42]. Isotopic substitution can also directly impact material properties, superconductors such as MgB_2 exhibit isotopic effects in their phonon-mediated electronic properties [114].

Calcite ($CaCO_3$) is abundant in natural minerals. Its structure and shape are strongly dependent on the formation environments and are very interesting to researchers [25,30,52,55]. Since that the vibrations in calcite are significantly influenced by the structure, plenty of articles focused on the vibrations in calcite [22, 23, 62, 80]. Isotopic effects on the vibrational spectra of calcite have been studied over many decades. In its naturally occurring state, calcite has a ^{13}C:^{12}C ratio of 1% while oxygen isotopes have a ^{18}O:^{16}O ratio of 0.1% [115,116]. Due to the low natural abundance of the heavier ^{13}C and ^{18}O isotopes, there were several attempts to synthetically enrich the isotope content in carbonate minerals. Decius *et al.* synthesized carbonate minerals enriched in ^{13}C and found the ^{13}C ν_2 peak was around 848 cm^{-1} [41]. More recently, Gillet *et al.* reported infrared (IR) and Raman measurements on 80% ^{18}O-substituted calcite to demonstrate similar isotopic effects [42]. The vibrational spectra for these isotopically substituted samples are especially complicated because there are three nonequivalent oxygen atoms in a single CO_3^{2-} unit, which means that the peaks split depending on the specific position of the oxygen atom isotope in the carbonate unit.

In the last decades, significant advances have been made in computational methods

and tools that allow calculations of vibrational wavenumbers and intensities for calcite [22,38,44,117] and other carbonated solids [1,51,118,119]. Some of these calculations included isotopic effects. Prencipe *et al.* [43] and Valenzano *et al.* [44] found that calcite fully substituted with the ^{13}C isotope will shift the carbonate normal modes, ν_2 and ν_3, to lower wavenumbers by 27 and 40 cm^{-1}, respectively.

Due to the low natural abundances of the heavier ^{13}C and ^{18}O isotopes, there has been much debate about the role that these isotopes might play in the origin of weak peaks in the calcite vibrational spectrum [50]. This is well illustrated by the representative Fourier transform infrared (FTIR) spectrum of calcite, given in Fig. 6.1. In addition to the three main absorption peaks of calcite (see detailed view in Fig. 6.1(b), (c) and (d)) there are clearly additional spectral features. In Fig. 6.1(b), in addition to the ν_3 absorption peak centered at 1433 cm^{-1}, two small shoulders appear. In the ν_2 region (875 cm^{-1}, Fig. 6.1(c)) an additional weak absorption peak at 848 cm^{-1} is easily seen. Interestingly, the weak absorption on the lower energy side of the ν_2 peak was first reported decades ago [120], but its origin has been debated. Two optional explanations for the origin of these spectral features were suggested: the combination of ν_4 and a lattice mode [49,51] or an isotopic shift [1,41,43,121].

One way to approach this question is to systematically examine the consequence of various levels of isotopic substitution. Naively, for different isotopic enrichment levels, one would assume that a linear interpolation between the two end members, calcite with 100% ^{12}C and 100% ^{13}C, would be sufficient. In chemical alloys, this assumption is often reasonable, as is the case for lattice constants in solid solutions, where it is known as Vegard's law [122]. However, this is not necessarily the case.

In this study, we systematically examined the influence of isotopic substitution on the spectral characteristics of calcite spectrum by experimental vibrational spectroscopy (FTIR and Raman). Using first principle calculations based on density

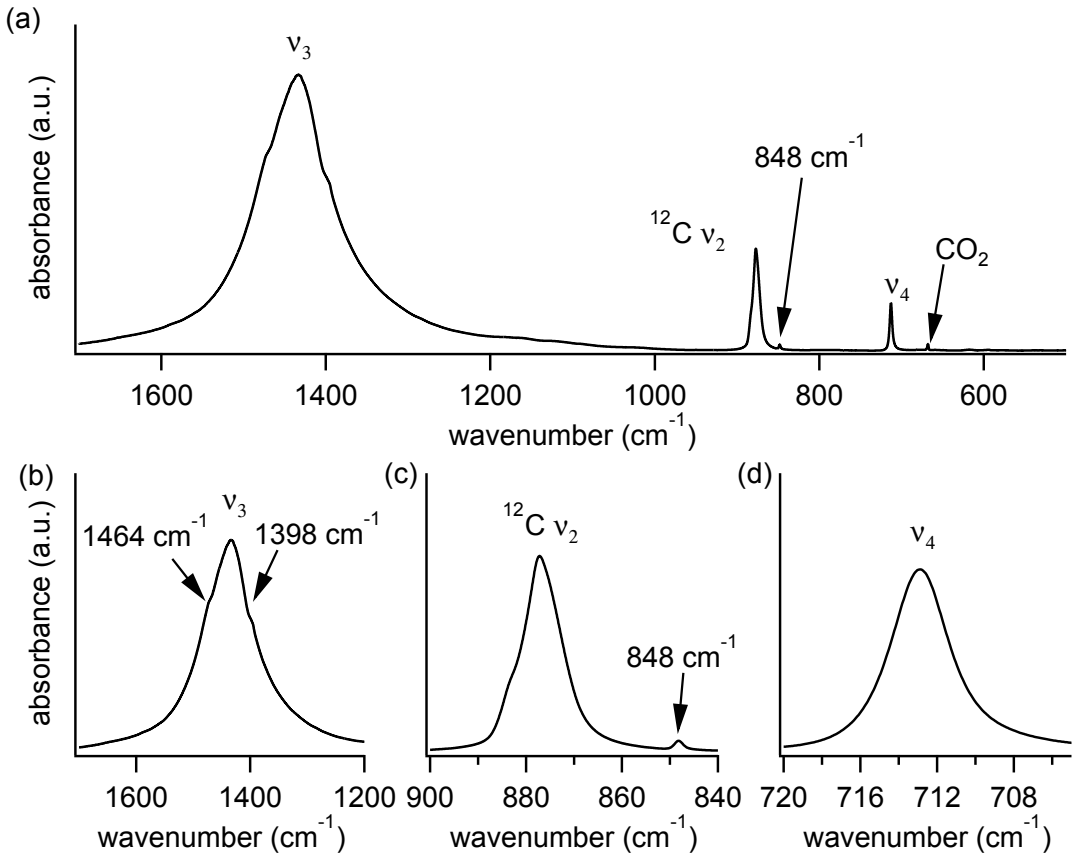

Figure 6.1: (a) A representative FTIR spectrum of calcite. The three vibrational modes of calcite due to the carbonate group ν_2 (out-of-plane bend), ν_3 (asymmetric stretch) and ν_4 (in plane bend) are labeled. The weak CO_2 (gas-phase) peak is not related to the calcite structure. (b)-(d) Detailed views of each of the vibrational modes.

functional theory (DFT) performed by our collaborators, we definitively determine the origin of the debated peaks is due to the isotopic content of the sample. Furthermore, focusing on the case of ^{13}C enrichment in calcite, and comparing experimental vibrational spectra with theoretical calculations, we show that peak position and intensity changes cannot be explained by simple interpolation. This research highlights the need to account for such coupling when considering isotopic substitution beyond the dilute limits.

6.3 Methods

6.3.1 Experimental details

Synthesized calcite was made by the method described in our previous paper [62]. 25 mL of 5 mM Na_2CO_3 and 1 mL of 60 mM $CaCl_2$ were used for preparation of calcite powders. The $Na_2^{12}CO_3$ and $Na_2^{13}CO_3$ solutions were mixed with the $Na_2^{12}CO_3$ concentration of 100%, 50%, 25%, 12.5%, and 0%. In this way, calcite samples with different concentrations of ^{13}C were produced. $Na_2^{13}CO_3$ powders were bought from Sigma-Aldrich Co.

We obtained FTIR spectra using a Bruker Vertex 70v vacuum spectrometer (<1 hpa) over a wavenumber range of at 4000 cm^{-1} to 500 cm^{-1} with a resolution of 1 cm^{-1}. The good vacuum was essential to eliminate contributions from water vapor, especially in the ν_3 region. The high resolution scans were also important to resolve the shoulders on the ν_3 peak and to resolve the weak 848 cm^{-1} peak. We did all measurements in a transmission geometry: synthesized calcite was ground with spectrophotometric grade KBr and then pressed into 7 mm diameter pellets under 2 tons of pressure. Before measurements, pellets were heated to 350 °C at the step of 110 °C in 3 hours to eliminate the influences of water and other $CaCO_3$ polymorphs. OPUS 7.0 (Bruker

Inc.) was used to determine peak positions, heights, widths, and areas. Data shown here are plotted as absorption spectra, but the quantitative analyses of peak widths and heights were compared using transmittance intensity.

For Raman spectra, we used a Renishaw inVia Raman Microscope 90Q314 with a Renishaw laser source (633 nm with max power of 500 mW). The wavenumber range of Raman measurements was 2000-100 cm^{-1}.

6.3.2 Computational details

DFT calculations were performed by our collaborators, Anna Hirsch (supervised by Dr. Leeor Kronik) and Dr. Leeor Kronik (Weizmann Institute of Science, Rehovot, Israel). All calculated vibrational spectra were obtained for a unit cell of hexagonal calcite. The calcite structure was firstly optimized before calculating the vibrational properties. The experimental coordinates were chosen from other experimental works [2,123]. Both were obtained by single crystal X−ray diffraction at room temperature. The optimized results are very similar to the published calculations [1, 43].

6.4 Results and discussion

Calcite FTIR spectrum is shown in Figure 6.1. Our investigations focus on three main regions as shown in Figure 6.1 (b), (c), and (d). The ν_3 peak (Figure 6.1 (b)) is centered at 1433 cm^{-1}, but we see two small shoulders on the peak. One is at 1398 cm^{-1} on the lower side, and the other one is at 1464 cm^{-1} on the higher side. In the ν_2 region (Figure 6.1 (c)), the strong ^{12}C peak at 875 cm^{-1} and the weak peak at 848 cm^{-1} are easily distinguished. The ν_4 peak (Figure 6.1 (d)) is at 713 cm^{-1}, which is due to the in-plane bend mode of carbonates. The clear and narrow ν_4 peak in our spectrum indicates the ordered structure of the calcite sample [22, 62].

Table 6.1: Experimentally determined peak positions from IR and Raman spectra (S1).

Mode assignment	IR peak position	Raman peak position
ν_4	712.9±0.2 cm^{-1}	710.1±0.5 cm^{-1}
^{13}C ν_2	848.2±0.2 cm^{-1}	-
^{12}C ν_2	876.9±0.2 cm^{-1}	-
ν_1	-	1084.4±0.5 cm^{-1}
^{13}C ν_3	1398±1 cm^{-1}	-
^{12}C ν_3	1433±1 cm^{-1}	-

Figure 6.2 shows the ν_2, ν_3, and ν_4 peaks at different ^{13}C concentrations. It is clear that the peaks at 1398 cm^{-1} and 848 cm^{-1} increase with ^{13}C concentration, indicating these two peaks are ^{13}C originated. The ^{12}C peaks at 1433 cm^{-1} and 875 cm^{-1} decrease due to smaller ^{12}C content. The ν_4 peak does not show extra ^{13}C peaks (Figure 6.2 (c))

The influences of ^{13}C on peak positions are shown in Figure 6.3. At the ν_3 region (Figure 6.3 (a) and (b)), the ^{12}C and ^{13}C peaks are differently affected by the ^{13}C concentration. The ^{12}C peak shifts to higher wavenumber (from 1433 cm^{-1} to 1437 cm^{-1}), while the ^{13}C peak shifts to lower wavenumber (from 1398 cm^{-1} to 1392 cm^{-1}). Experimental results (a) follow the calculated results (b), although calculations overestimated shifting wavenumber. At the ν_2 region (Figure 6.3 (c) and (d)), experimental results indicate that the ^{12}C and ^{13}C peaks shift to lower and higher wavenumber, which are opposite directions compared with ν_3 peaks. However, calculations suggest that the ν_2 and ν_3 regions are similarly affected by the ^{13}C concentration. For the ν_4 region, both experimental and calculated results indicate that its position moves to lower wavenumber with higher ^{13} concentration (Figure 6.3 (e) and (f)).

Figure 6.4 shows intensity ratios between the ^{13}C and ^{12}C ν_3 (a) and ν_2 (b) peaks. Both experiments and calculations give similar results. However, the intensity ratios for calculations are significantly larger than experimental results, indicating that the ^{13}C peak intensities were overestimated during calculations. The ^{13}C ν_2 area ratio

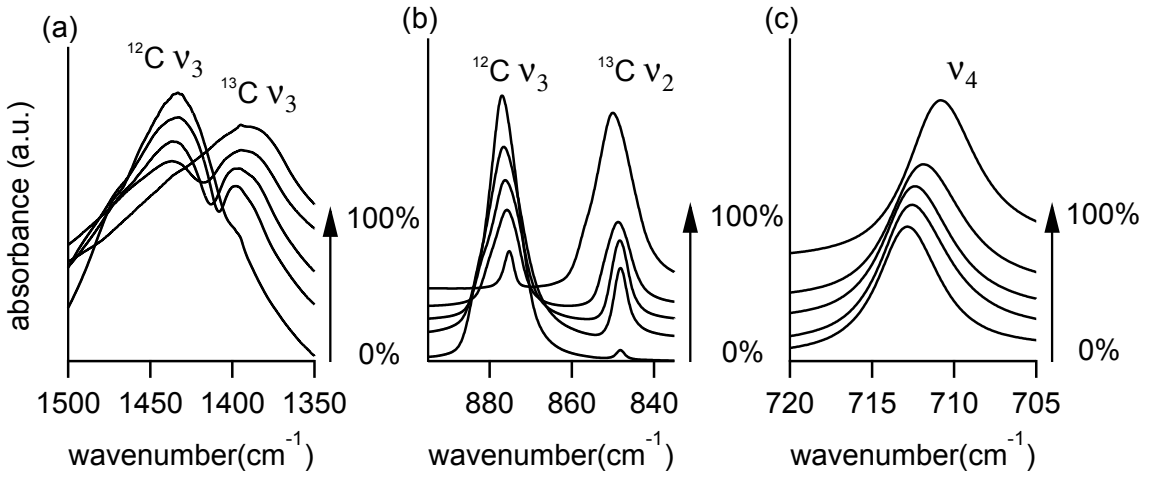

Figure 6.2: Zoomed views of the ν_3 (a), ν_2 (b) and ν_4 (c) regions of calcite samples with different ^{13}C concentrations. ^{13}C concentrations (bottom to top) are 0%, 13%, 25%, 50%, and 100%, respectively. The ν_3 and ν_2 regions show clear double-peak shapes. It is interesting that the ^{12}C ν_2 and ν_3 peaks also shift with ^{13}C concentration. The ν_4 region does not show the double-peak shape. But the ν_4 peak shifts to lower wavenumber due to the higher ^{13}C concentration.

for transmittance mode (a ratio is given by (^{13}C ν_2 area)/the total areas of ν_2 peaks (^{13}C ν_2+^{12}C ν_2)) is shown in Figure 6.4 (c). The transmittance spectra are converted from absorption spectra in OPUS software. It is noteworthy that area ratios match the ^{13}C concentration.

6.5 Conclusions

Our results show that the weak features in calcite ν_2 and ν_3 regions of our FTIR spectra are fully consistent with modes related to ^{13}C. Our investigations can be grouped in two regimes: the dilute regime, which is relevant for naturally occurring levels of ^{13}C, and the non-dilute regime, which applies to artificially enhanced proportions of ^{13}C. Both experiments and simulations were employed during our investigation. Although the concentration of ^{13}C is only around 1% [116], an IR spectrum of calcite can still

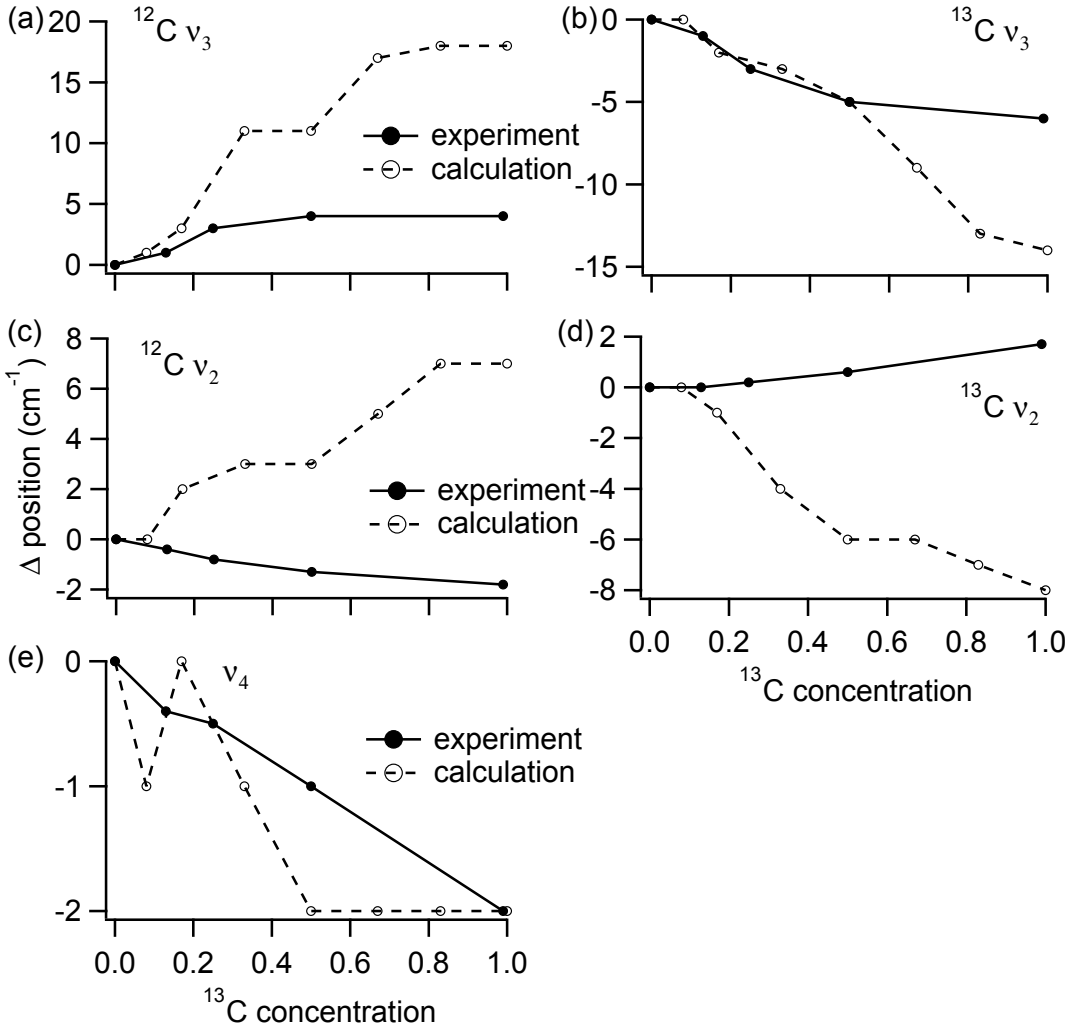

Figure 6.3: The influences of ^{13}C concentrations on the peak positions of ν_3 (a and b), ν_2 (c and d), and ν_4 (e) are presented. For the ν_3 and ν_4 peaks, calculations give the same results as experiments, although calculations overestimated the shifting wavenumber for the ν_3 region. For the ν_2 region, calculations do not show same results as experiments. The ^{13}C and ^{12}C peaks move to higher and lower wavenumbers, respectively, in our experiments, while calculations give opposite results.

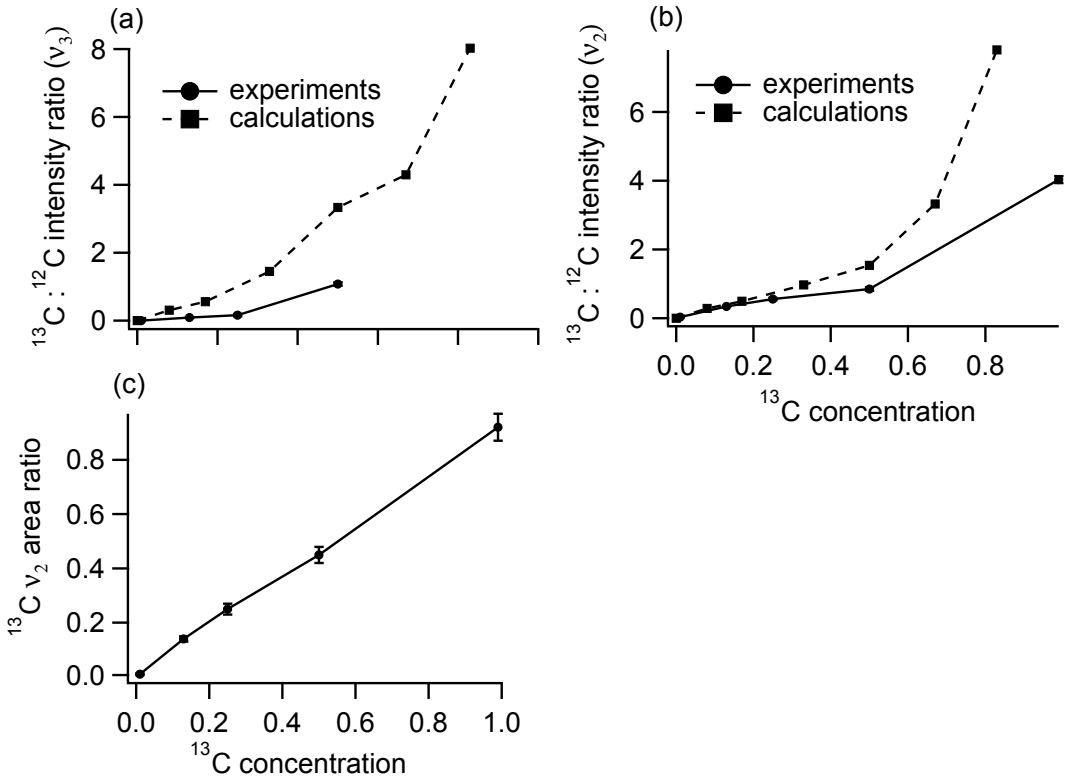

Figure 6.4: The influences of ^{13}C concentration on intensity ratios between the ^{13}C and ^{12}C ν_3 (a)) and ν_2 (b) absorption peaks are presented. The ^{13}C ν_2 peak area ratio is shown in (c). ^{13}C concentrations for experimental results are based on Na_2CO_3 powders for preparation, and real ^{13}C concentrations in calcite samples might be different due to the influences of CO_2 incorporation from the open air.

show clear evidences of its absence, which are the weak peaks at 1398 cm^{-1} (the ν_3 region) and 848 cm^{-1} (the ν_2 region). Weak ^{13}C peaks are at the lower side of the strong ^{12}C peaks due to the heavier atomic mass. For the ν_4 region, there is no ^{13}C peak. It is due to that energies of the ^{13}C and ^{12}C ν_4 vibration are the same [43, 44], and they give a single peak at the ν_4 region.

For ^{13}C enriched calcite, intensities for ^{13}C IR peaks increase due to the higher concentration. However, it is surprising that the peak positions for both the ^{12}C and ^{13}C peaks move when ^{13}C content changes. For the ν_3 and ν_4 regions, calculations and experiments show similar results with increasing ^{13} content: a) the ^{12}C and ^{13}C ν_3 peaks move away from each other, and b) the ν_4 peak move to the lower wavenumber. However, for the ν_2 region, calculations and experiments give opposite results. Simulations suggest that the ^{12}C and ^{13}C ν_2 peaks are suppose to behave the same as the ν_3 peaks. But the two ν_2 peaks actually move towards each other at higher ^{13}C content. One possible explanation is that there is strong interaction between dipoles caused by the ν_2 vibration [41], and this brings the discrepancy. Although calculations and experiments do not show agreements for the ν_2 region, they still give similar results for the ν_3 and ν_4 regions. Simulations on IR peak intensities also correspond to experiments for all vibrations, although calculations overestimate the intensities of ^{13}C peaks.

Our experimental data suggest that the amount ratio between ^{13}C and ^{12}C atoms equals to the area ratio between their ν_2 transmittance peaks. This finding may enable us to study the isotope concentration in a simpler way. However, the large uncertainty in the area ratio is the main problem. Further studies will be still needed for detecting isotopes in materials utilizing vibrational spectroscopy.

6.6 Supporting information

6.6.1 Comments on combination modes

Combination modes in calcite have been studied with symmetry-related arguments. In 1970, Donoghue *et al.* examined IR spectra for carbonate and nitrate minerals both experimentally and theoretically [49]. Based on group theory and the analysis of vibration symmetries, they suggested that the weak band at 848 cm^{-1} is due to the combination of $\nu_4(E_g)$ + lattice (u) modes, and is also enhanced by Fermi resonance with $\nu_2(A_{2g})$. Shortly after this, White reviewed all possible explanations that had been offered for this peak [50]. His conclusion was not decisive, but he did not rule out the possibility of combination modes. A very recent experimental study by Carteret *et al.* [51] continues the trend of suggesting combination modes, suggesting that the weak peak near the aragonite ν_2 peak is a combination mode. However, our results suggest the weak peak at 848 cm^{-1} is originated from the ^{13}C ν_2 vibration, although the natural abundance of ^{13}C is only 1%.This peak increases in ^{13}C enriched samples, as well as the peak at 1398 cm^{13}, which is due to the ^{13}C ν_3 peaks. Isotopic effects on combination modes are presented in Figure 6.5. The $\nu_1 + \nu_4$ mode does not show clearly difference when ^{13} content changes. The $\nu_1 + \nu_3$ mode has a sharp peak and a flat region at the lower side of the peak, both of them moves to lower wavenumber when ^{13}C concentration increase. The $2\nu_3$ peak show complicated shapes, and ^{13}C concentration changes have significant effects on it.

6.6.2 Comments on Raman results

In our Raman measurements on calcite powders (see Figure 6.6), we noticed that the ν_1 and ν_4 peaks are much narrower than the peaks of the lattice modes. The weak 848 cm^{-1} peak we observe is quite narrow, and we suggest this is a further evidence

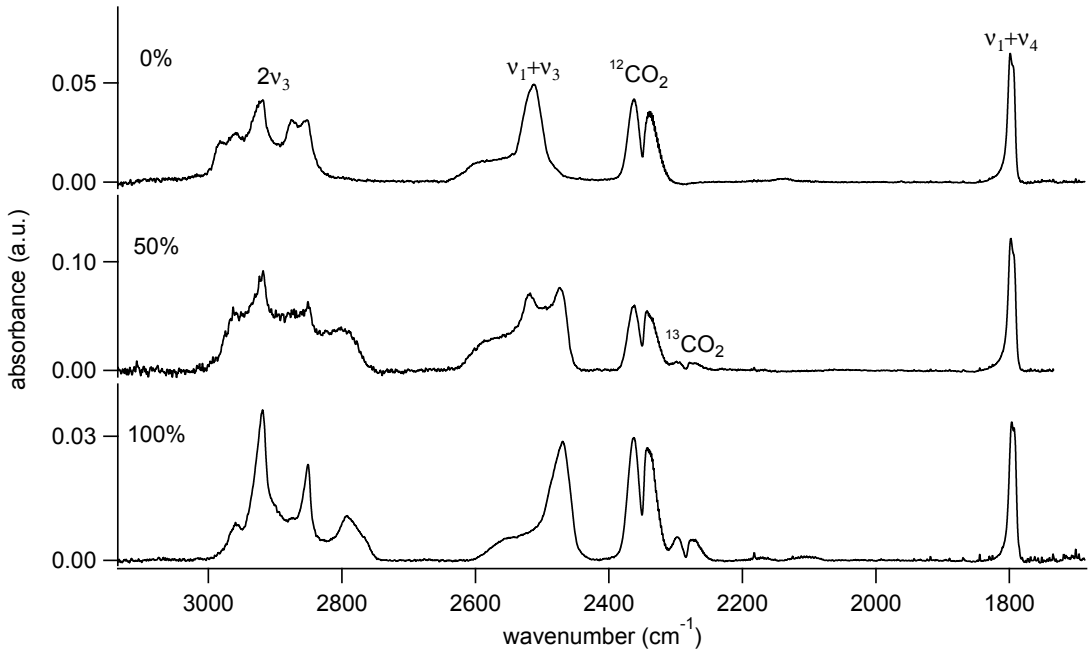

Figure 6.5: FTIR spectra of calcite samples in the range from 3135 to 1683 cm^{-1}. All spectra show clear CO_2 features, which is probably due to decomposition of small amount of calcite during heating and oxidation of unexpected organic matter. The ^{13}C concentration also affects the combination modes of calcite. The $2\nu_3$ mode has a complicated shape for all samples, indicating the complexity in the ν_3 mode. The $\nu_1 + \nu_3$ mode show both ^{12}C and ^{13}C features as the ν_3 mode. The $\nu_1 + \nu_4$ mode shifts to lower wavenumber with ^{13}C concentration as the ν_4 mode.

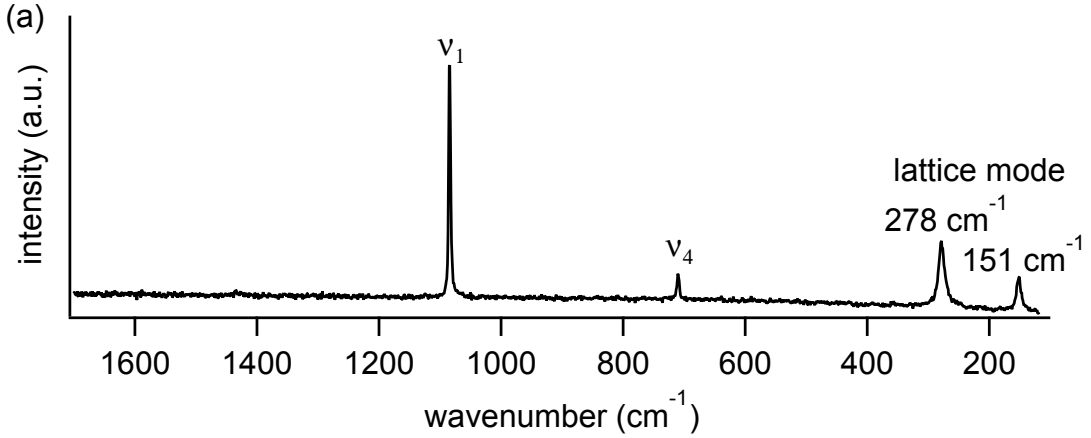

Figure 6.6: The Raman spectrum of a calcite sample with 0% ^{13}C concentration. Two sharp peaks at 1084 and 710 cm^{-1} are due to the ν_1 and ν_4 vibrations. Two broader peaks at lower wavenumber are due to lattice modes.

that this peak is not related to lattice mode combinations. These results are similar to that supported by Mg-carbonate studies done by Bischoff *et al.* in 1985 [107].

Calculations performed by other researchers also suggest the lattice modes are broader than the normal modes in calcite. Gueta *et al.* calculated the phonon dispersion relations for calcite (shown in the Supporting Information of Ref. [38]), indicating that the normal modes for the carbonate units are flat and well-localized at specific energies, while most of lattice modes are dispersive. We think that this helps to explain why the lattice modes for calcite give broader Raman peaks.

At the ν_2 region (Figure 6.1 (c)), there is a shoulder on the left side of the ν_2 peak near 882 cm^{-1}. We're not sure what this is, but it does appear in all of our calcite samples. We suspect it is the LO mode of ν_2 vibration based on Valenzano's calculations [44]. Since there is no lattice mode located at 170 cm^{-1}, this shoulder is unlikely from combination of ν_4 and one lattice mode.

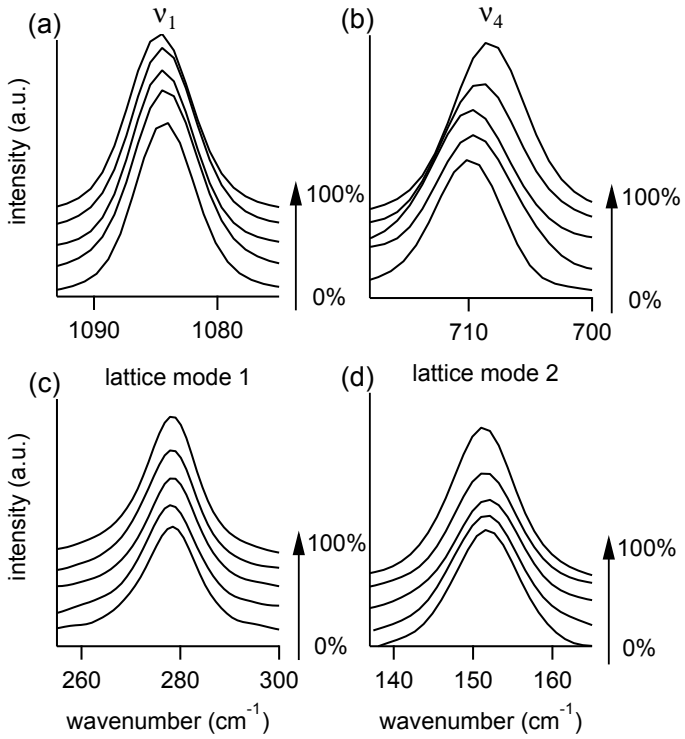

Figure 6.7: Zoomed views of the ν_1 (a), ν_4 (b) and two lattice modes (c and d) in Raman spectra for calcite with different ^{13}C concentrations. Only the ν_4 peak shifts to lower wavenumber with the higher ^{13}C concentration, all the other three Raman peaks remain constant.

Chapter 7

Acoustic detection of IR spectra from calcite minerals

The preliminary data for this chapter is not sufficient for a manuscript, so this chapter is written in general format.

7.1 Introduction

FTIR spectroscopy has been widely utilized in studying the composition of a material (solids, liquids, or gases) in many fields. It has a fast processing time and informative results [7,23,38]. However, the traditional FTIR technique requires careful preparation of samples for measurements. Samples are usually ground with potassium bromide and pressed into pellets to dilute the samples and avoid saturation in absorption spectra. Particle sizes and shapes within the pellets can strongly affect the spectra [45, 46]. Furthermore, the traditional FTIR technique cannot be applied to some bulk samples if they are very opaque to infrared light, because there will be strong scattering effects. Other techniques have been developed to cover the shortfalls of

traditional FTIR measurements, and FTIR-photoacoustic (FTIR-PAS) spectroscopy is one of them [68, 124, 125].

The photoacoustic effect was first discovered by Alexander Graham Bell in 1880 [126]. He found that a solid in an enclosed cell exposed to chopped sunlight generated audible sound. However, this effect was regarded as having no practical value and its application was not developed until the 1970s [125]. Theoretical studies were then performed by Rosencwaig *et al.* [127] and McDonald *et al.* [128]. They suggested that the primary source of the acoustic signal was the periodic heat flow from the solid to the surrounding gas due to the chopped light. The photoacoustic effect was then used to investigate the absorption coefficient as a function of depth in a solid [129, 130]. More recently, the development of photoacoustic imaging allows researchers to monitor the dynamics of biological processes [131].

FTIR-PAS spectroscopy is FTIR spectroscopy with an acoustic detector [130]. A schematic of FTIR-PAS spectroscopy is shown in Figure 7.1. A sample absorbs IR energy, and this heats the sample. Oscillations of the input light produce thermal waves, that change the gas pressure in contact with the sample. The oscillated pressure (sound signal) is transferred through the medium gas and is detected by a microphone or a cantilever. This is a PAS signal. The Fourier transform of PAS signals will give a FTIR-PAS spectrum, which contains the information about IR-active vibrational modes in the solid. For a PAS measurement, helium is usually used as the medium gas because it can enhance the transfer of heat and boost the signal [130].

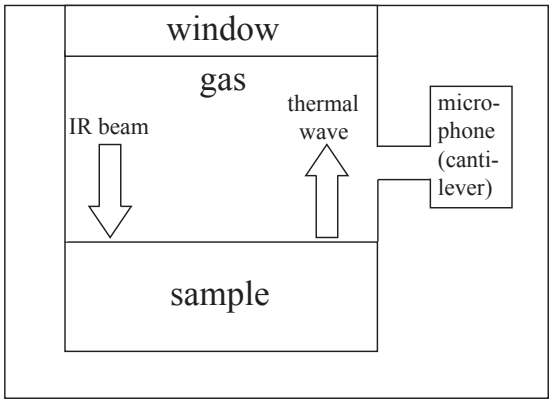

Figure 7.1: A schematic picture of FTIR-PAS detection.

Quantitative analyses of FTIR-PAS spectra requires fully understanding sample preparation effects. In this chapter, calcite powdered samples at different grinding levels and amounts were measured by FTIR-PAS spectroscopy. Effects of particle sizes and sample amounts are evaluated. Differences between FTIR spectra with the optical and PAS detectors are also compared and analyzed.

FTIR-PAS spectroscopy can be utilized to detect isotopic and combination modes in calcite. The reasons causing the enhancement of weak optical peaks are related to the mechanisms of acoustic detection. The effects of sample amounts on PAS signals are minimal. However, the PAS amplitude decrease with decreasing particle sizes due to the higher surface to volume ratio. By comparing the published theoretical results to our FTIR-PAS spectra, we suggest that weak and broad FTIR-PAS peaks for calcite, which cannot be readily detected by optical FTIR spectroscopy, are due to combination modes. We also show that the ^{13}C ν_2 peak in a calcite PAS spectrum shows clear structural dependency.

Table 7.1: Sample details are listed. The heating temperature and raw starting material for preparing the plaster sample are included.

standards	raw material	
C1	analytical-grade calcite (Merck)	
C2	spar calcite	
plaster	starting material	temperature
P1	analytical-grade calcite (Merck)	900°C

7.2 Experimental details

FTIR-PAS spectra were collected using a Bruker IFS 55v/S spectrometer (Bruker, Inc.) equipped with an MTEC 300 photoacoustic accessory (MTEC Inc.) using a wavenumber range of 4000 cm^{-1} to 500 cm^{-1} and a resolution of 1 cm^{-1}. Before measurements, a background spectrum was measured from black carbon, and helium was used as the medium gas [130,132]. Water vapor and carbon dioxide in the sample chamber were eliminated by introducing in a helium stream into the chamber for 10 minutes before it was sealed. The sample was irradiated with modulated light (1 KHz) to produce the thermal wave. Optical FTIR spectra were obtained using a Bruker Vertex 70v vacuum spectrometer (Bruker, Inc.) in transmission mode over a wavenumber range of at least 4000 cm^{-1} to 500 cm^{-1} with a resolution of 1 cm^{-1}. IR peak intensities were assessed using OPUS 7.0 software (Bruker, Inc).

Calcite spar (Mexico), analytical-grade calcite (Merck), and analytical-grade calcite plaster are the study cases. Sample details are listed in Table 7.1. Calcite spar and analytical-grade calcite have well ordered 3D periodic structure as discussed in Chapter 3 and Chapter 4. Plaster samples were provided by Michael B. Toffolo, supervised by Dr. Elisabetta Boaretto (Weizmann Institute of Science, Rehovot, Israel) [55], as described in Chapter 5. XRD studies on these samples indicate that plaster has broad XRD peaks due to lattice strain and the small domain size, and they contain $Ca(OH)_2$ (see more details in Chapter 4 and 5).

7.3 Results

7.3.1 Mass effects on FTIR-PAS spectra

PAS spectra of well-ground powder samples of calcite spar (C2) with different amounts (masses) are presented in Figure 7.2. Spectral intensities remain constant within uncertainties, as shown in Figure 7.2 (c). Peak intensities do not change significantly with sample amounts, although there is a slight decrease of peaks with very low mass. It is due to that only the surface powder absorbs IR energy and produce PAS signals. Thus, the sample amount has limited effects on PAS intensities only when there is a very small amount of sample. Larger amounts of sample in chamber decrease the distance between the sample and the PAS detector, which attributes to the slight growth of peaks [127, 128].

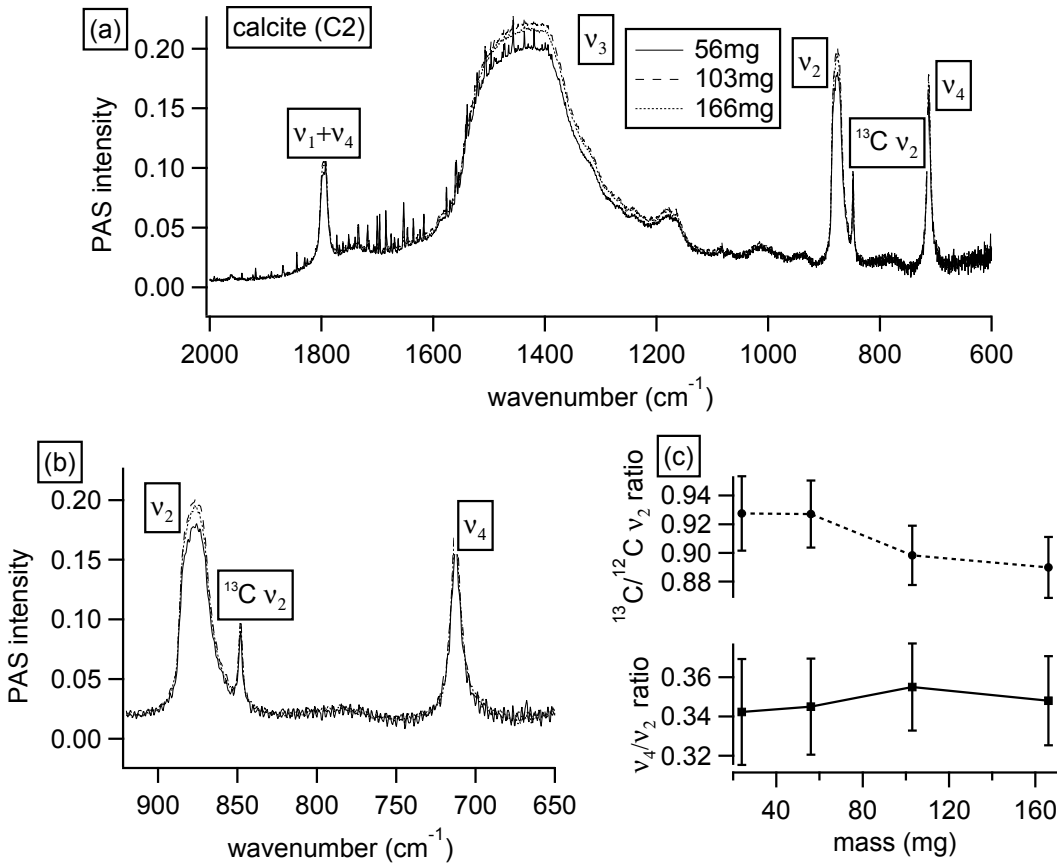

Figure 7.2: FTIR-PAS spectra of powdered spar calcite for 3 different masses. Samples are in the same grinding levels to eliminate the particle size influences. The noise on the high wavenumber side of the ν_3 peak arises form water vapor. (b) presents the details of the ν_2 and ν_4 regions. (c) shows that the peak ratios are the same, within experimental uncertainties.

7.3.2 Intensities (PAS detector *vs.* optical detector)

Representative FTIR spectra of analytical-grade calcite (C1) measured by the optical and PAS detectors are shown in Figure 7.3. The PAS and optical detectors give the same position for each peak, as shown in Table 7.2. The main difference between the

Table 7.2: Peak positions measured by the optical and PAS detectors.

peak	optical	PAS
$2\nu_3$	-	2872-2982 cm^{-1}
$\nu_1 + \nu_3$	2517 cm^{-1}	2517 cm^{-1}
$\nu_3 + \nu_4$	-	2143 cm^{-1}
$\nu_1 + \nu_2$	-	1956 cm^{-1}
$\nu_1 + \nu_4$	1798	1798 cm^{-1}
ν_3	1428 cm^{-1}	1420-1470 cm^{-1}
^{12}C ν_2	875 cm^{-1}	875 cm^{-1}
^{13}C ν_2	848 cm^{-1}	848 cm^{-1}
ν_4	712 cm^{-1}	712 cm^{-1}

FTIR-PAS and optical FTIR spectra is that relative intensities given by PAS detector are enhanced, and weak PAS peaks are not readily visible with optical detection.

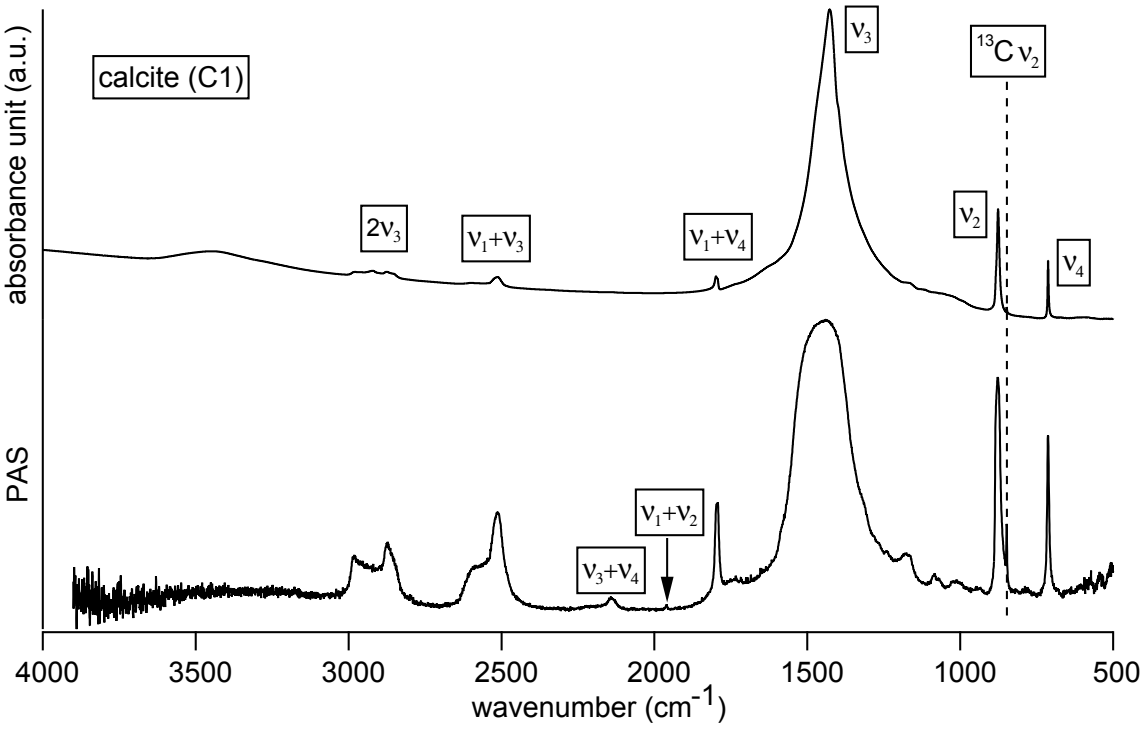

Figure 7.3: Representative FTIR spectra of analytical-grade calcite (C1) using the PAS (lower) and optical (upper) detectors are presented. Intensities are scaled to clearly show the details of spectra. Normal vibration modes and their combination modes are labeled. Peak positions in PAS and optical FTIR spectra are the same. However, their relative intensities (normalized to each ν_3) are different. Weak optically-detected peaks are enhanced with the PAS detector.

Peak intensities with two detectors are listed in Table 7.3. Four peaks are included, which are $\nu_1 + \nu_4$ (1798 cm^{-1}), ^{12}C ν_2 (875 cm^{-1}), ^{13}C ν_2 (848 cm^{-1}), and ν_4 (712 cm^{-1}). Their intensities are normalized to ^{12}C ν_2. It is clear that the relative peak intensities given by PAS detector are larger than their optical counterparts.

Theoretical work done by Rosencwaig *et al.* [127] and McDonald *et al.* [128] suggested that a PAS signal is proportional to the optical absorption coefficient of a

solid. Based on earlier reports [22,45], the absorption of a sample dispersed in a KBr pellet can be given by:

$$A = -\frac{h}{d}\log[(1-f) + fe^{-\mu d}] \tag{7.1}$$

where A, h, d, f, and μ are absorbance (optical intensity), pellet thickness, particle diameter, sample fraction in the KBr pellet, and absorption coefficient, respectively. Absorption coefficients of the ν_2 and ν_4 peaks are $\mu_2 = 1.0\ \mu\text{m}^{-1}$ and $\mu_2 = 0.3\ \mu\text{m}^{-1}$ [22, 45]. Based on the results given by Rosencwaig *et al.* [127] and McDonald *et al.* [128], the intensity ratio between the ν_2 and ν_4 PAS peaks should be equal to the ratio between their absorption coefficients. However, this is not consistent with our results (shown in Table 7.3). One possible reason is that samples used for our FTIR-PAS measurements were powders, while the reported calculations are based on bulk samples [127, 128].

In our case, squares of PAS intensity ratios match optical intensity ratios (transmittance mode), and this can be explained as follows. The incident light has an energy of $I_0(k)$, where k is the wavenumber, but only a $r(k)$ portion of the energy is transferred to "sound", which is given by

$$E_{sound} = r(k)I_0(k) \tag{7.2}$$

where E_{sound} is the energy of "sound". For PAS detector, it measures the sound pressure which is the amplitude ($A(W)$) of "sound", and the relation between amplitude and energy is:

$$A(k)^2 \ \propto \ r(k)I_0(k) \tag{7.3}$$

in this way, the intensity ratio between two PAS peaks is:

$$h(k_i) : h(k_j) = A(k_i) : A(k_j) \tag{7.4}$$

Table 7.3: Peak intensities in PAS and optical FTIR spectra shown in Figure 7.3. The intensities of transmittance spectrum are converted from absorption spectrum using OPUS 7.0 software. Peak intensities are normalized to the ν_2 peak and background is subtracted. Squares of PAS intensities are included for comparison.

	optical absorbance	optical transmittance	FTIR-PAS	(FTIR-PAS)^2
ν_2	1.000±0.008	1.000±0.007	1.00±0.03	1.00±0.06
ν_4	0.566±0.006	0.708 ± 0.005	0.89±0.03	0.79±0.06
^{13}C ν_2	0.049±0.004	0.074 ± 0.003	0.34±0.02	0.11±0.04
$\nu_1 + \nu_3$	0.131±0.004	0.179±0.005	0.43±0.02	0.18±0.04

where $h(k)$ is the intensity of a PAS peak. For an optical FTIR spectra (transmittance), a peak intensity is given by:

$$H(k) = 1 - T(k) = R(k)I_0(k) \tag{7.5}$$

where $H(k)$ is the peak height, $T(k)$ is the transmittance and $R(k)I_0(k)$ is the absorbed light energy. Then the intensity ratio between two transmittance peaks is:

$$H(k_i) : H(k_j) = R(k_i)I_0(k_i) : R(k_j)I_0(k_j) \tag{7.6}$$

assuming that the $r(k)$ and $R(k)$ has a linear relationship (this assumption can well explains our results):

$$\begin{aligned} H(k_i) : H(k_j) &= r(k_i)I_0(k_i) : r(k_j)I_0(k_j) \\ &= A(k_i)^2 : A(k_j)^2 = h(k_i)^2 : h(k_j)^2 \end{aligned} \tag{7.7}$$

7.3.3 Grinding effects on FTIR-PAS spectra

Figure 7.4 shows the FTIR-PAS spectra of calcite (C1) powders with different particle sizes due to larger grinding times. The intensities increases with more grinding is due to larger total surface area in smaller particles [68]. PAS signals are produced from

surfaces of powders, and the PAS signal is proportional to surface area. Due to the larger surface area of smaller particles, the source that generates thermal waves increases significantly, and a higher PAS signal is detected. For optical spectra, the spectral intensities also increase with smaller sample particle sizes, while it is due to a different effect: pellets with smaller particle sizes absorb more incident light [22, 45].

A plot of ^{13}C:^{12}C peak height ratios *vs* ν_4:ν_2 peak height ratios is presented in Figure 7.4 (c). and a strong grinding effect is illustrated. Both ratios decrease with grinding, which indicates that stronger peaks grow more rapidly with increased grinding times.

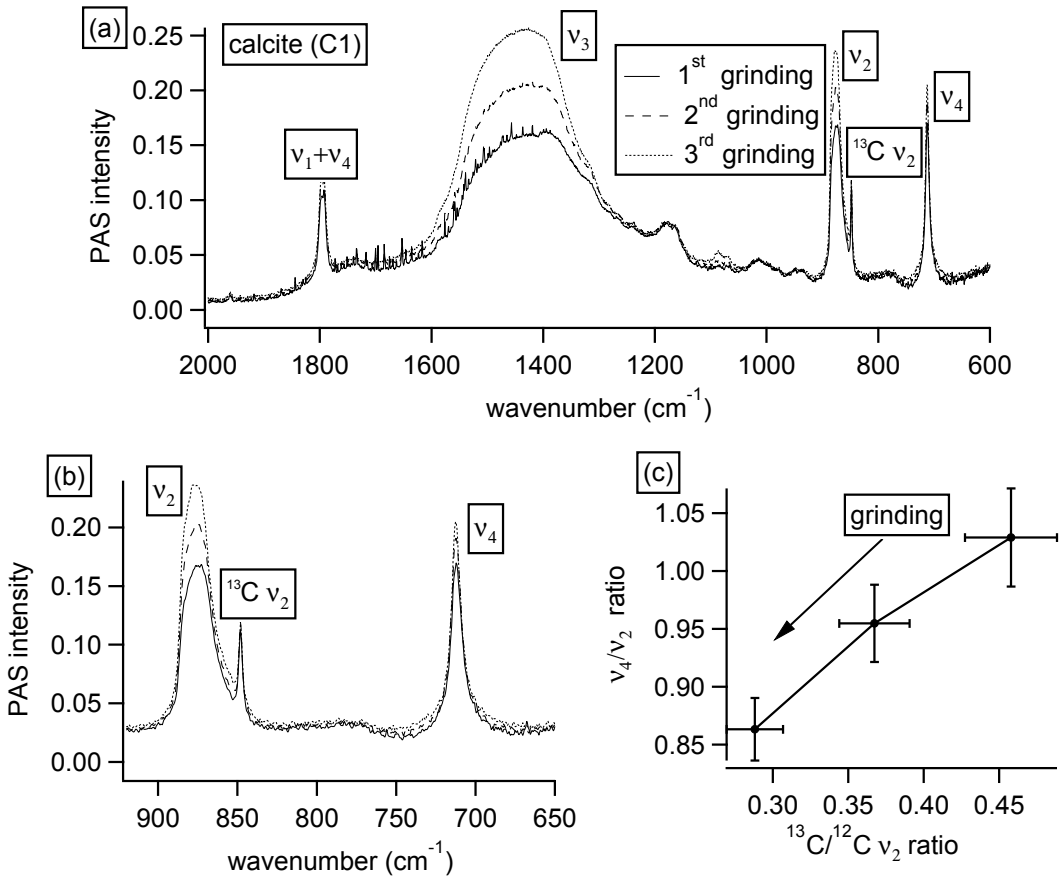

Figure 7.4: FTIR-PAS spectra of calcite (C1) powders with different particle sizes (grinding levels). Amount for all spectra is the same (58 mg). The noise on the high wavenumber side of the ν_3 peak arises from water vapor. (b) presents the details of the ν_2 and ν_4 regions. (c) shows that grinding levels strongly affect relative peak intensities.

7.4 Discussion

Isotope and combination peaks in an optical FTIR spectrum are usually weak and obscured by noise, making quantitative analyses very difficult. However, these peaks

Table 7.4: Positions of possible combined peaks that are only present in FTIR-PAS spectra of calcite. Possible origins of them are listed. Data for lattice modes are from Ref. [3] and [1]. $*$ indicates calculated result.

observed peak (cm^{-1})		origin (cm^{-1})
2137	=	ν_3+ν_4 [1428+712]
1960	=	ν_1+ν_2 [1085+875]
1180-1164	=	ν_2+lattice mode (E_u or A_{2u}) [875+(297 or 303)]
1086-1066	=	ν_2+lattice mode (E_u or A^*_{2g}) [875+(223 or 193)]
1020-980	=	ν_2+lattice mode (E_g or E_u) [875+(156 or 102)]
		ν_4+lattice mode (A_{2u}) [712+303]
976-928	=	ν_2+lattice mode (A_{2u} or E_u) [875+(102 or 92)]
		ν_4+lattice mode (E_u) [712+223]

are clearly presented in a FTIR-PAS spectrum, and therefore, FTIR-PAS spectroscopy is helpful for studies of isotopic and combination modes.

Combination modes that involve calcite lattice modes are weak and usually cannot be recognized in an optical FTIR spectrum. Theoretical calculations do not predict these combination modes either [1, 118]. Fortunately, information about these modes are easy to extract from a FTIR-PAS spectrum, as shown in Figure 7.3. Based on earlier results given by Ref. [3] and [1], the peaks which are probably originated from combination modes (only observed in the FTIR-PAS spectrum) are listed in Table 7.4. It is obvious that peak positions match the combination modes.

The ^{13}C ν_2 peak is interesting because it is different from the ^{12}C ν_2 peak, which is not expected. Previous studies on calcite using optical FTIR indicated that the ν_2 peak remains unchanged with structural disorder, while the ν_4 peak changes [38, 62]. Our conclusions in Chapter 4 also indicate that the relative intensity of the ν_2 peak remains nearly constant in different calcite samples, while ν_4 significantly changes. It is expected that the ^{13}C ν_2 peak should behave the same as the ^{12}C ν_2 peak. However, based on our previous results, the relative intensities of both the ^{13}C ν_2 and ν_4 peak decrease in plaster samples, while the ^{12}C ν_2 peak does not (Chapter 5). Based on earlier reports [133,134], concentrations of ^{13}C vary in the range of less than 10 permil

in natural samples, and therefore, it is unlikely that the decrease is due to the ^{13}C concentration change. It is difficult to use an optical FTIR spectrometer to detect them. However, the ^{13}C ν_2 peak becomes clear in a FTIR-PAS spectrum, as shown in Table 7.3.

PAS spectra of two calcite samples (C1 and C2) and a plaster sample (P1) are presented in Figure 7.6. All samples were well ground to eliminate the effects of particle size effects. C1 and C2 are well crystallized based on our XRD analyses (Chapter 4). Their ν_4 and ^{13}C ν_2 peaks are sharp and clear, as shown in Figure 7.6 (b). The plaster sample (P1) have smaller crystalline domain sizes and more lattice strain (Chapter 4), and its ν_4 and ^{13}C ν_2 peak is weak and more broad.

We measured FTIR-PAS spectra of the C1, C2, and P1 samples with different grinding times, and the plot of the ^{13}C ν_2 intensity vs the ν_4 intensity for all the spectra is presented in Figure 7.6 (c). The intensities are normalized to the ^{12}C ν_2 peak. The clear grinding effect can be observed. As shown in Figure 7.6 (c), dots for calcite and plaster samples locate at their specific regions. Furthermore, C1 and C2 also have different peak ratios. Plaster sample (P1) has smaller ν_4 and ^{13}C ν_2 intensities than calcite samples. A strong correlation between the ^{13}C ν_2 and ν_4 peaks is demonstrated, and we attribute the changes in the ^{13}C ν_2 peak to the same reason (disorder) causing changes in the ν_4 peak. However, the reasons why the ^{13}C ν_2 and ν_4 peaks correlate with each other are still unknown, and it requires further investigation.

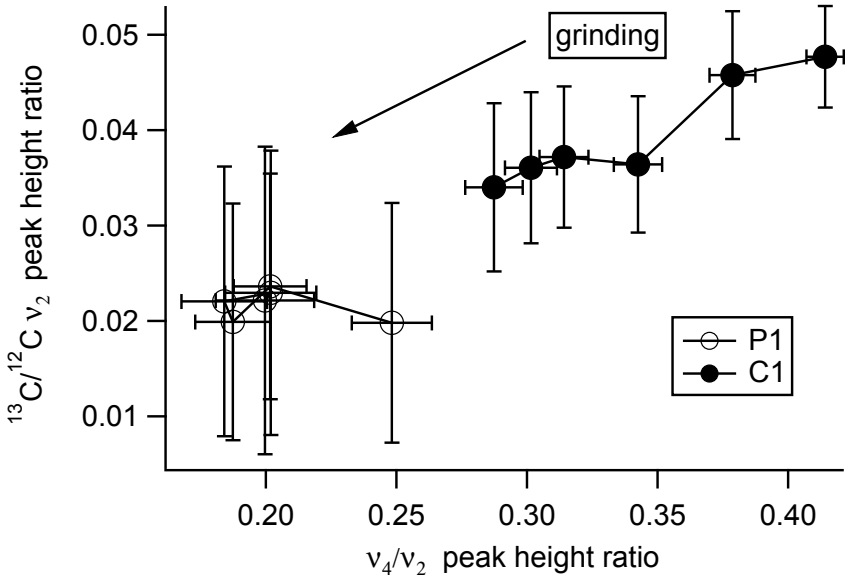

Figure 7.5: The ^{13}C ν_2 intensity vs the ν_4 intensity for optical FTIR absorption spectra of the P1 and C1 samples with different grinding levels. The ^{13}C ν_2 peak is weak in optical spectra (especially for the plaster sample). Due to the large signal-to-noise ratio, the differences in the ^{13}C ν_2 peak of the plaster and calcite samples are not clear.

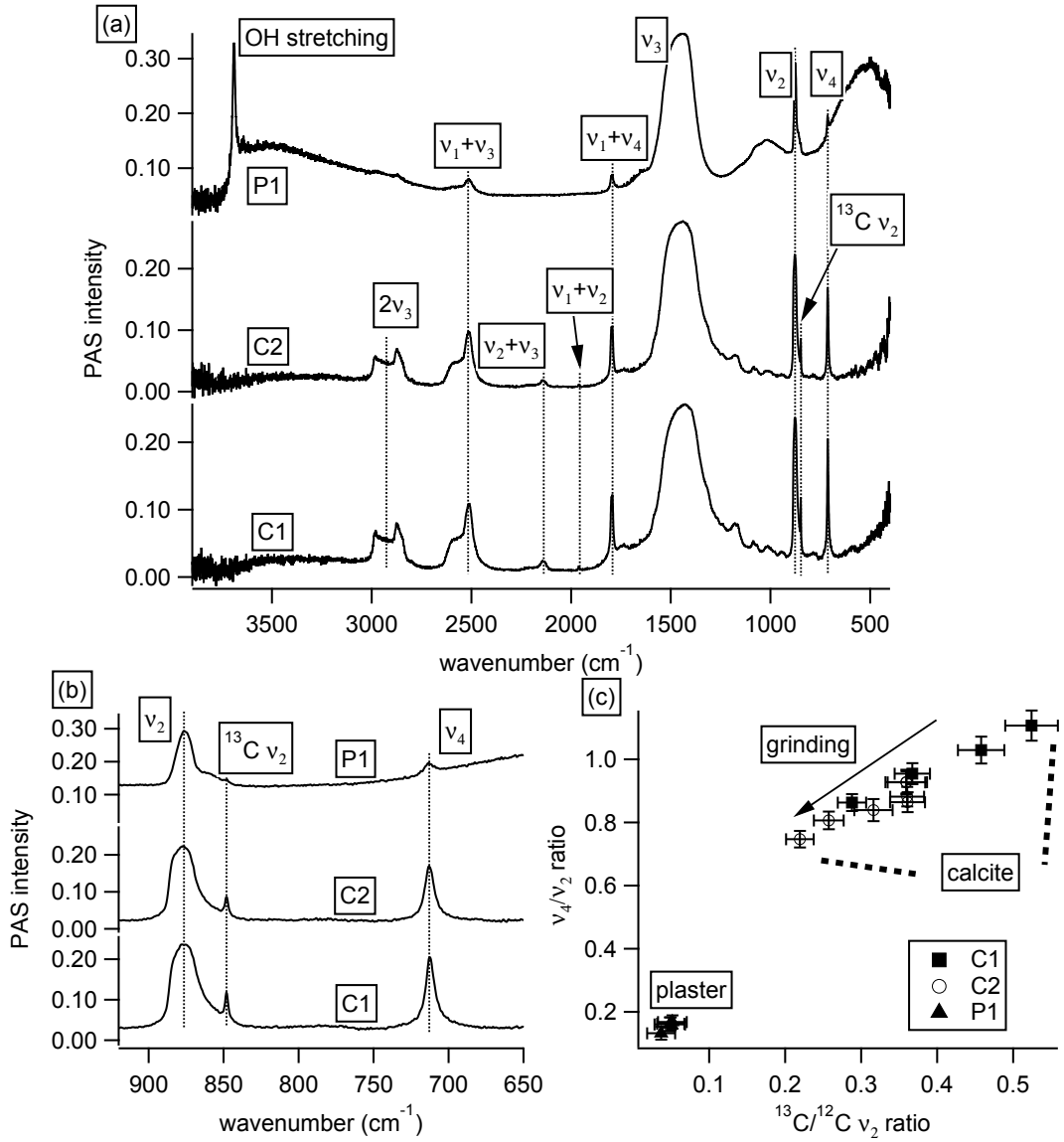

Figure 7.6: FTIR-PAS spectra of different calcite samples.

7.5 Conclusion

Peak intensities in a FTIR-PAS spectrum are not affected by the sample amount, but do strongly depend on grinding levels (particle sizes). Weak peaks in a FTIR-PAS

spectrum are enhanced compared to an optical spectrum. Since FTIR-PAS spectra show weak peaks more clearly than optical FTIR spectra, they are ideal for studying combination and isotope peaks. That is important for our studies of $CaCO_3$, and we can even identify combination modes that involve lattice modes. The ^{13}C ν_2 mode of calcite shows strong correlation with the ν_4 mode, which is different to the ^{12}C ν_2 mode. This feature is interesting, and further studies will be needed to understand the reason.

Chapter 8

Conclusion

8.1 Summary of thesis work

Investigation of structural disorder in a solid is an important aspect for material studies due to that the formation and transformation of materials can be investigated by structural disorder in them. Our studies highlighted the abilities of vibrational spectroscopy to detect structural disorder in calcite.

Previous studies indicate that two normal vibrational modes (out-of-plane bend mode (ν_2) and in-plane bend (ν_4) mode) in calcite are differently affected by disorder [22, 24, 38]. In order to explain this phenomenon, the effects of temperature (from 77 K to 773 K) on the ν_2 and ν_4 modes were thoroughly studied by performing FTIR measurements. We found that the ν_4 mode is more sensitive to temperature. For synthesized calcite, the peak width of the ν_2 mode remains as constant (the width changes by -2$\pm$2% from 293 K to 598 K), while the ν_4 significantly broadens (the widths changes by 42$\pm$2% from 293 K to 598 K). The broadening effects due to temperature (from 293 K to 598 K) in other carbonate minerals (dolomite, aragonite, and vaterite) were analyzed. The ν_4 mode significantly broadens for minerals having

planar structures of carbonate ions (48±5% for dolomite, 40±10% and 90±40% (713 cm^{-1} and 700 cm^{-1}) for aragonite, 2±8% for vaterite), while the ν_2 mode remains during heating for all cases. Therefore, we attribute the broadening effects in the ν_4 mode of calcite to the planar structure of its carbonate ions. We also provide a general method identifying a defect sensitive vibration mode in other minerals.

Do different types of long-range disorder give the same effects to the ν_4 mode in calcite? To understand this question, three types of long-range disorder, including crystallinity (domain size), lattice strain, and microstrain fluctuation, in different calcite samples were evaluated by employing XRD measurements. Their domain sizes, lattice strains in {001} planes, and microstrain fluctuations are very different (from 90 nm to over 350 nm for domain sizes, from -0.4(7)% to 0.3(5)% for lattice strain, and from 0.006% to 0.195% for microstrain fluctuation, respectively). All three types of disorder affect the relative peak intensities in calcite FTIR spectra, making the "grinding curve" of each sample varied. This work demonstrates that identifying the specific type of disorder only by performing FTIR measurements is challenging, and it suggests that grinding curves can be an effective method for rapid screening of samples.

Effects of long-range defects on vibrations were studied in Chapter 3 and 4, and Chapter 5 focuses on short-range disorder in calcite based minerals. By combining XRD, EXAFS and FTIR methods, we differentiated among plaster samples by their short-range environments, and the carbonation processes in them were studied. Plaster samples show similar XRD patterns and FTIR spectra. The bonding distances calculated by fitting EXAFS regions are also the same for all plaster samples (around 2.38 Å for Ca-O^1 bonds, around 3.36 Å for Ca-C bonds, around 3.48 Å for Ca-O^2 bonds, and around 4.06 Å for Ca-Ca bonds). However, the *R*-factors, which indicate the fitting stability, for plaster samples prepared at 800 °C (from 10% to 16%) are

significantly larger than those prepared at 900 °C (from 35% to 48%). We suggest that it is due to the influence of $Ca(OH)_2$ in plaster samples. The degree of carbonation in a plaster sample strongly depends on the heating temperature, rather than starting materials. Peaks related to combination modes

In Chapter 6, we demonstrate FTIR can be used to detect isotopic "defects". Our studies indicated that two specific peaks are due to ^{13} C ν_2 (at 848 cm^{-1}) and ν_3 (at 1398 cm^{-1}). Furthermore, some IR peaks move with increasing ^{13}C concentration. In Chapter 7, we demonstrated that FTIR-PAS (FTIR-photoacoustic spectroscopy) is helpful for studying weak peaks related to combination modes and isotopes. We noticed the structural defects usually play a significance effects on these weak peaks, and FTIR-PAS is an ideal method to study them.

Vibrations have been studied for many decades, but they are not fully understood. My thesis research focuses on the vibrations in calcite and the effects of structural disorder on them. My thesis goal is to track structural differences and identify their origins in a solid using vibrational spectroscopy. By carrying out temperature dependent FTIR measurements on calcite, we found disorder sensitive vibrations are also temperature dependent, and therefore, it is possible to investigate structural differences using vibrational spectroscopy. However, further research suggested that using vibrational spectroscopy alone is not sufficient to track structural differences in detail. Other techniques, including XRD and XAFS, were utilized to distinguish different types of structural disorder. I am not able to identify the origins of structural defects based on work in this dissertation, but I think that using other techniques at a higher spatial resolution could be helpful for future studies.

During the research, we noticed that isotopic vibrations present some interesting features. However, their IR peaks were usually very weak, making quantitative analyses difficult. Isotopic substitution in a solid can be related to its formation and storage

conditions, which makes studies of this important to researchers. By increasing the spectral resolution, using vacuum measurement environments (to eliminate water vapor effects), and utilizing acoustic detection (to increase relative intensities of weak peaks), I was able to analyze peaks related to isotopic vibrations. The results indicate that isotopic concentrations correlate to relative peak areas, and isotope concentrations play an interesting role in determining peak positions. Furthermore, although isotopic substitution is usually not considered to affect structure, our results indicate that there is a strong correlation between structural defects and isotopic vibrations in calcite. I suggest that FTIR has the potential to study isotopes and the influences of structures on them, which has not been well utilized in the past.

8.2 Future work and broader contexts

Two aspects still need further investigation. First, does disorder affect IR peak widths? We studied the effects of disorder and temperature on IR peak intensities. However, the effects of disorder on IR peak widths have not been discussed. Although the main challenge is that IR peak widths are strongly affected by preparation and measurement methods, those effects can be eliminated by carefully controlling measurement conditions. Comparing peak widths with different types of disorder would allow us to quantitatively analyze structural disorder by peak widths. Another question is whether vibrational spectroscopy can be utilized to study disorder in other minerals besides calcite. Although some studies have demonstrated that some specific vibrations in quartz, hydroxyapatite, and silicon show structural disorder dependency [39, 67, 84, 135], detailed studies have not been reported.

Investigating structures and isotopes in a solid is one significant aspect because it can give information about the formation conditions and processes, which is important

for many fields, including mineralogy, archeology, biology, and petroleum [47,106,133]. However, traditional methods (XRD, XAFS, TEM) for detecting structures cannot detect isotopes, and vice versa. Our results demonstrate that vibrational spectroscopy can detect structural disorder and isotopes in a solid with a single measurement. The primary results from FTIR-PAS (FTIR-photoacoustic) measurements demonstrate an interesting phenomenon of the $^{13}CO_3^{2-}$ ν_2 peak of calcite: unlike the $^{12}CO_3^{2-}$ ν_2 peak, its intensity significantly varies in different calcite samples, and we suggest it is due to disorder differences. However, further investigations are still needed to support our assumption and to explain the reasons causing different behaviors of the ^{13}C and ^{12}C ν_2 peaks.

Another useful study would be to investigate other vibrational spectroscopic techniques. For example, FTIR-PAS (as mentioned above) [130] and ATR-FTIR (Attenuated total reflection-FTIR) [136, 137]. Based on our primary studies, FTIR-PAS is ideal for studying weak IR peaks, such as isotope peaks and combined peaks. For ATR-FTIR, it can examine samples with minimal preparation. Its principles can be described as follows: incident infrared light reflects off the internal surface of an ATR crystal (usually diamonds) in contact with a sample. During the reflection, an evanescent wave is formed and extends into the sample with a penetration depth depending on the wavelength of infrared light. The infrared light is collected when it exits the crystal, which gives a spectrum [138]. ATR-FTIR is widely utilized to detect surfaces and interfaces of materials [136, 139–141]. This technique can be utilized to study the adsorption properties of a solid.

Appendix A

Monitoring carbonation of lime in real time

The carbonation of lime can be described by the following chemical reaction:

$$CaO+H_2O+CO_2 \rightarrow Ca(OH)_2+CO_2 \rightarrow CaCO_3+H_2O$$

This process produces two $CaCO_3$ polymorphs: calcite and aragonite [55]. We tried to find how calcite and aragonite form during this process. The measurements were done at the Canadian Light Source Inc. (Saskatoon, SK). Due to the high intensity and brightness of synchrotron radiation, it enables us to focus on a small piece of lime and detect its FTIR spectrum in a short period. Lime samples were prepared by Dr. Michael B. Toffolo, supervised by Dr. Elisabetta Boaretto (Weizmann-Max Plank Institute of Science, Rehovot, Israel). Particles were placed on a KCl window, and both the sample and KCl window were placed in a cell. CO_2 flowed through water and then filled the cell. Lime particles were therefore emerged in the wet CO_2, which accelerated the carbonation process.

FTIR spectra were collected using a Bruker Vertex 70v vacuum spectrometer connected to a Hyperion 3000 IR microscope with a liquid-nitrogen-cooled single-

element HgCdTe (MCT) detector. The beam size was modified to a circular area with a diameter of 0.45 μm, and the beam was focused on a single lime particle. One spectrum was collected every 30 minutes over 8 hours. The ν_2 region and the OH-stretch mode of collected spectra are presented in Figure A.1 (a) and (b). Baselines were subtracted in OPUS software. A gradual increase in both calcite and aragonite ν_2 peaks was observed, indicating the carbonation of lime. We found that the calcite ν_2 peak increases sooner than the aragonite ν_2 peak. OH- stretch peaks also increase with time due to the formation of $Ca(OH)_2$. The shoulder on the higher side of the OH-stretch peak is probably due to the adsorbed water on particles, and it disappeared with time.

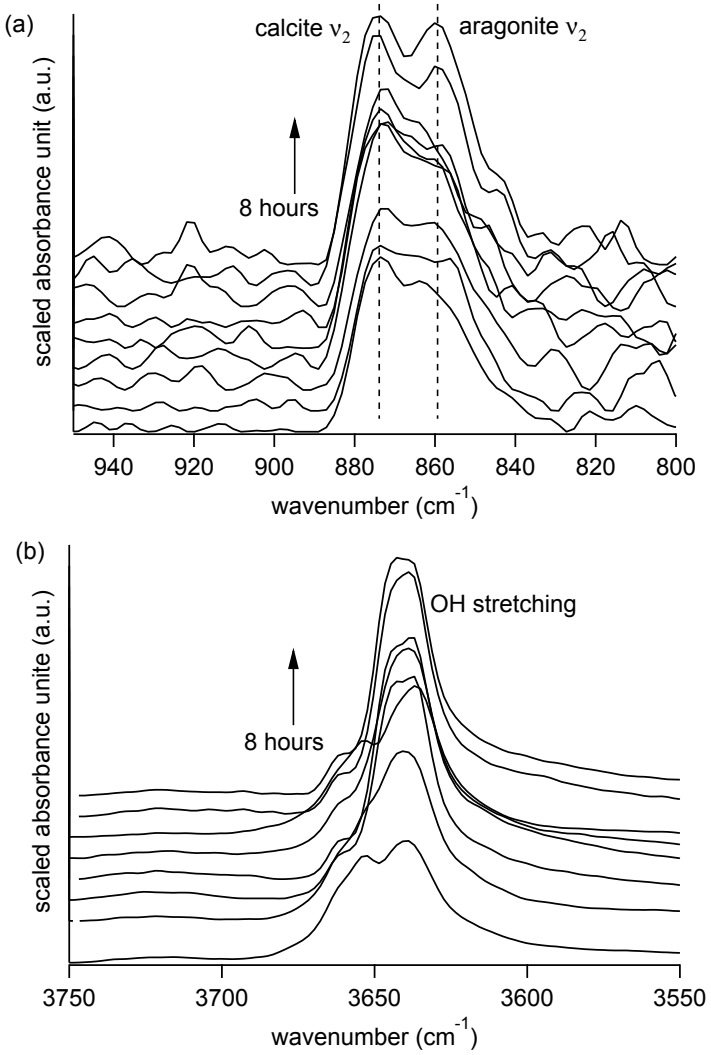

Figure A.1: FTIR spectra of a single lime particle exposed to wet CO_2 for 8 hours. The ν_2 region is presented in (a), and the OH- stretch mode is presented in (b).

Bibliography

[1] L. Valenzano, Y. Noel, R. Orlando, C. Zicovich-Wilson, M. Ferrero, and R. Dovesi. Ab initio vibrational spectra and dielectric properties of carbonates: magnesite, calcite and dolomite. *Theor. Chem. Acc.*, 117(5-6):991–1000, 2007.

[2] S. A. Markgraf and R. J. Reeder. High-temperature structure refinements of calcite and magnesite. *Am. Mineral.*, 70:590–600, 1985.

[3] K. Hellwege, W. Lesch, M. Plihal, and G. Schaack. Zwei-phononen-absorptionsspektren und dispersion der schwingungszweige in kristallen der kalkspatstruktur. *Z. Physik*, 232(1):61–86, 1970.

[4] J. P. R. de Villiers. Crystal structure of aragonite, strontianite and vaterite. *Am. Mineral.*, 56:758–767, 1971.

[5] R. Demichelis, P. Raiteri, J. D. Gale, and R. Dovesi. A new structural model for disorder in vaterite from first-principles calculations. *Cryst. Eng.*, 14:44–47, 2012.

[6] *American Mineralogist Crystal Structure Database. http://rruff.geo.arizona.edu/AMS/amcsd.php*, 2014.

[7] D. N. Sathyanarayana. *Vibrational Spectroscopy: Theory and Applications*. New Age International (P) Ltd., New Delhi (2004), 2004.

[8] J. R. Ferraro and K. Nakamoto. *Introductory Raman Spectroscopy*. Academic Press , Inc., San Diego (1994), 1994.

[9] *Joint Commission on Powder Diffraction Standards C International Centre for Diffraction Data, http://www.icdd.com*, 2003.

[10] B.-K. Teo. Extended X-Ray Absorption Fine Structure (EXAFS) Spectroscopy: Techniques and Applications. In B. Teo and D. Joy, editors, *EXAFS Spectroscopy*, pages 13–58. Springer Science & Business Media, New York (1981), 1981.

[11] C. E. Weir and E. R. Lippincott. Infrared studies of aragonite, calcite, and vaterite type structures in the borates, carbonates, and nitrates. *J. Res. Nat. Bur. Stand. A. Physc. and Chem.*, 65A:173–183, 1961.

[12] L. Gago-Duport, M. J. I. Briones, J. B. Rodriguez, and B. Covelo. Amorphous calcium carbonate biomineralization in the earthworm calciferous gland: Pathways to the formation of crystalline phases. *J. Struct. Biol.*, 162(3):422–435, 2008.

[13] B. Pokroy, A. Fitch, and E. Zolotoyabko. The microstructure of biogenic calcite: a view by high - resolution synchrotron powder diffraction. *Adv. Mater.*, 18(18):2363–2368, 2006.

[14] F. R. McFeely, S. P. Kowalczyk, L. Ley, R. G. Cavell, R. A. Pollak, and D. A. Shirley. X-ray photoemission studies of diamond, graphite, and glassy carbon valence bands. *Phys. Rev. B*, 9:5268–5278, Jun 1974.

[15] J. Robertson and E. P. O'Reilly. Electronic and atomic structure of amorphous carbon. *Phys. Rev. B*, 35:2946–2957, Feb 1987.

[16] M. A. Rodriguez, J. F. Browning, C. S. Frazer, C. S. Snow, R. G. Tissot, and E. P. Boespflug. Unit cell expansion in ErT_2 films. *Powder Diffr.*, 22:118–121, 6 2007.

[17] S. Qiu, V. B. Krishnan, S. A. Padula, R. D. Noebe, D. W. Brown, B. Clausen, and R. Vaidyanathan. Measurement of the lattice plane strain and phase fraction evolution during heating and cooling in shape memory NiTi. *Appl. Phys. Lett.*, 95(14):141906, 2009.

[18] A. K. Zak, W. A. Majid, M. Abrishami, and R. Yousefi. X-ray analysis of ZnO nanoparticles by Williamson−Hall and size−strain plot methods. *Solid State Sci.*, 13(1):251–256, 2011.

[19] M. Schieber, T. Schlesinger, R. James, H. Hermon, H. Yoon, and M. Goorsky. Study of impurity segregation, crystallinity, and detector performance of melt-grown cadmium zinc telluride crystals. *J. Cryst. Growth*, 237C239, Part 3(0):2082–2090, 2002.

[20] X. Long, M. J. Nasse, Y. Ma, and L. Qi. From synthetic to biogenic Mg-containing calcites: a comparative study using FTIR microspectroscopy. *Phys. Chem. Chem. Phys.*, 14:2255–2263, 2012.

[21] R. L. McCreery. *Raman Spectroscopy for Chemical Analysis*. John Wiley & Sons, Inc., New York (2000), 2000.

[22] K. M. Poduska, L. Regev, E. Boaretto, L. Addadi, S. Weiner, L. Kronik, and S. Curtarolo. Decoupling local disorder and optical effects in infrared spectra:

differentiating between calcites with different origins. *Adv. Mater.*, 23(4):550–554, 2011.

[23] L. Regev, K. M. Poduska, L. Addadi, S. Weiner, and E. Boaretto. Distinguishing between calcites formed by different mechanisms using infrared spectrometry: archaeological applications. *J. Archaeolog. Sci.*, 37(12):3022–3029, 2010.

[24] Y. Politi, Y. Levi-Kalisman, S. Raz, F. Wilt, L. Addadi, S. Weiner, and I. Sagi. Structural characterization of the transient amorphous calcium carbonate precursor phase in sea urchin embryos. *Adv. Funct. Mater.*, 16(10):1289–1298, 2006.

[25] D. Gebauer, P. N. Gunawidjaja, J. Y. P. Ko, Z. Bacsik, B. Aziz, L. Liu, Y. Hu, L. Bergstrom, C.-W. Tai, T.-K. Sham, M. Eden, and N. Hedin. Proto-calcite and proto-Vaterite in amorphous calcium carbonates. *Angew. Chem. Int. Ed.*, 49(47):8889–8891, 2010.

[26] S. M. Sze and K. K. Ng. *Physics of Semiconductor Devices*. John Wiley & Sons, Inc., New Jersey (2007), 2007.

[27] J. S. Yin and Z. L. Wang. Ordered Self-Assembling of Tetrahedral Oxide Nanocrystals. *Phys. Rev. Lett.*, 79:2570–2573, 1997.

[28] Z. Samoilenko, V. Okunev, E. Pushenko, T. Dyachenko, A. Cherenkov, P. Gierlowski, S. Lewandowski, A. Abaloshev, A. Klimov, and A. Szewczyk. Variety of LaSrMnO structures induced by growth conditions and laser irradiation. *Tech. Phys.*, 48(2):250–256, 2003.

[29] K. J. Murata and M. B. Norman. An index of crystallinity for quartz. *Am. J. Sci.*, 276(9):1120–1130, 1976.

[30] E. Beniash, J. Aizenberg, L. Addadi, and S. Weiner. Amorphous calcium carbonate transforms into calcite during sea urchin larval spicule growth. *Proc. R. Soc. Lond. B Biol. Sci.*, 264(1380):461–465, 1997.

[31] L. Addadi, S. Raz, and S. Weiner. Taking advantage of disorder: amorphous calcium carbonate and its roles in biomineralization. *Adv. Mater.*, 15(12):959–970, 2003.

[32] E. Loste, R. M. Wilson, R. Seshadri, and F. C. Meldrum. The role of magnesium in stabilising amorphous calcium carbonate and controlling calcite morphologies. *J. Cryst. Growth*, 254(1):206–218, 2003.

[33] C. Suryanarayana and M. G. Norton. *X-ray Diffraction: a Practical Approach*. Springer Science & Business Media, New York (1998), 1998.

[34] D. B. Williams and C. B. Carter. *The Transmission Electron Microscope*. Springer Science & Business Media, New York (1996), 1996.

[35] R. S. K. Lam, J. M. Charnock, A. Lennie, and F. C. Meldrum. Synthesis-dependant structural variations in amorphous calcium carbonate. *Cryst. Eng.*, 9:1226–1236, 2007.

[36] V. G. Keramidas and W. B. White. Raman scattering study of the crystallization and phase transformations of ZrO_2. *J. Am. Ceram. Soc.*, 57(1):22–24, 1974.

[37] S. Shoval, Y. Ginott, and Y. Nathan. A new method for measuring the crystallinity index of quartz by infrared spectroscopy. *Mineral. Mag.*, 55:579–582, 1991.

[38] R. Gueta, A. Natan, L. Addadi, S. Weiner, K. Refson, and L. Kronik. Local atomic order and infrared spectra of biogenic calcite. *Angew. Chem. Int. Ed.*, 46(1-2):291–294, 2007.

[39] E. Balan, S. Delattre, D. Roche, L. Segalen, G. Morin, M. Guillaumet, M. Blanchard, M. Lazzeri, C. Brouder, and E. K. Salje. Line-broadening effects in the powder infrared spectrum of apatite. *Phys. Chem. Miner.*, 38(2):111–122, 2011.

[40] G. Falini, S. Fermani, M. Gazzano, and A. Ripamonti. Structure and morphology of synthetic magnesium calcite. *J. Mater. Chem.*, 8:1061–1065, 1998.

[41] J. C. Decius, O. G. Malan, and H. W. Thompson. The Effect of Intermolecular Forces Upon the Vibrations of Molecules in the Crystalline State. I. The Out-of-Plane Bending of the Carbonate Ion in Aragonite Minerals. *Proc. R. Soc. London, Ser. A*, 275(1362):295–309, 1963.

[42] P. Gillet, P. McMillan, J. Schott, J. Badro, and A. Grzechnik. Thermodynamic properties and isotopic fractionation of calcite from vibrational spectroscopy of ^{18}O-substituted calcite. *Geochim. Cosmochim. Acta*, 60(18):3471–3485, 1996.

[43] M. Prencipe, F. Pascale, C. M. Zicovich-Wilson, V. R. Saunders, R. Orlando, and R. Dovesi. The vibrational spectrum of calcite $CaCO_3$: an ab initio quantum-mechanical calculation. *Phys. Chem. Miner.*, 31(8):559–564, 2004.

[44] L. Valenzano, F. J. Torres, K. Doll, F. Pascale, C. M. Zicovich-Wilson, and R. Dovesi. Ab initio study of the vibrational spectrum and related properties of crystalline compounds; the case of $CaCO_3$ calcite. *Zeitschrift für Physikalische Chemie*, 220(7/2006):893–912, 2006.

[45] G. Duyckaerts. The infra-red analysis of solid substances. A review. *Analyst*, 84:201–214, 1959.

[46] R. Ruppin and R. Englman. Optical phonons of small crystals. *Rep. Prog. Phys.*, 33(1):149, 1970.

[47] V. Mavromatis, M. Schmidt, R. Botz, L. Comas-Bru, and E. H. Oelkers. Experimental quantification of the effect of Mg on calcite-aqueous fluid oxygen isotope fractionation. *Chem. Geol.*, 310C311(0):97–105, 2012.

[48] M. R. Kagan and R. L. McCreery. Reduction of fluorescence interference in Raman spectroscopy via analyte adsorption on graphitic carbon. *Anal. Chem.*, 66(23):4159–4165, 1994.

[49] M. Donoghue, P. Hepburn, and S. Ross. Factors affecting the infrared spectra of planar anions with D_{3h}, symmetry-V: The origin of the splitting of the out-of-plane bending mode in carbonates and nitrates. *Spectrochim. Acta, Part A*, 27(7):1065–1072, 1971.

[50] W. B. White. *The carbonate minerals*, volume 4. Monograph, 1974.

[51] C. Carteret, M. De La Pierre, M. Dossot, F. Pascale, A. Erba, and R. Dovesi. The vibrational spectrum of $CaCO_3$ aragonite: A combined experimental and quantum-mechanical investigation. *J. Chem. Phys.*, 138(1):014201, 2013.

[52] G. Falini, S. Albeck, S. Weiner, and L. Addadi. Control of aragonite or calcite polymorphism by mollusk shell macromolecules. *Science*, 271(5245):67–69, 1996.

[53] J. A. Kleypas, R. W. Buddemeier, D. Archer, J.-P. Gattuso, C. Langdon, and B. N. Opdyke. Geochemical consequences of increased atmospheric carbon dioxide on coral reefs. *Science*, 284(5411):118–120, 1999.

[54] N. H. de Leeuw and S. C. Parker. Surface structure and morphology of calcium carbonate polymorphs calcite, aragonite, and vaterite: an atomistic approach. *J. Phys. Chem. B*, 102(16):2914–2922, 1998.

[55] M. B. Toffolo and E. Boaretto. Nucleation of aragonite upon carbonation of calcium oxide and calcium hydroxide at ambient temperatures and pressures: a new indicator of fire-related human activities. *J. Archaeolog. Sci.*, 49(0):237–248, 2014.

[56] B. Dickens and J. Bowen. Refinement of the crystal structure of the aragonite phase of $CaCO_3$. *J. Res. Nat. Bur. Stand.*, 75:27–32, 1971.

[57] E. M. Pouget, P. H. H. Bomans, A. Dey, P. M. Frederik, G. de With, and N. A. J. M. Sommerdijk. The development of morphology and structure in hexagonal vaterite. *J. Am. Chem. Soc.*, 132(33):11560–11565, 2010.

[58] L. Kabalah-Amitai, B. Mayzel, Y. Kauffmann, A. N. Fitch, L. Bloch, P. Gilbert, and B. Pokroy. Vaterite crystals contain two interspersed crystal structures. *Science*, 340(6131):454–457, 2013.

[59] J. C. Jamieson. Phase equilibrium in the system calcite−araonite. *J. Chem. Phys.*, 21(8):1385–1390, 1953.

[60] J. Peric, M. Vucak, R. Krstulovic, L. Brecevic, and D. Kralj. Phase transformation of calcium carbonate polymorphs. *Thermochim. Acta*, 277(0):175–186, 1996.

[61] I. Hershkovitz, O. Marder, A. Ayalon, M. Bar-Matthews, G. Yasur, E. Boaretto, V. Caracuta, B. Alex, A. Frumkin, M. Goder-Goldberger, et al. Levantine cranium from Manot Cave (Israel) foreshadows the first European modern humans. *Nature*, 520:216–219, 2015.

[62] B. Xu and K. M. Poduska. Linking crystal structure with temperature-sensitive vibrational modes in calcium carbonate minerals. *Phys. Chem. Chem. Phys.*, 16:17634–17639, 2014.

[63] T. Furukawa and W. B. White. Raman spectroscopic investigation of the structure and crystallization of binary alkali germanate glasses. *J. Mater. Sci.*, 15(7):1648–1662, 1980.

[64] L. S. Taylor and G. Zografi. The Quantitative Analysis of Crystallinity Using FT-Raman Spectroscopy. *Pharm. Res.*, 15(5):755–761, 1998.

[65] F. B. Reig, J. G. Adelantado, and M. M. Moreno. FTIR quantitative analysis of calcium carbonate (calcite) and silica (quartz) mixtures using the constant ratio method. Application to geological samples. *Talanta*, 58(4):811–821, 2002.

[66] M. Ledinsky, L. Fekete, J. Stuchlik, T. Mates, A. Fejfar, and J. Kocka. Characterization of mixed phase silicon by Raman spectroscopy. *J. Non-Cryst. Solids*, 352:1209–1212, 2006.

[67] B. J. Saikia, G. Parthasarathy, and N. Sarmah. Fourier transform infrared spectroscopic estimation of crystallinity in SiO_2 based rocks. *Bull. Mater. Sci.*, 31(5):775–779, 2008.

[68] P. B. Coleman. *Practical Sampling Techniques for Infrared Analysis*. CRC Press LLC, Boca Raton (1993), 1993.

[69] L. Lauterbach, H. Wang, M. Horch, L. B. Gee, Y. Yoda, Y. Tanaka, I. Zebger, O. Lenz, and S. P. Cramer. Nuclear resonance vibrational spectroscopy reveals the FeS cluster composition and active site vibrational properties of an O^2- tolerant NAD+-reducing [NiFe] hydrogenase. *Chem. Sci.*, 6:1055–1060, 2015.

[70] M. Najac and I. M. Raman. Integration of purkinje cell inhibition by cerebellar nucleo−olivary neurons. *J. Neurosci.*, 35(2):544–549, 2015.

[71] B. E. Warren. *X-ray Diffraction*. Addison-Wesley, 1969.

[72] W. H. Zachariasen. *Theory of X-Ray Diffraction in Crystals*. John Wiley & Sons, Inc., New York (1945), 1945.

[73] V. D. Mote, Y. Purushotham, and B. N. Dole. Williamson-Hall analysis in estimation of lattice strain in nanometer-sized ZnO particles. *J. Theor. Appl. Phys.*, 6(1):6, 2012.

[74] F. R. Elder, A. M. Gurewitsch, R. V. Langmuir, and H. C. Pollock. Radiation from Electrons in a Synchrotron. *Phys. Rev.*, 71:829–830, Jun 1947.

[75] H. Winick and S. Doniach. *Synchrotron Radiation Research*. Springer Science & Business Media, New York (2012), 2012.

[76] M. Newville. Fundamentals of X-ray absorption fine structure. *Consortium for Advanced Radiation Sources, University of Chicago (USA)[http://xafs. org]*, 2004.

[77] E. Sevillano, H. Meuth, and J. J. Rehr. Extended x-ray absorption fine structure Debye-Waller factors. I. Monatomic crystals. *Phys. Rev. B*, 20:4908–4911, Dec 1979.

[78] B. Ravel and M. Newville. ATHENA, ARTEMIS, HEPHAESTUS: data analysis for X-ray absorption spectroscopy using IFEFFIT. *J. Synchrotron Radiat.*, 12(4):537–541, 2005.

[79] M. Suzuki, T. Kogure, S. Weiner, and L. Addadi. Formation of aragonite crystals in the crossed lamellar microstructure of limpet shells. *Cryst. Growth Des.*, 11(11):4850–4859, 2011.

[80] F. A. Andersen and L. Brecevic. Infrared spectra of amorphous and crystalline calcium carbonate. *Acta Chem. Scand.*, 45:1018–1024, 1991.

[81] S. Gunasekaran, G. Anbalagan, and S. Pandi. Raman and infrared spectra of carbonates of calcite structure. *J. Raman Spectrosc.*, 37(9):892–899, 2006.

[82] E. K. Salje, E., M. A. Carpenter, T. Malcherek, and T. B. Ballaran. Autocorrelation analysis of infrared spectra from minerals. *Eur. J. Mineral.*, 12(3):503–519, 2000.

[83] A. J. Blanch, J. S. Quinton, C. E. Lenehan, and A. Pring. Autocorrelation infrared analysis of mineralogical samples: The influence of user controllable experimental parameters. *Anal. Chim. Acta*, 590(2):145–150, 2007.

[84] Y. Asscher, S. Weiner, and E. Boaretto. Variations in atomic disorder in biogenic carbonate hydroxyapatite using the infrared spectrum grinding curve method. *Adv. Funct. Mater.*, 21(17):3308–3313, 2011.

[85] R. H. Stolen, C. Lee, and R. Jain. Development of the stimulated Raman spectrum in single−mode silica fibers. *J. Opt. Soc. Am. B: Opt. Phys.*, 1(4):652–657, 1984.

[86] E. Gazit, I. R. Miller, P. C. Biggin, M. S. Sansom, and Y. Shai. Structure and orientation of the mammalian antibacterial peptide cecropin P1 within phospholipid membranes. *J. Mol. Biol.*, 258(5):860–870, 1996.

[87] N. Ishizawa, H. Setoguchi, and K. Yanagisawa. Structual evolution of calcite at high temperatures: Phase V unveiled. *Sci. Rep.*, 3:2832–2836, 2013.

[88] R. A. Cowley. Anharmonic crystals. *Rep. Prog. Phys.*, 31(1):123, 1968.

[89] M. Lazzeri, M. Calandra, and F. Mauri. Anharmonic phonon frequency shift in MgB_2. *Phys. Rev. B*, 68(22):220509, 2003.

[90] E. Balan, S. Delattre, M. Guillaumet, and E. K. Salje. Low-temperature infrared spectroscopic study of OH-stretching modes in kaolinite and dickite. *Am. Mineral.*, 95(8-9):1257–1266, 2010.

[91] J. Menéndez and M. Cardona. Temperature dependence of the first-order Raman scattering by phonons in Si, Ge, and α-Sn: Anharmonic effects. *Phys. Rev. B*, 29(4):2051, 1984.

[92] J. F. Scott. Soft-mode spectroscopy: Experimental studies of structural phase transitions. *Rev. Mod. Phys.*, 46:83–128, Jan 1974.

[93] P. Rez and A. Blackwell. Ca L23 Spectrum in Amorphous and Crystalline Phases of Calcium Carbonate. *J. Phys. Chem. B*, 115:11193–11198, 2011.

[94] A. G. Kalampounias, S. N. Yannopoulos, and G. N. Papatheodorou. Temperature- induced structural changes in glassy, supercooled, and molten silica from 77 to 2150 K. *J. Chem. Phys.*, 124:014504, 2006.

[95] S. Weiner. *Microarchaeology: Beyond the Visible Archaeological Record*. Cambridge University Press, New York (2010), 2010.

[96] E. Boaretto and K. M. Poduska. Materials science challenges in radiocarbon dating: the case of archaeological plasters. *J. Mater.*, 65(4):481–488, 2013.

[97] C. N. Trueman, K. Privat, and J. Field. Why do crystallinity values fail to predict the extent of diagenetic alteration of bone mineral? *Palaeogeogr. Palaeoclimatol. Palaeoecol.*, 266(3C4):160–167, 2008.

[98] H. A. Al-Hosney and V. H. Grassian. Water, sulfur dioxide and nitric acid adsorption on calcium carbonate: A transmission and ATR-FTIR study. *Phys. Chem. Chem. Phys.*, 7:1266–1276, 2005.

[99] D. Buti, F. Rosi, B. Brunetti, and C. Miliani. In-situ identification of copper-based green pigments on paintings and manuscripts by reflection FTIR. *Anal. Bioanal. Chem.*, 405(8):2699–2711, 2013.

[100] G. Tarquini, S. N. Cesaro, and L. Campanella. Identification of oil residues in Roman amphorae (Monte Testaccio, Rome): A comparative FTIR spectroscopic study of archeological and artificially aged samples. *Talanta*, 118(0):195–200, 2014.

[101] V. Chu, L. Regev, S. Weiner, and E. Boaretto. Differentiating between anthropogenic calcite in plaster, ash and natural calcite using infrared spectroscopy: implications in archaeology. *J. Archaeolog. Sci.*, 35(4):905–911, 2008.

[102] A. Stebner, D. Brown, and L. Brinson. Youngs modulus evolution and texture-based elastic-inelastic strain partitioning during large uniaxial deformations of monoclinic nickel-titanium. *Acta Mate.*, 61(6):1944–1956, 2013.

[103] E. Zolotoyabko and J. P. Quintana. Non-destructive microstructural analysis with depth resolution: application to seashells. *J. Appl. Crystallogr.*, 35(5):594–599, 2002.

[104] H. Leemreize, J. R. Eltzholtz, and H. Birkedal. Lattice macro and microstrain fluctuations in the calcified byssus of Anomia simplex. *Eur. J. Mineral.*, 2014.

[105] G. Williamson and W. Hall. X−ray line broadening from filed aluminium and wolfram. *Acta Metall.*, 1:22–31, 1953.

[106] K. M. Poduska, L. Regev, F. Berna, E. Mintz, I. Milevski, H. Khalaily, S. Weiner, and E. Boaretto. Plaster characterization at the PPNB site of Yiftahel (Israel) including the use of ^{14}C: implications for plaster production, preserva. *Radiocarbon*, 54:887–896, 2012.

[107] W. D. Bischoff, S. K. Sharma, and F. T. MacKenzie. Carbonate ion disorder in synthetic and biogenic magnesian calcites; a Raman spectral study. *Am. Mineral.*, 70(5-6):581–589, 1985.

[108] E. Zolotoyabko, E. N. Caspi, J. S. Fieramosca, R. B. Von Dreele, F. Marin, G. Mor, L. Addadi, S. Weiner, and Y. Politi. Differences between Bond Lengths in Biogenic and Geological Calcite. *Cryst. Growth Des.*, 10(3):1207–1214, 2010.

[109] Y. Levi-Kalisman, S. Raz, S. Weiner, L. Addadi, and I. Sagi. Structural differences between biogenic amorphous calcium carbonate phases using X-ray absorption spectroscopy. *Adv. Funct. Mater.*, 12(1):43–48, 2002.

[110] G. Falini, S. Fermani, S. Vanzo, M. Miletic, and G. Zaffino. Influence on the formation of aragonite or vaterite by otolith macromolecules. *Eur. J. Inorg. Chem.*, 2005(1):162–167, 2005.

[111] F. E. Sowrey, L. J. Skipper, D. M. Pickup, K. O. Drake, Z. Lin, M. E. Smith, and R. J. Newport. Systematic empirical analysis of calcium-oxygen coordination environment by calcium K-edge XANES. *Phys. Chem. Chem. Phys.*, 6:188–192, 2004.

[112] B. L. Phillips, Y. J. Lee, , and R. J. Reeder. Organic Coprecipitates with Calcite:65 NMR Spectroscopic Evidence. *Environ. Sci. Technol.*, 39(12):4533–4539, 2005.

[113] J. Feng, Y. J. Lee, R. J. Reeder, and B. L. Phillips. Observation of bicarbonate in calcite by NMR spectroscopy. *Am. Mineral.*, 91(5-6):957–960, 2006.

[114] S. L. Budk, G. Lapertot, C. Petrovic, C. E. Cunningha, N. Anderson, and P. C. Canfield. Boron Isotope Effect in Superconducting MgB_2. *Phys. Rev. Lett.*, 86(9):1877–1880, 2001.

[115] T. W. Boutton. Stable carbon isotope ratios of natural materials: II. Atmospheric, terrestrial, marine, and freshwater environments. *Carbon isotope techniques*, 1:173, 1991.

[116] C. Slater, T. Preston, and L. T. Weaver. Stable isotopes and the international system of units. *Rapid Commun. Mass Spectrom.*, 15(15):1270–1273, 2001.

[117] U. Gupta, V. K. Singh, V. Kumar, and Y. Khajuria. Experimental and Theoretical Spectroscopic Studies of Calcium Carbonate $CaCO_3$. *Mater. Focus*, 4(2):164–169, 2015.

[118] M. De La Pierre, C. Carteret, L. Maschio, E. Andr, R. Orlando, and R. Dovesi. The Raman spectrum of $CaCO_3$ polymorphs calcite and aragonite: A combined experimental and computational study. *J. Chem. Phys.*, 140(16):164509, 2014.

[119] M. D. L. Pierre, R. Demichelis, U. Wehrmeister, D. E. Jacob, P. Raiteri, J. D. Gale, and R. Orlando. Probing the Multiple Structures of Vaterite through Combined Computational and Experimental Raman Spectroscopy. *J. Phys. Chem. C*, 118(47):27493–27501, 2014.

[120] J. C. Decius. Coupling of the Out$-$o$f-$Plane Bending Mode in Nitrates and Carbonates of the Aragonite Structure. *The Journal of Chemical Physics*, 23(7):1290–1294, 1955.

[121] M. E. Bottcher, P.-L. Gehlken, and D. Steele. Characterization of inorganic and biogenic magnesian calcites by Fourier Transform infrared spectroscopy. *Solid State Ionics*, 101C103, part2(0):1379–1385, 1997.

[122] A. Denton and N. W. Ashcroft. Vegard's Law. *Phys. Rev. A*, 43(6):3161–3164, 1991.

[123] E. N. Maslen, V. A. Streltsov, and N. R. Streltsova. X-ray study of the electron density in calcite, $CaCO_3$. *Acta Crystallogr., Sect. B: Struct. Sci.*, 49(4):636–641, 1993.

[124] R. H. Clarke. A theory for the christiansen filter. *Appl. Opt.*, 7:861–868, 1968.

[125] A. Rosencwaig. Photoacoustic spectroscopy. New tool for investigation of solids. *Anal. Chem.*, 47(6):592A–604a, 1975.

[126] A. G. Bell. On the production and reproduction of sound by light. *Am. J. Sci.*, 20(118):305–324, 1880.

[127] A. Rosencwaig and A. Gersho. Theory of the photoacoustic effect with solids. *J. Appl. Phys.*, 47(1):64–69, 1976.

[128] F. A. McDonald and G. C. Wetsel. Generalized theory of the photoacoustic effect. *J. Appl. Phys.*, 49(4):2313–2322, 1978.

[129] H. Vargas and L. C. M. Miranda. Photoacoustic and related photothermal techniques. *Phys. Rep.*, 161(2):43–101, 1988.

[130] P. R. Griffiths and J. M. Chalmers. *Handbook of Vibrational Spectroscopy*. John Wiley & Sons, Ltd., Chichester (2002), 2002.

[131] A. P. Jathoul, J. Laufer, O. Ogunlade, B. Treeby, B. Cox, E. Zhang, P. Johnson, A. R. Pizzey, B. Philip, T. Marafioti, et al. Deep in vivo photoacoustic imaging of mammalian tissues using a tyrosinase-based genetic reporter. *Nat. Photonics*, 9:239–246, 2015.

[132] T. Ando, S. Inoue, M. Ishii, M. Kamo, Y. Sato, O. Yamada, and T. Nakano. Fourier-transform infrared photoacoustic studies of hydrogenated diamond surfaces. *J. Chem. Soc., Faraday Trans.*, 89:749–751, 1993.

[133] P. Ciais, P. P. Tans, M. Trolier, J. W. C. White, and R. J. Francey. A large northern hemisphere terrestrial CO_2 sink indicated by the $^{13}C/^{12}C$ ratio of atmospheric CO_2. *Science*, 269(5227):1098–1102, 1995.

[134] A. H. Knoll, A. J. Kaufman, and M. A. Semikhatov. The carbon-isotopic composition of Proterozoic carbonates: Riphean successions from northwestern Siberia (Anabar Massif, Turukhansk Uplift). *Am. J. Sci.*, 295(7):823–850, September 1995.

[135] M. Ledinskỳ, A. Vetushka, J. Stuchlík, T. Mates, A. Fejfar, J. Kočka, and J. Štěpánek. Crystallinity of the mixed phase silicon thin films by Raman spectroscopy. *J. Non-Cryst. Solids*, 354(19):2253–2257, 2008.

[136] I. A. Mudunkotuwa, A. A. Minshid, and V. H. Grassian. ATR-FTIR spectroscopy as a tool to probe surface adsorption on nanoparticles at the liquid-solid interface in environmentally and biologically relevant media. *Analyst*, 139:870–881, 2014.

[137] P. Kristova, L. J. Hopkinson, and K. J. Rutt. The effect of the particle size on the fundamental vibrations of the [CO_3^{2-}] anion in calcite. *J. Phys. Chem. A*, 119(20):4891–4897, 2015.

[138] F. M. Mirabella. *Internal reflection spectroscopy: Theory and applications*, volume 15. Marcel Dekker, Inc., New York (1992), 1992.

[139] M. P. Andersson, C. P. Hem, L. N. Schultz, J. W. Nielsen, C. S. Pedersen, K. K. Sand, D. V. Okhrimenko, A. Johnsson, and S. L. S. Stipp. Infrared spectroscopy and density functional theory investigation of calcite, chalk, and coccoliths−do we observe the mineral surface? *J. Phys. Chem. A*, 118(45):10720–10729, 2014.

[140] P. J. Swedlund, Y. Song, Z. D. Zujovic, M. K. Nieuwoudt, A. Hermann, and G. J. McIntosh. Short range order at the amorphous TiO_2-water interface probed by silicic acid adsorption and interfacial oligomerization: An ATR-IR and ^{29}Si MAS-NMR study. *J. Colloid Interface Sci.*, 368(1):447–455, 2012.

[141] J. D. Kubicki, K. W. Paul, L. Kabalan, Q. Zhu, M. K. Mrozik, M. Aryanpour, A.-M. Pierre-Louis, and D. R. Strongin. ATR-FTIR and density functional theory study of the structures, energetics, and vibrational spectra of phosphate adsorbed onto goethite. *Langmuir*, 28(41):14573–14587, 2012.